UNIVERSITY OF CALIFORNIA
RIVERSIDE

Topological Spintronics in Confined Geometry

A Dissertation submitted in partial satisfaction
of the requirements for the degree of

Doctor of Philosophy

in

Electrical Engineering

by

Yizhou Liu

December 2017

Dissertation Committee:

Professor Roger K. Lake, Chairperson
Professor Jianlin Liu
Professor Alexander Balandin

The Dissertation of Yizhou Liu is approved:

Committee Chairperson

University of California, Riverside

Acknowledgments

I wish to thank my adivosr Prof. Roger Lake. Doing research in Roger's lab is enjoyable, and whenever I need any help I always get useful suggestions from him. I also thank all my previous and current LATTE lab-mates. Special thanks to Prof. Jiadong Zang (UNH), Dr. Yafis Barlas, Dr. Gen Yin and Prof. Jing Shi, for their guidance and stimulating suggestions on my projects. During my intership, I also received much help from my mentors Dr. Emad Girgis and Dr. Kwaku Eason. I acknowledge all my collaborators and fruitful discussions with Dr. Junxue Li, Dr. Se Kwon Kim, Qiming Shao, Prof. Guoqiang Yu, Prof. Yongtao Cui, Prof. Igor Barsukov, Prof. Ilya Krivorotov, Dr. Eric Montoya and Dr. Zhong Shi. I would also like to thank my friends Kun Yue and Fei Deng for their inspiring daily discussions.

Chapters 2, 3, and 5 of this dissertation are, in part or in full, a reprint of the material as it appears in the following journals:

- Applied Physics Letters [1]. Reprinted with permission from [1]. ©2015. American Institute of Physics
- Physical Review B [2]. Reprinted with permission from [2]. ©2016. American Physical Society
- Journal of Magnetism and Magnetic Materials [3]. Reprinted with permission from [3]. ©2017. Elsevier

Chapters 4 and 6 are, in part or in full, a reprint from two manuscripts in preparation [4, 5].

This work was primarily supported by the Spins and Heat in Nanoscale Electronic Systems (SHINES) an Energy Frontier Research Center funded by the U.S. Department of Energy, Office of Science, Basic Energy Sciences under Award No. DE-SC0012670. Numerical simulations and collaborative travel between UCR and UNH related to work presented in Chapter 3 on skyrmion resonant modes and Chapter 4 on Hopfions were also supported by the NSF ECCS-1408168.

To my family.

ABSTRACT OF THE DISSERTATION

Topological Spintronics in Confined Geometry

by

Yizhou Liu

Doctor of Philosophy, Graduate Program in Electrical Engineering
University of California, Riverside, December 2017
Professor Roger K. Lake, Chairperson

One main objective of spintronics is to process and store information with the magnetic order parameters. Much recent attention has been given to magnetic skyrmions that reside in magnetic materials with the antisymmetric Dzyaloshinskii-Moriya interaction. Here, we study skyrmion dynamics in two different confined geometries. We first demonstrate single skyrmion creation and annihilation by spin waves in a cross-bar geometry. A critical spin-wave frequency is required both for the creation and the annihilation of a skyrmion. The minimum frequencies for creation and annihilation are similar, but the optimum frequency for creation is below the critical frequency for skyrmion annihilation. Then we investigate the resonant modes of a single Néel type skyrmion in confined nanodisks with varying aspect ratios (AR). With the increase of disk AR, multiple new modes emerge in the power spectrum, which originate from the broken rotational symmetry of both the nanodisk and the skyrmion.

Other than skyrmions, we also present the realization of a zero–field, stable hopfion spin texture in a magnetic system consisting of a chiral magnet nanodisk sandwiched by two films with perpendicular magnetic anisotropy. The preimages of the spin texture and numerical calculations of Q_H show that the hopfion has $Q_H = 1$. Further-

more, another non-trivial state that includes a monopole–antimonopole pair (MAP) is also stabilized in this system. The ground state is determined by the ratio of the helical period L of the chiral magnet to the radius and thickness of the nanodisk. The topological transition between the hopfion and the MAP state involves a creation (annihilation) of the MAP and twist of the preimages.

Another goal of spintronics is to transport spin with minimal losses. Spin superfluid transport can be achieved in easy-plane ferromagnets and antiferromagnets by creating a non-equilibrium meta-stable state with static spin spiral textures. We show that the spin superfluid analogy can be extended to include Josephson-like oscillations of the spin current in both easy-plane ferromagnets and antiferromagnets. This spin current also has a non-linear, time-averaged component which provides a 'smoking gun' signature of spin superfluidity. A spin oscillator device based on the spin superfluid Josephson effect is proposed. The 2π precession of the in–plane magnetization results in an approximately order of magnitude larger output power of the spin superfluid Josephson oscillator compared to that of a spin Hall oscillator.

Contents

List of Figures

Chapter 1

Introduction

1.1 Motivation and Outline

During the past decade, advances in new technologies, such as smart phones , have completely reshaped people's daily lives. These advances result from the exponential increase in computing power. High performance and small scale electronic devices lay the foundation of modern information technology and make it possible to build devices that people could not imagine even one decade ago. In 1965, Gordon Moore observed that the number of transistors per chip doubled every two years [8], which results in higher performance and smaller scale of the transistor. However, beginning from this year, the industry business model based on Moores law has ended. The major obstacle is that we are approaching the physical size limit of the transistor. Beyond this size limit, quantum mechanics takes over, and the performance of the transistor significantly degrades. More densely packed, faster, smaller transistors consume more power per unit area. Power and the associated heat generation have limited clock speeds to around 3-4 GHz since the mid 2000s. Increasing energy efficiency is critical for both improving high performance computing and mobile devices that rely on battery power.

The field of spintronics addresses this grand challenge by manipulating electron spins and magnetic spin textures instead of electron charge. The emerging field of spintronics proposes to use the spin, instead of the charge, of electrons as the physical representation of the logical bits. This scheme of computing by flipping electron spins, rather than by moving electrons, has the potential advantages of nonvolatility, faster data processing speed, low power consumption, and it can be integrated together with conventional semiconductor devices. Nonvolatility allows a spintronic based architecture to handle computing and data storage simultaneously in a single unit, which makes it suitable for implementing new architectures other than the conventional von Neumann architecture [3]. To enable these applications, controllable manipulation of spins becomes the key issue.

This dissertation presents a comprehensive study of topology related effects in the field of spintronics. The contents of this dissertation are basically divided into two parts. Chapter two to four explore the fundamental physics and possible applications of the magnetic topoogical solitons in confined geometry. Chapter five and six cover a novel effect called the spin Josephson effect in spin superfluids. Then the smoking gun signatures of spin superfluids and spin Josephson oscillators are introduced based on the spin Josephson effect. In the following, a brief overview of the baisc concepts in spintronics and micromagnetism is given in this chapter.

1.2 Bohr Magneton and Gyromagnetic Ratio

Assume an electron circulating around a nucleus as a classical particle as shown in Fig. 1.1. Due to the charge of the electron, this circulating motion generates a circulating electric current that is opposite to the direction of the electron. According to

Maxwell's equation, this electric current further generates a magnetic field perpendicular to the circulating plane. In the classical limit, a magnetic moment can be expressed as $\mu = IA$, where I is the electric current and A is the area. The effective current induced by this electron can be written as $I = -\frac{e}{T}$ and $T = \frac{2\pi r}{v}$ is the period of orbit. Since the electron is rotating around the nucleus, we can also write down its angular momentum as $L = mvr$ with its mass m and velocity v. Using these relationships, the magnetic moment becomes

$$\mu = \frac{evr}{2} = \frac{e\frac{L}{mr}r}{2} = \frac{e}{2m}L. \tag{1.1}$$

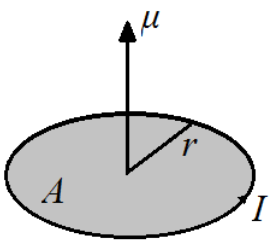

Figure 1.1: Illustration of a magnetic moment and its current loop.

Recall that the angular momentum has the form $L = \hbar\sqrt{l(l+1)}$ in quantum mechanics, so we can further write μ as

$$\mu = \frac{e\hbar}{2m}s = \mu_{\mathrm{B}}s, \tag{1.2}$$

where we define $\mu_{\mathrm{B}} = \frac{e\hbar}{2m} = 9.2740 \times 10^{-24}$ J/T as the Bohr magneton. Bohr magneton is the basic unit for expressing the magnetic moment. s in Eq. 1.2 is a quantity that counts the magnetic moment numbers for diferent systems, which will depend on specific material parameters.

Other than the Bohr magneton, we can rewrite Eq. 1.1 as $\mu = \gamma L$ where $\gamma = \frac{e}{2m}$ is the gyromagnetic ratio, which is the ratio of a system's magnetic moment to

its angular momentum. The gyromagnetic ratio defines a fundamental frequency when the system is placed in an external field, thus it is very important for the dynamics of a magnetic system. The above definition is only valid in the classical limit, since we take the electron as a classical particle and ignore its quantum properties. When the quantum nature of the electron is taken into account, the correct expression of the gyromagnetic ratio becomes

$$\gamma = g\frac{\mu_{\mathrm{B}}}{\hbar}, \tag{1.3}$$

where g is the Landé g-factor. This definition takes into account the spin nature of electron. For a single free electron $\gamma = 1.76 \times 10^{11}$rad Hz T^{-1}, which is the value often used in micromagnetic simulations as a constant. However, since the g-factor varies for different materials, sometimes it is important to use the modified gyromagnetic ratio value in order to get the correct results.

1.3 Magnetic Interaction

In this section, a brief overview of different magnetic interactions is presented. There are various types of magnetic interactions in magnetic system from short range to long range. These magnetic interactions play important roles in determining the magnetization dynamics.

1.3.1 Exchange Interaction

One of the most fundamental interactions in magnetic systems is the exchange interaction. The exchange interaction is a short range interaction that is only present between close neighbors. The simplest expression of the exchange interaction is

$$\mathcal{H}_{exch} = \sum_{<i,j>} -J\mathbf{S}_i \cdot \mathbf{S}_j. \tag{1.4}$$

Here J is the exchange parameter and $\mathbf{S} = S\mathbf{m}$ denotes the spin at each magnetic site. In the simplest case, the interaction is only between *nearest neighbors*. J is normally isotropic in space, but for some special cases it may becomes anisotropic. The sign of J determines the lowest energy state of the spin. For $J > 0$, parallel spins minimize the energy, which results in a ferromagnetic (FM) state (Fig. 1.2 (a)). For $J < 0$, anti-parallel spins minimize the energy, which results in an antiferromagnetic (AFM) state (Fig. 1.2 (b)).

If we assume $J > 0$ and it is strong enough to keep the neighbor spins almost parallel, we can extend Eq. 1.4 in the following manner. Assume $\theta_{i,j}$ is the angle between the neighbor spins direction $\mathbf{m}_i$ and $\mathbf{m}_J$. Since the neighbor spins change slowly over space, $\theta_{i,j}$ is a very small angle and we can write Eq. 1.4 as

$$\begin{aligned}\mathcal{H}_{exch} &= -JS^2 \sum_{<i,j>} cos(\theta_{i,j}) \simeq -JS^2 \sum_{<i,j>} (1 - \frac{{\theta_{i,j}}^2}{2}) \\ &= \text{const} + \frac{JS^2}{2} \sum_{<i,j>} {\theta_{i,j}}^2 \simeq \text{const} + \frac{JS^2}{2} \sum_{<i,j>} (\mathbf{m}_j - \mathbf{m}_i)^2. \end{aligned} \tag{1.5}$$

By further writing $\mathbf{m}$ as a continuous function, we will have $\mathbf{m}_j - \mathbf{m}_i = (\mathbf{r}_{i,j} \cdot \nabla)\mathbf{m}$, where $\mathbf{r}_{i,j}$ is the vector pointing from position $\mathbf{r}_i$ to position $\mathbf{r}_j$. After using this relationship, Eq. 1.5 becomes

$$\mathcal{H}_{exch} = const + \frac{JS^2}{2} \sum_{<i,j>} [(\mathbf{r}_{i,j} \cdot \nabla)\mathbf{m})]^2 \tag{1.6}$$

Summing over all the nearest neighbors of each site and change the first summation

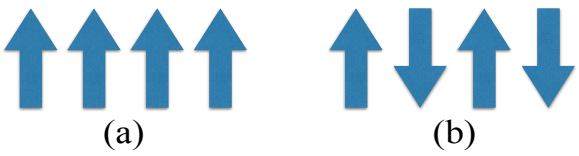

Figure 1.2: (a) FM state (b) AFM state

to an integral, we arrive at the famous continuous form of exchange interaction (the constant term is ignored)

$$\mathcal{H}_{exch} = \int A(\nabla \mathbf{m})^2 d\mathbf{r} \tag{1.7}$$

and $A = \frac{JS^2}{2a}$ is the so-called exchange constant with the lattice constant a. The derivations above connect the atomic exchange parameter J to the continuum exchange constant A. Although sometimes the exchange interaction is more complicated and needs to be analyzed through many-body physics or calculated from first principles, this simple model still provides a powerful model to semiclassically study the magnetization dyanmics.

In the model above, we only take into account the nearest neighbor sites because the exchange paramter is much smaller beyond nearest neighbor. However, in some special cases, for example in the frustrated magnets, the exchange interaction is still strong beyond nearest neighbor and cannot be ignored. In this case, the competing exchange interactions on a cubic lattice can be described by

$$\mathcal{H}_{exch} = -J_1 \sum_{<i,j>} \mathbf{S}_i \cdot \mathbf{S}_j + J_2 \sum_{<<i,j>>} \mathbf{S}_i \cdot \mathbf{S}_j + J_3 \sum_{<<<i,j>>>} \mathbf{S}_i \cdot \mathbf{S}_j \tag{1.8}$$

Here the summation includes up to the third-neighbor interaction as shown in Fig. 1.3. The system can be also extended to a triangular lattice or a kagome lattice, which is

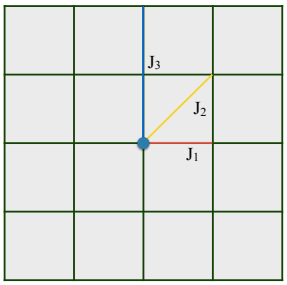

Figure 1.3: J_1 - J_2 - J_3 model on a cubic lattice

a model for many frustrated magnets. Since the exchange interaction J_i can be either FM type or AFM type, these competing interactions may induce different spin textures such as FM ordering in–plane and AFM ordering cross–plane.

1.3.2 Dzyaloshinskii-Moriya interaction

The Dzyaloshinskii-Moriya interaction (DMI) is also a short range interaction, which is due to the broken of inversion symmetry [9, 10]. A general expression of DMI is

$$\mathcal{H}_{DM} = \mathbf{D}_{ij} \cdot (\mathbf{S}_i \times \mathbf{S}_j), \tag{1.9}$$

where $\mathbf{D}_{ij}$ is the DM constant vector. The direction of $\mathbf{D}_{ij}$ is determined by the symmetry of unit cell [9]. Unlike the exchange interaction, which tends to make neighbor spins parallel or anti-parallel, the DMI tends to make neighboring spins perpendicular with each other. Thus the competing interaction between the exchange interaction and the DMI modulates the spin to form a helical chain.

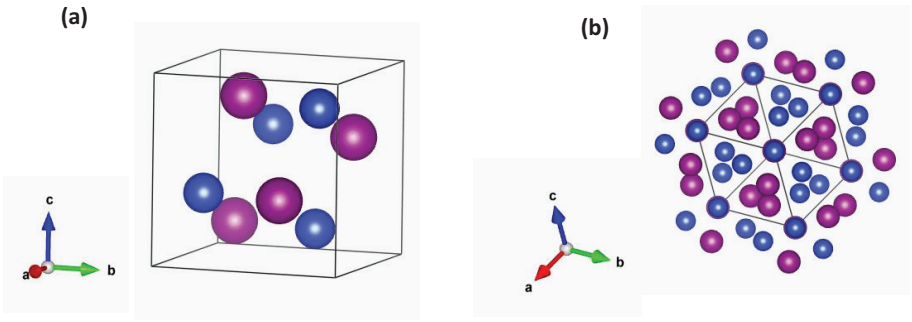

Figure 1.4: (a) The unit cell of MnSi. (b) The (111) face of MnSi lattice. Pink balls stand for Mn atoms, and the blue balls stand for the Si atoms.

In bulk materials, such as MnSi (Fig. 1.4), the inversion symmetry is broken in its unit cell, which results in a bulk DM vector $\mathbf{D}_{ij} = \mathbf{r}_{ij}$. There is a series of materials similar to MnSi, known as the B20 compounds, which host a similar DM

vector. The DMI can also be artificially induced by putting a material with strong spin-orbit coupling (SOC), such as a heavy metal, on top of an ultra-thin magnetic film. The broken inversion symmetry at the interface and the large SOC can induce an interfacial type DMI, as shown in Fig. 1.5. The interfacial DMI has a DM vector $\mathbf{D}_{ij} \perp \mathbf{r}_{ij}$, which is also perpendicular to the interface plane. In continuum limit, the bulk DMI is written as

$$\mathcal{H}_{DM} = \int D_{\text{cont}} \mathbf{s} \cdot (\nabla \times \mathbf{s}) d\mathbf{r}, \tag{1.10}$$

and the interfacial DMI can be written as

$$\mathcal{H}_{DM} = -\int D_{\text{cont}} \mathbf{s} \cdot [(\mathbf{z} \times \nabla) \times \mathbf{s}] d\mathbf{r}, \tag{1.11}$$

where $D_{\text{cont}} = DS^2/a^2$ is the DM constant in the continuum limit. The ratio between the exchange constant and the DM constant J/D_{cont} could be used to estimate the helical period in materials with DMI. Since the DM vector is different in bulk and interfacial system, they modify the spin directions in different ways. For bulk DMI, the DMI tends to make the spins form a Bloch type helix. In the presence of other competing interactions, the bulk DMI also favors the formation of a Bloch type skyrmion, as shown in Fig. 1.6(a). For interfacial DMI, the DMI tends to make the spins form a Néel type

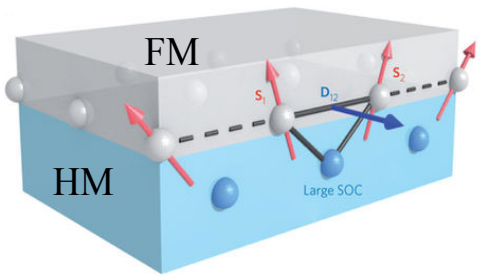

Figure 1.5: Schematic of interfacial DMI [6].

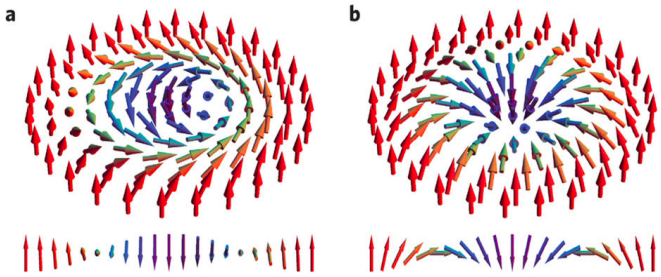

Figure 1.6: (a) Bloch type skyrmion (top) and spin helix (bottom). (b) Néel type skyrmion (top) and spin helix (bottom) [7].

helix as well as Néel type skyrmion, as shown in Fig. 1.6(b).

The DMI is an asymmetric interaction. It introduces a chirality in magnetic systems, which affects the dynamics of the system. For example, in the presence of DMI, the magnon flow is asymmetric in space. The DMI also plays an important role in the static and dynamic properties of domain walls, which are also closely related to the system's chirality. In general, the DMI is isotropic in space. Similar to the exchange interaction, the anisotropic DMI also exists in both AFM and FM materials. In an AFM system, it can lead to the formation of AFM skyrmions.

1.3.3 Magnetic Anisotropy

The exchange interaction and the DMI are the interactions with neighboring magnetic moments. Other than these interactions between neighbors, the energy of a magnetic system also depends on the direction of its magnetization. It has been experimentally observed that for most of the magnets, the magnetization always has some preferred direction, which is refered to as magnetic anisotropy. Magnetic anisotropy depends on the lattice structure and symmetry, and it is closely related to the spin orbit interaction in materials. In the absence of magnetic anisotropy, for a single spin, its energy is isotropic as shown in Fig. 1.7 (a). Magnetic anisotropy creates some local

minima directions and the number of minima depends on the exact form of magnetic anisotropy. The simplest magnetic anisotropy is the uniaxial anistropy, which has the form

$$\mathcal{H}_{an,u} = -K_u \sum_i (\mathbf{s}_i \cdot \mathbf{u})^2 \tag{1.12}$$

K_u is the anisotropy constant and $\mathbf{u}$ is a unit direction vector. When $K_u > 0$, the uniaxial anisotropy creates two local minima directions *i.e.* parallel or anti-parallel with $\mathbf{u}$, as shown in Fig. 1.7 (b). In this case, the magnetization tends to align with the axis $\mathbf{u}$ to reduce its energy, thus it is called the easy-axis case. When $K_u < 0$, the uniaxial anisotropy creates two local maxima directions *i.e.* parallel or anti-parallel with $\mathbf{u}$, as shown in Fig. 1.7 (c). In this case, the energy could be minimized when the magnetization is in the plane perpendicular with $\mathbf{u}$, and this type of anisotropy is called easy-plane anisotropy or hard-axis anisotropy.

In Eq. 1.12, only the first order effect is considered. There also exists higher order terms such as the 4th and 6th order uniaxial anisotropy, and they play an important role in explaining some special phenomana such as the easy cone anisotropy. Notice that, by the definition of uniaxial anistropy, only the even order term is allowed in the expression.

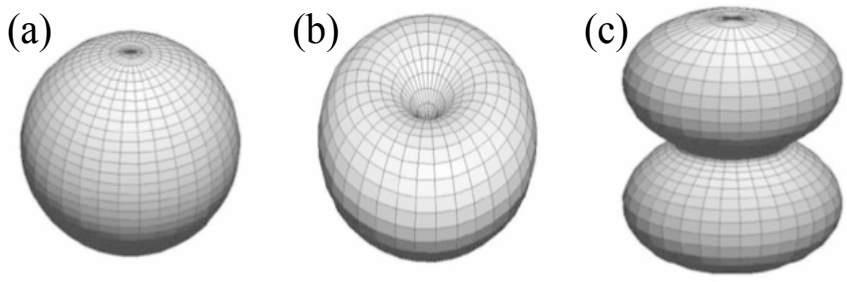

Figure 1.7: Energy landscape for (a) isotropic, (b) easy-axis and (c) easy-plane (hard-axis).

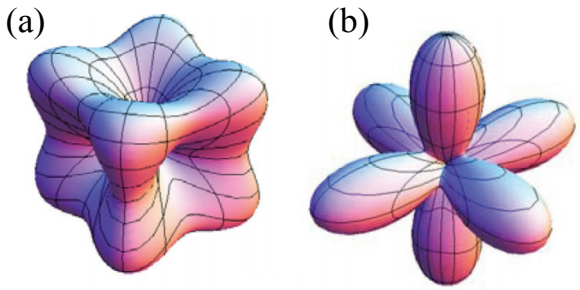

Figure 1.8: Energy landscape for cubic anisotropy with (a) $K_c > 0$ (b) $K_c < 0$.

Uniaxial anisotropy is one example of the magnetic anisotropy. The magnetic anisotropy may also has multiple preferential axes, for example in materials with speicific lattice structures. The most general one is the cubic anisotropy in materials with cubic unit cells such as iron and nickel. The cubic anisotropy can be written as

$$\mathcal{H}_{an,c} = -K_c \sum_i [(s_x)^2(s_y)^2 + (s_y)^2(s_z)^2 + (s_z)^2(s_x)^2] \tag{1.13}$$

where K_c is the anisotropy constant for cubic anisotropy. Similar with uniaxial anisotropy, only even order terms are allowed due to the definition and symmetry of magnetic anisotropy. The energy landscape for $K_c > 0$ is plotted in Fig. 1.8 (a). The local minima directions are along the three major axis of the cube. Since iron has a positive K_c, this type of cubic anisotropy is sometimes referred to as the iron-type anisotropy. The energy landscape for $K_c < 0$ is plotted in Fig. 1.8 (b). The local maxima directions are along the three major axis of the cube. This type of cubic anisotropy is similar to that of nickel, which has a negative K_c, so it is sometimes denoted as the nickel-type anisotropy. Higher order terms also exist in cubic anisotropy, which makes the energy landscape more complicated. But the amplitude of these higher order terms are, in most cases, much smaller than the first order term.

1.3.4 Magnetic Dipole-Dipole Interaction

The magnetic moment at a given position can directly interact with another magnetic moment via the magnetic dipole-dipole interaction (DDI). The DDI is a long range interaction that includes every point within the system. The DDI energy is defined as

$$\mathcal{H}_{DDI} = -\frac{\mu_0 S^2}{4\pi} \sum \frac{3(\mathbf{S}_i \cdot \mathbf{r}_{ij})(\mathbf{S}_j \cdot \mathbf{r}_{ij}) - \mathbf{S}_i \cdot \mathbf{S}_j}{|r|^3}, \tag{1.14}$$

where $\mathbf{r}_{ij}$ is the unit vector pointing from site i to site j and $|r|$ is the distance between these two sites. The DDI is an essential component in magnetic domain theory. For a magnet with a very large size, forming a single domain in which every magnetic moment points in the same direction costs a lot of energy, which is mainly due to the DDI. Thus, many domains are created in order to reduce the total energy of the system. Furthermore, the DDI is also closely related to the geometrical parameters of the sample. For example, in a magnetic thin film, due to the large ratio between the lateral size and the thickness, all the magnetic moments prefer to stay in the plane instead of out-of-plane, which is due to the presence of DDI. Thus, the DDI is also refered to as the shape anisotropy.

The DDI is not only important at long range, it also plays an important role in sub-micron size magnets. Depending on the geometry, the DDI can modify the dynamics of magnons and skyrmions. Calculating the DDI requires taking into account almost all of the magnetic moments in the system, so it is the most time consuming part in micromagnetic simulations.

1.3.5 External Magnetic Field and Zeeman Energy

When placing a magnet in an external field, the magnetic moments tend to align with the external field and the related energy is known as the Zeeman energy. The Zeeman energy has the form

$$\mathcal{H}_{\text{Zeeman}} = -\sum_i \mathbf{H}_{ext} \cdot \mathbf{S}_i. \tag{1.15}$$

Obviously it has the minimum energy when the magnetic moment is aligned with the external field.

1.4 Equation of Motion

1.4.1 Landau-Lifshitz-Gilbert Equation

The dynamics of the magnetic moment is described semiclassically by the Landau-Lifshitz (LL) equation and Landau-Lifshitz-Gilbert (LLG) equation. The LL equation was proposed by Landau and Lifshitz in 1935 which includes a derived precession term and an additional phenomenological damping term []. Then Gilbert modified their results and proposed the LLG equation in 1955 []. The LLG equation is

$$\dot{\mathbf{M}} = -\gamma \mathbf{M} \times \mathbf{H}_{eff} + \frac{\alpha}{M_s} \mathbf{M} \times \dot{\mathbf{M}} \tag{1.16}$$

where $\mathbf{M}$ is the magnetization, γ is the gyromagnetic ratio, and α is the phenomenological damping term. $\dot{\mathbf{M}}$ denotes the time deravative of magnetization, and $\mathbf{H}_{eff} = -\mathrm{d}\mathcal{H}/\mathrm{d}\mathbf{M}$ is the effeective field.

The LLG equation can be easily transformed to the LL equation. First, take the cross product $\mathbf{M}$ with both sides of Eq. 1.16,

$$\mathbf{M} \times \dot{\mathbf{M}} = -\gamma \mathbf{M} \times (\mathbf{M} \times \mathbf{H}_{eff}) + \frac{\alpha}{M_s} \mathbf{M} \times (\mathbf{M} \times \dot{\mathbf{M}}). \tag{1.17}$$

Then by using the Lagrange's formula $\mathbf{a} \times (\mathbf{b} \times \mathbf{c}) = \mathbf{b}(\mathbf{a} \cdot \mathbf{c}) - \mathbf{c}(\mathbf{a} \cdot \mathbf{b})$, the term $\frac{\alpha}{M_s}\mathbf{M} \times (\mathbf{M} \times \dot{\mathbf{M}})$ becomes

$$\frac{\alpha}{M_s}\mathbf{M} \times (\mathbf{M} \times \dot{\mathbf{M}}) = \frac{\alpha}{M_s}[\mathbf{M}(\mathbf{M} \cdot \dot{\mathbf{M}}) - \dot{\mathbf{M}}(\mathbf{M} \cdot \mathbf{M})] \tag{1.18}$$

To simplify Eq. 1.18, several relationships are employed. First, we can define $\mathbf{M} = M_s\mathbf{m}$ with the saturation magnetization M_s and the magnetization unit vector $\mathbf{m}$. Then, the second term in Eq. 1.18 can be reduced to ${M_s}^2\dot{\mathbf{M}}$. We also use the trick $\mathbf{M} \cdot \dot{\mathbf{M}} = 0$, which means the direction of change in magnetization is alwasy perpendicular to its original direction. After using these relationships, Eq. 1.17 finally becomes just

$$\mathbf{M} \times \dot{\mathbf{M}} = -\gamma\mathbf{M} \times (\mathbf{M} \times \mathbf{H}_{eff}) - \alpha M_s\dot{\mathbf{M}} \tag{1.19}$$

Inserting Eq. 1.19 back into Eq. 1.16, we have

$$\dot{\mathbf{M}} = -\frac{\gamma}{1+\alpha^2}\mathbf{M} \times \mathbf{H}_{eff} - \frac{\gamma\alpha}{(1+\alpha^2)M_s}\mathbf{M} \times (\mathbf{M} \times \mathbf{H}_{eff}) \tag{1.20}$$

which is the LL equation with damping term. Eq. 1.20 can be further normalized to

$$\dot{\mathbf{m}} = -\frac{\gamma}{1+\alpha^2}\mathbf{m} \times \mathbf{h}_{eff} - \frac{\gamma\alpha}{(1+\alpha^2)}\mathbf{m} \times (\mathbf{m} \times \mathbf{h}_{eff}) \tag{1.21}$$

with the unit vector $\mathbf{m}$ and the normalized effective field $\mathbf{h}_{eff}$. The form of Eq. 1.21 is always employed in micromagnetic simulations.

1.4.2 Finite temperature

The LLG equation only captures the magnetization dynamics at very low temperature, where the thermal effect can be neglected. In order to study magnetization at finite temperature, a thermal induced random field must be added to the LLG equation in order to mimic the effect of finite temperature. The LLG equation with thermal field can be written as

$$\dot{\mathbf{M}} = -\gamma\mathbf{M} \times (\mathbf{H}_{eff} + \mathbf{L}) + \frac{\alpha}{M_s}\mathbf{M} \times \dot{\mathbf{M}} \tag{1.22}$$

where $\mathbf{L}$ is the thermal field or Langevin field. The dissipation-fluctuation relation $\langle L_\mu(r,t)L_v(r^{'},t^{'})\rangle = \xi\delta_{\mu v}\delta_{rr'}\delta_{tt'}$ is satisfied where $\xi = \alpha k_B T/\gamma$. The average $\langle\cdots\rangle$ is taken over all realizations of the fluctuation field. In numerical calculations, the random number period for $\mathbf{L}$ must be large enough to avoid possible numerical artifacts.

Although adding the random field can describe magnetization dyanmics at finite temperature, studying the dynamics at elevated temperatures is still not possible with Eq. (1.22). This is because the magnetization is a thermally averaged quantity, and its magnitude can change a lot under elevated temperature. If one wants to deal with elevated temperature, the Landau-Lifshitz-Bloch (LLB) equation must be employed. The LLB equation is very useful for problems such as heat assisted magnetic recording.

1.5 Spin Transfer Torque

1.5.1 Slonczewski Torque

The interplay between electrical current and magnetization, which lies in the core of spintronics, has been extensively studied over the past few decades. When a spin polarized current passes through a ferromagnetic conductor, it can exert torque on the magnetic moments [11, 12] by transferring spin angular momentum. This spin transfer torque (STT) can be used to electrically manipulate the magnetization. In the equation of motion, STT is an additional term on the right side of the LLG equation, which phenomenologically describes the effect of spin polarized current.

$$\mathbf{T}_{\mathrm{STT}} = -a_J\mathbf{m}\times(\mathbf{m}\times\mathbf{p}\ ) - b_J(\mathbf{m}\times\mathbf{p}) \tag{1.23}$$

The unit vector $\mathbf{p}$ represents the direction of spin polarization. The prefactor $a_J = \frac{\hbar\gamma JP}{2|e|dM_s}$ and the prefactor $b_J = \epsilon a_J$, where P is the spin polarization factor, J is the current density and d is the thicnkess of the magnet. The factor ϵ in b_J describes the

ratio between this two torques. In the jargon of spintronics, the first term of STT is refered to as the anti-damping like torque or Slonczewski torque, since it has the same form as the damping term in the LL equation. The second term is often refered as field-like torque since it has the same form as the field precession term. The Slonczewski torque normally describes the case when the current direction is perpendicular to the magnet plane.

The Slonczewski torque can be briefly derived phenomenologically in the following way. Imagine there is a normal metal (NM) adjacent to a FM with magnetization $\mathbf{m}$ (we assume a uniform $\mathbf{m}$ in the FM) as shown in Fig. 1.9. A spin poalrized current is injected from the NM to the FM with a spin polarization $\mathbf{p}$. If $\mathbf{p}$ is non-collinear with $\mathbf{m}$, due to the s-d exchange coupling between the injected electrons and the local magnetization, the spin polarized current will try align with the local magnetization and transfer its angular momentum. After a time scale related to the s-d exchange coupling, the spin polarization of injected electron becomes parallel with the local magnetization and completes the angular momentum transfer. Since each electron carries an angular momentum $\hbar/2$ (or $-\hbar/2$), after the angular momentum transfer, the loss of angular mo-

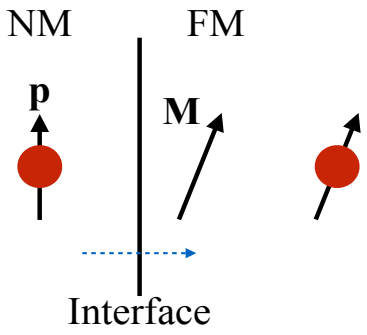

Figure 1.9: Schematic of the STT

mentum for each electron, in this process, can be expressed as $\mathbf{T}_{loss} = \frac{\hbar}{2}[\mathbf{p} - (\mathbf{p} \cdot \mathbf{m})\mathbf{m}]$. And the FM acquires the same amout of angular momentum. Assume a spin polarized current density j peperdicular to the FM and the spin transfer torque applied to all its magnetic moments, we can get the rate of change in magnetic moment is equal to (use the triple product property on Eq. 1.24)

$$\dot{\mathbf{m}} = \frac{\hbar\gamma j}{2edM_s}\mathbf{m} \times (\mathbf{m} \times \mathbf{p}) \tag{1.24}$$

where d is the thickness of the FM. The above equation basically resembles the anti-damping like torque. And the field-like torque can be understood as the spin-polarized electrons accumulation at the NM|FM interface. For a miscroscopic derivation of STT, see reference [11].

1.5.2 Zhang-Li Torque

All the moments in magnets are not always pointing in the same direction. The moments sometimes form non-uniform spin textures such as the domain walls, vortices and skyrmions. In metallic magnets, the non-uniform spin texture gives arise to another type of spin transfer torque

$$\mathbf{T}_{ZL} = u_0(\mathbf{j} \cdot \nabla)\mathbf{m} - \beta u_0[\mathbf{m} \times (\mathbf{j} \cdot \nabla)\mathbf{m}] \tag{1.25}$$

where $u_0 = \frac{Pg\mu_B}{2|e|M_s}$ with the spin polarization factor P and the current density $\mathbf{j}$. The first term represents the torque at the adiabatic limit, and the second term represents the non-adiabatic effect with the non-adiabatic factor β. This torque describes the case when the current is applied in-plane.

Chapter 2

Skyrmion Creation and Annihilation by spin waves

A magnetic skyrmion is a topologically protected spin texture with its spins pointing in all directions. The spins of a skyrmion wrap the unit sphere giving a skyrmion number (or winding number) of ± 1. [13] A collective skyrmion phase was first observed as an intermediate phase between the helical state and the ferromagnetic state in the helimagnet B20 compound MnSi. [14, 15] The lack of inversion symmetry in the B20 compounds induces an asymmetric exchange coupling known as the Dzyaloshinskii-Moriya(DM) interaction. [9, 10] The skyrmion phase emerges from the competition between the DM interaction and the symmetric Heisenberg exchange coupling. Other than the B20 compounds, magnetic skyrmions have also been observed at the Fe/Ir interface where the broken inversion symmetry at the interface introduces an interfacial DM interaction [16]. The size of a skyrmion ranges from 5nm to 100nm depending on the strength of DM interaction and exchange interaction. Previous theoretical and experimental results have demonstrated that skyrmions can be manipulated by electric

currents, electric fields, or temperature gradients. [17–20] A skyrmion is moved by a current density that is 4 to 5 orders of magnitude smaller than that required to move a domain wall. [21, 22] Spin waves or magnons also interact with skyrmions and induce magnon-skyrmion scattering. [23] A skyrmion induced topological magnon hall effect has been observed. [24] The skyrmion magnon interaction suggests the possibility of manipulating skyrmions with spin waves.

Skyrmion-based devices require single skyrmion creation and annihilation. A single skyrmion can be created by applying a spin polarized, [25,26] unpolarized, [27,28] or circulating current [29] to a ferromanetic state. Laser heating can overcome the potential barrier between the skyrmion and the ferromagnetic state. [30] Injecting a spin-polarized current into a notched geometry creates a skyrmion. [31] Most recently, skyrmion bubbles were generated by driving domain walls through a constriction. [32, 33] In this chapter, we consider a crossbar structure and investigate the creation and annihilation of skyrmions within the crossbar using spin waves. The effect of frequency, amplitude, and temperature are determined and illustrated with a phase diagram.

2.1 Skyrmion Creation

Spin wave control of a single magnetic skyrmion provides a mechanism for all magnonic skyrmion-based Boolean or non-Boolean information processing architectures. In a simple non-volatile memory array, the topological charge could serve as the state variable that could be 'read' using the topological Hall effect. [34] At spin wave amplitudes or frequencies below that required for annihilation, skyrmions scatter spin waves at specific angles. [23] Thus, skyrmions at cross-bar intersections act as the magnetic bits in a magnetic holographic memory architecture. [35]

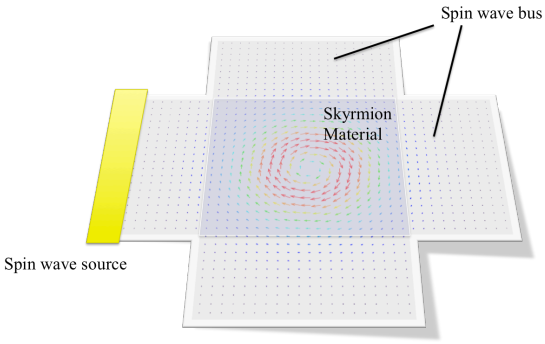

Figure 2.1: Schematic of the crossbar structure. The crossbar structure consist of two parts, the spin wave bus and the central region which has a DM interaction that stabilizes a skyrmion. A spin wave source is put at the left terminal for creation and annihilation.

The crossbar structure is shown in Fig. 1. The center area consists of a skyrmion host material such as a B20 helimagnetic compound that stabilizes the skyrmion. The horizontal and vertical spin-wave buses are ferromagnetic with low damping to support a spin wave. In such a structure, a single skyrmion will be confined in the center area by the potential boundary between the spin wave bus and the skyrmion material.

To study the dynamics of a skyrmion in this structure, we first consider the Hamiltonian of a two-dimensional square lattice [36]:

$$\mathcal{H} = \sum_{<i,j>} [-J\mathbf{S}_i \cdot \mathbf{S}_j + \delta D\hat{r}_{ij}\mathbf{S}_i \times \mathbf{S}_j] - \mu_B \sum_i \mathbf{S}_i \cdot \mathbf{h}_0, \tag{2.1}$$

where the first term is the Heisenberg exchange interaction and the second term is the

DM interaction. $\hat{r}_{ij}$ is a vector pointing from S_i to S_j and δ is 0 for the spin wave bus and 1 for the skyrmion material. The last term is the Zeeman term and μ_B is the Bohr magneton. The Landau-Lifshitz-Gilbert equation is solved by a fourth order Runge-Kutta method,

$$\dot{\mathbf{S}} = -\gamma \mathbf{S} \times \mathbf{H}_{eff} + \alpha \mathbf{S} \times \dot{\mathbf{S}} \tag{2.2}$$

where γ is the gyromagnetic ratio, α is the damping constant and $\mathbf{H}_{eff}$ is the effective field given by $\mathbf{H}_{eff} = -\frac{\partial \mathcal{H}}{\partial \mathbf{S}}$. Finite temperature is included with a stochastic field L to simulate the random field generated by finite temperature. With the finite stochastic field, the LLG equation becomes

$$\dot{\mathbf{S}} = -\gamma \mathbf{S} \times (\mathbf{H}_{eff} + \mathbf{L}) + \alpha \mathbf{S} \times \dot{\mathbf{S}} \tag{2.3}$$

The dissipation-fluctuation relation $\langle L_\mu(r,t) L_v(r^{'},t^{'})\rangle = \xi \delta_{\mu v} \delta_{rr'} \delta_{tt'}$ is is satisfied where $\xi = \alpha k_B T/\gamma$. The average $\langle \cdots \rangle$ is taken over all the realizations of the fluctuation field. The equation is solved by using the Heun scheme. [37] To precisely monitor the creation and annihilation process, a lattice version of the topological charge is employed to calculate the skyrmion number at each time step. [28] All units in our simulation are normalized to J. We choose $J = 1$, $D = 0.3J$, and $\alpha = 0.001$.

The central region is 30 by 30 sites and the entire structure is 300 by 300 sites. To stabalize the skyrmion, a background magnetic field $h_0 = 0.09$ is applied in the z direction to the entire domain so that the ground state of both the spin wave bus and the central region is a ferromagnetic state.

We first consider the skyrmion creation process. A spin wave is injected by applying an ac magnetic field $H_{ac} = A\sin(\omega t)$ at the source for a total time of 300 (in units of $1/J$). At the ends of the other three terminals, absorbing boundary conditions are employed to avoid spin wave reflection. The absorbing boundary conditions are

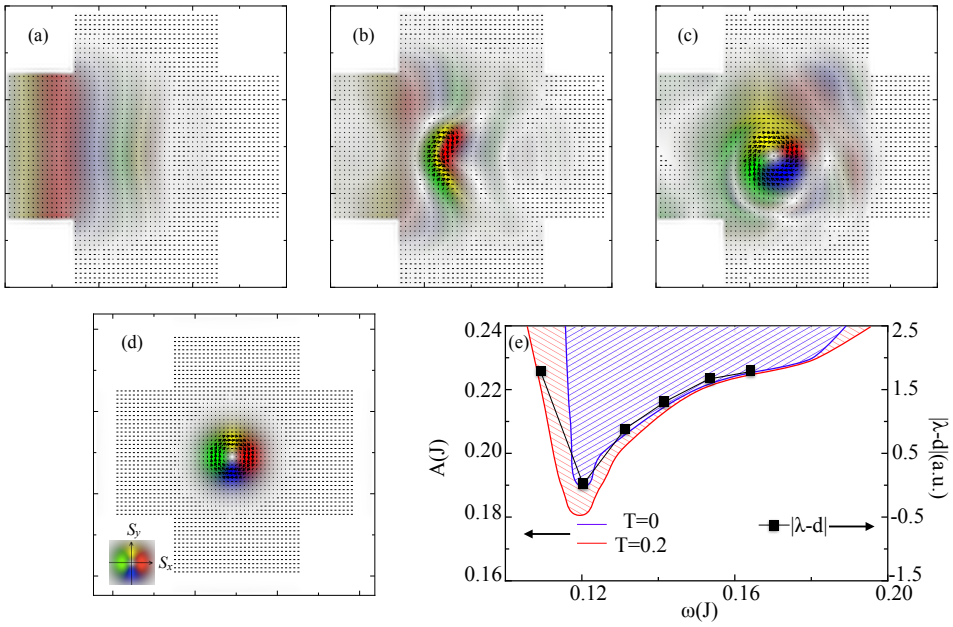

Figure 2.2: (a)-(d) Snapshots during skyrmion creation. The color in the snapshot represents different in-plane directions of the spin. The velocity of the injected spin wave in (a) picks up a transverse component as it enters the center region with the DM interaction in (b). The topological charge switches from 0 to 1 in (c) indicating the creation of a skyrmion. The skyrmion remains in (d) after the spin wave ceases. (e) Phase diagram showing the frequencies and amplitudes required for skyrmion creation at two different temperatures. Black squares indicate the difference between the wavelength of the spin wave and the diameter of the skyrmion.

implemented by exponentially increasing the damping constant α from 0.001 to 0.5 over 30 sites at the end of each terminal.

Time snapshots of the creation process are shown in Fig. 2 at zero temperature. Initially at t = 0, the spin wave is generated by the ac magnetic field and propagates in the positive x-direction. At t=100, the spin wave enters the central region which supports the DM interaction. The DM interaction acts as an effective vector potential on the spin wave giving rise to a transverse component to the velocity [38] causing the spin wave to propagate downward as it enters the central region. The spin wave amplitude in Fig. 2.2b is larger in the lower part of the the center region. The combination of

the geometry change between the lead and the central region and the effective magnetic field provided by the DM interaction is sufficient for this spin wave amplitude to evolve into a skyrmion. At the time step just after the topological charge becomes 1 in Fig. 2.2c, the skyrmion is located in the lower part of the center region. After the spin wave ceases in Fig. 2.2d, the skyrmion centers itself in the center region. The creation time for this process is 470 when the frequency is 0.12.

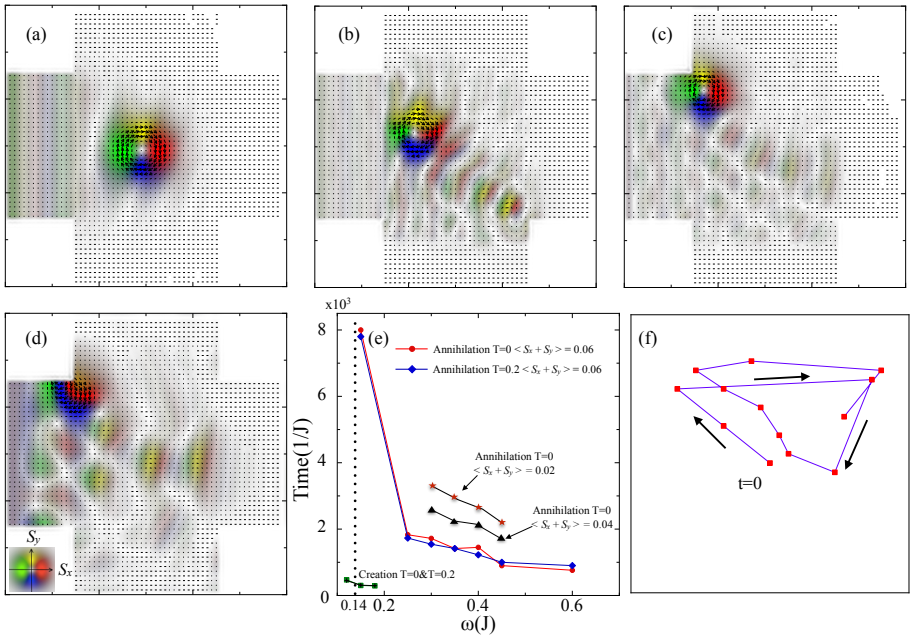

Figure 2.3: (a)-(d) Snapshots of the skyrmion annihilation process. The color scheme is the same as in Fig. 2. Upon injection of the spin wave, the skyrmion moves upward and to the left with a backwards scattering angle of approximately 30° as shown in (b) and (c). The spin texture in (d) is shown at the time step immediately after annihilation when the topological charge switches from 1 to 0. (e) Dependencies of the creation and annihilation times on the spin wave frequency and amplitude. (f) Trajectory of the skyrmion's center in the center region of the crossbar when $\omega = 0.14$, and the spin wave amplitude is 0.06. The frame of the plot represents the perimeter of the 30 by 30 center region. The total simulation time is 6×10^4.

Thermal fluctuations favor the skyrmion creation process, since the random field works together with the spin-wave excitation to overcome the energy barrier be-

tween the skyrmion state and the ferromagnetic state. Therefore, we also consider heat assisted spin-wave skyrmion creation. During spin wave injection, a heat source (such as a laser spot) could heat the cross section area. This is similar to heat assisted magnetic recording [39] and the method proposed in Ref. [30], but here, only a small temperature increase is required compared to the temperature required to exceed the Curie temperature.

A phase diagram showing the spin-wave amplitudes and frequencies required to create a skyrmion at both $T = 0$ and $T = 0.2$ is shown in Fig. 2.2e. At $T = 0$, spin waves with frequencies and amplitudes lying within the blue hatched region create skyrmions. At $T = 0.2$, spin waves with frequencies and amplitudes lying within the red and blue hatched region create skyrmions. Increasing the temperature allows skyrmion creation at slightly lower spin wave amplitudes and frequencies, but it does not affect the optimum frequency of $\omega = 0.12$ for skyrmion creation. The optimal frequency occurs when the wavelength of the spin wave matches the diameter of the skyrmion. The black squares in Fig. 2.2e show the magnitude of the difference between the spin-wave wavelength and the skyrmion diameter $|\lambda - d|$. The optimal frequency occurs when this difference is zero.

2.2 Skyrmion Annihilation

We next study skyrmion annihilation by an injected spin wave. A skyrmion provides an emergent magnetic field that can be written as $h_e = -\mathbf{S} \cdot (\partial_x \mathbf{S} \times \partial_y \mathbf{S})$ with the total flux $\int d^2r \; h_e = 4\pi Q$ and $Q = -1$ is the topological charge of a single skyrmion. [24] When a spin wave is injected from the left, this emergent magnetic field exerts a Lorentz force on the spin wave that deflects it downward and to the right. To

conserve momentum, the skyrmion moves upward and to the left. [23] Inspired by this property, we consider the possibility of annihilating a single skyrmion by dragging it out of the center region with a spin wave. Since there is no DM interaction to stablize a skyrmion outside the center region, the skyrmion will be annihilated.

Figs. 2.3a-d show the evolution of the spin texture resulting from an injected spin wave with amplitude $\langle \mathbf{S}_x + \mathbf{S}_y \rangle = 0.06$, frequency $\omega = 0.45$, and $T = 0$. At the initial state shown in Fig. 2.3a, a relaxed stable skyrmion is at the center of the crossbar, and the spin wave is just entering the center region. As the spin wave interacts with the skyrmion, the skyrmion moves upward and to the left with a backwards scattering angle of approximately 30° as shown in Figs. 2.3a-d. Right after the skyrmion moves outside the center region in Fig. 2.3d, it is annihilated due to the lack of DM interaction, and the magnitude of the topological charge switches from -1 to 0. At the boundary, there exists an energy barrier between the skyrmion material and the spin wave bus. Hence, the skyrmion can only be annihilated if it has enough energy to cross this boundary.

According to the previous study on magnon-skyrmion scattering [23], the velocity of the skyrmion depends on the frequency of the spin wave at a fixed amplitude. Fig. 2.3e plots the time that it takes to annihilate a skyrmion versus the frequency of the spin wave. The higher the frequency, the shorter the time, and this is consistent with an increased velocity with spin wave frequency. We also performed simulations for different spin wave amplitudes as shown in Fig. 2.3e. As the amplitude of the spin wave decreases, the time to destroy the skyrmion increases. This is consistent with the skyrmion velocity decreasing with decreasing spin-wave amplitude as was found in previous calculations of skyrmion velocity [20].

To overcome the potential barrier, there exists a critical frequency that is required to annihilate the skyrmion. In our simulation, the critical frequency is approxi-

mately 0.14 as indicated by the vertical dotted line in Fig. 2.3(e). As the frequency drops from 0.25 to 0.15, the time for annihilation increases. As the frequency approaches 0.14, the annihilation time rapidly increases. When $\omega = 0.14$, we do not observe skyrmion annihilation even when $t = 6 \times 10^4$ which is the longest time that we have run the simulations.

For $\omega \leq 0.14$, the skymion circulates inside the central region area as shown in Fig. 2.3f. This circulating motion is due to the backward motion of the skyrmion and the repulsion force that exists at the boundary between spin wave bus and skyrmion material. The frequency of this circulating motion is 3 orders of magnitude smaller than the frequency of the injected spin wave. In a uniform system, the skyrmion motion should satisfy Thiele's equation of motion [40], with a gyrovector $\frac{1}{4\pi}\int -\mathbf{S} \cdot (\partial_x \mathbf{S} \times \partial_y \mathbf{S}) d^2r = -1$ which is the topological charge of the skyrmion. The skyrmion will exert an effective Lorentz force on the injected spin wave that is connected to the topological charge by the emergent magnetic field of the skyrmion. However, the skyrmion is also subject to the forces resulting from the boundaries between the center region and the leads and the corners. The sum of these forces determine the skyrmion motion which must be calculated numerically.

Again, since thermal fluctuations influence the propagation of a spin wave, we re-do the above simulations at a finite temperature of $T = 0.2$. Like the results for skyrmion creation, the finite temperature results for skyrmion annihilation show little change with respect to the zero temperature results. Annihilation times for $T = 0$ and $T = 0.2$ with $\langle \mathbf{S}_x + \mathbf{S}_y \rangle = 0.06$ are plotted in Fig. 2.3e. The annihilation times are essentially the same at all frequencies, and the cutoff frequency remains the same for both temperatures.

To estimate values required for a specific material implementation, we use parameters for the insulating skyrmion material Cu_2OSeO_3. For Cu_2OSeO_3, $J = 4.3$ meV, $D = 0.26$ meV and $a = 1$ nm. For skyrmion creation, a 12 GHz, 300 Oe ac magnetic field is required at the lowest point in the phase diagram for $T = 0$. For skyrmion annihilation, a 30 Oe, 25 GHz ac magnetic field is required. The switching times for this skyrmion creation and annihilation are approximately 2.5 ns and 10 ns, respectively.

2.3 Possible Experimental Scheme

Fabrication of such a structure could be performed in several ways. In one, the Yttrium-Iron-Garnet(YIG) can be deposited and etched into cross bars with a hole in the central region, and then the DM material can be deposited in the central region. It is worth mentioning here that our results also apply to Néel type skyrmions which are stabilized by an interfacial DM interaction in layered structures. For a structure with Néel type skyrmions confined in the central region, one could fabricate the entire crossbar geometry with YIG and then deposit a heavy metal on top of the center region thus inducing an interfacial DM interaction in the center region only.

Skyrmion creation results from the geometry change in the crossbar combined with the effective gauge field provided by the DM interaction acting on the spin wave. Skyrmion annihilation results from the emergent magnetic field of the skyrmion acting on the spin wave and the conservation of momentum between the spin wave and the skyrmion. A critical frequency is required both for the creation and the annihilation of a skyrmion. The heat assisted method for skyrmion creation reduces the minimum frequency required for creation. The minimum frequencies for creation and annihilation

are similar, but the optimum frequency for creation that requires minimum spin-wave amplitude is below the critical frequency for skyrmion annihilation. If a skyrmion already exists in the cross bar region, a spin wave below the critical frequency causes it to circulate within the central region at an angular frequency about 3 orders of magnitude below the spin wave frequency.

Chapter 3

Shape dependent resonant modes of skyrmions in magnetic nanodisks

Skyrmions can be stabilized in a confined geometry without an external magnetic field [41, 42]. The shape dependent boundary conditions in confined geometries can give rise to different magnetic solitons and their interesting dynamics, such as the pinning and creation of a domain wall [43]. Skyrmion dynamics in confined geometries are very different from that in infinite planes or bulk samples [31, 44, 45]. The boundary plays a crucial role when the sample size is comparable to the size of the skyrmion. Thus, understanding skyrmion dynamics in different confinement geometries is an important step towards practical applications.

In this chapter, we investigate the spin wave modes of a single Néel type skyrmion confined in nanodisks with aspect ratios (ARs) ranging from a circular nanodisk with AR=1 to an elliptical nanodisk with AR=2. We focus on the power spectrum

for the out-of-plane (perpendicular to the disk) resonant modes of the skyrmion and its dependence on the AR. The dynamical pattern of each mode has been identified by the spatial map of both the magnetization fluctuations and its power spectral density (PSD). For comparison, the power spectra of ferromagnetic (FM) states in the same geometries have also been calculated.

3.1 Micromagnetic Model

To study the skyrmion dynamics in a nanodisk, we consider a thin magnetic nanodisk with perpendicular magnetic anisotropy (perpendicular to the disk plane) and an interfacial type DM interaction [46]. The Hamiltonian can be written as:

$$\mathcal{H} = \int dr^3[-A(\nabla \mathbf{S})^2 - D\mathbf{S} \cdot [(\mathbf{z} \times \nabla) \times \mathbf{S})] - K_u(S_z)^2 - \mu_0 M_s \mathbf{S} \cdot \mathbf{H} + W_{\text{dip}}], \quad (3.1)$$

where $\mathbf{S}$ is the unit vector of magnetization, and μ_0 is the magnetic constant. The first and second terms are the Heisenberg exchange energy and the DMI energy, respectively. The third term is the anisotropy energy, the fourth term is the Zeeman energy, and the last term is the dipolar interaction energy. The micromagnetic simulations were carried out by solving the Landau-Lifshitz-Gilbert equation with the Mumax3 code [47],

$$\dot{\mathbf{S}} = -\gamma \mathbf{S} \times \mathbf{H}_{eff} + \alpha \mathbf{S} \times \dot{\mathbf{S}} \quad (3.2)$$

where γ is the gyromagnetic ratio, α is the damping constant and $\mathbf{H}_{\text{eff}}$ is the effective field given by $\mathbf{H}_{\text{eff}} = -\frac{1}{\mu_0 M_S} \frac{\partial \mathcal{H}}{\partial \mathbf{S}}$. An exchange constant $A = 15$ pJ/m, a perpendicular anisotropy constant $K_u = 900$ kJ/m^3, a DMI $D = 3$ mJ/m^2 and a saturation magnetization $M_s = 1$ MA/m are used for all simulations. A small damping constant $\alpha = 0.001$ is employed to get a better resolution of the spin wave modes in the spectrum. The geometry of the nanodisk is $l \times 100 \times 1$ nm and the AR is defined as $l/100$.

After the skyrmion is completely relaxed, a time dependent magnetic field $h_{ac}(t) = h_z \frac{\sin(2\pi\omega_c t)}{2\pi\omega_c t}$ with $h_z = 0.5$mT and a cut-off frequency $\omega_c = 50$ GHz is applied to excite the skyrmion ground state [44, 45, 48]. The evolution of the averaged magnetization at each time step is recorded and the power spectrum is calculated by performing a Fourier transform of the recorded data. To resolve resonant modes at different frequencies, an ac magnetic field $h_{ac}(t) = h_z \sin(2\pi\omega t)$ with $h_z = 0.5$mT is used. The time evolution of magnetization at each mesh point is saved to generate the spatial maps of the magnetization fluctuations and their Fourier transforms.

3.2 Spectrum Results and Discussions

We first examine the static spin texture of skyrmions at different ARs and the results are summarized in Fig. 3.1. As indicated from the distribution of the $\hat{z}$ component of the magnetization m_z shown in Fig. 3.1(a) and (b), the magnetization at the edge always tilts away from the easy-axis, which is due to the open boundary condition of the nanodisk and the DMI. While the skyrmion radius along the x-axis (long axis) always expands with increasing AR, the skyrmion radius along the y-axis (short axis) remains unchanged for AR<1.5 and begins to slightly shrink when AR>1.5. The AR of the skyrmion can be extracted from the m_z distributions along x-axis and y-axis, and the relationship between the skyrmion AR and the disk AR has been plotted in the inset of Fig. 3.1(b). For AR<1.5, the skyrmion AR nonlinearly increases with the disk AR, and for AR>1.5, the skyrmion AR has a linear relation with the disk AR. Furthermore, except for the trivial circular disk with AR=1, the skyrmion AR is not strictly equal to the disk AR especially when the disk AR>1.5. The dipolar field plays an important role in determining the shape and stability of the skyrmion in

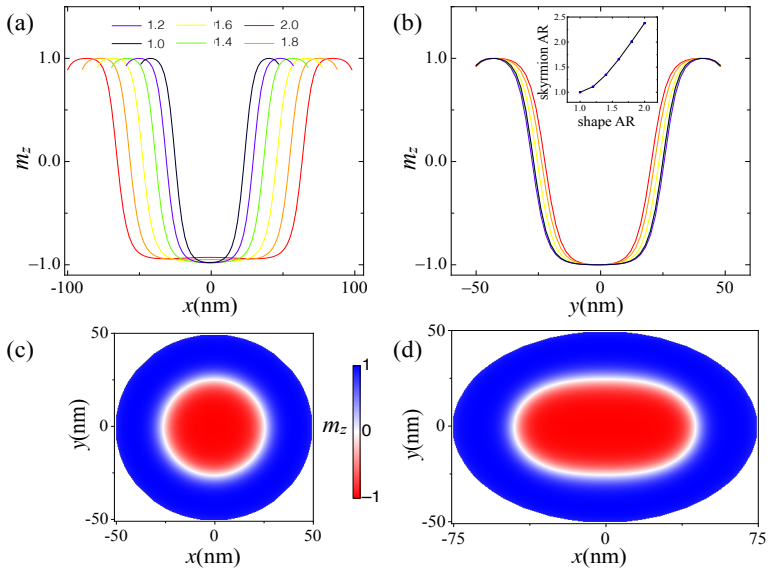

Figure 3.1: Magetization distributions of skyrmion at different ARs along (a) x-axis and (b) y-axis. Inset is the skyrmion AR as a function of the disk AR. (c) and (d) are the spatial distributions of m_z at AR=1 and AR=1.5, respectively.

these nanodisks. Distortion of the skyrmion is a result of the dipolar field in different geometries, where the rotational symmetries of both the nanodisk and the skyrmion are broken. It is also worth mentioning that if we keep increasing the disk AR all the way to 2.5, the skyrmion is no longer the ground state, but a multi-domain state becomes the lowest energy state as a result of the strong in-plane dipolar field in large AR disks.

We next calculate the power spectrum as a function of the disk AR. A color plot of the power spectrum from AR=1.0 to AR=2.0 is shown in Fig. 3.2(a). When AR=1, there are three featured modes in the spectrum. Mode A with the lowest frequency of 4.3 GHz is not sensitive to the AR. Frequencies of the other two, mode B at 27.8 GHz and mode C at 43.5 GHz, decrease nonlinearly with the AR. Other than the initial three spin wave modes observed at AR=1, several extra modes emerge when the AR goes up. Below 10 GHz, two modes with strong amplitudes begin to appear. The first one with lower frequency emerges immediately after the AR deviates from 1, while the

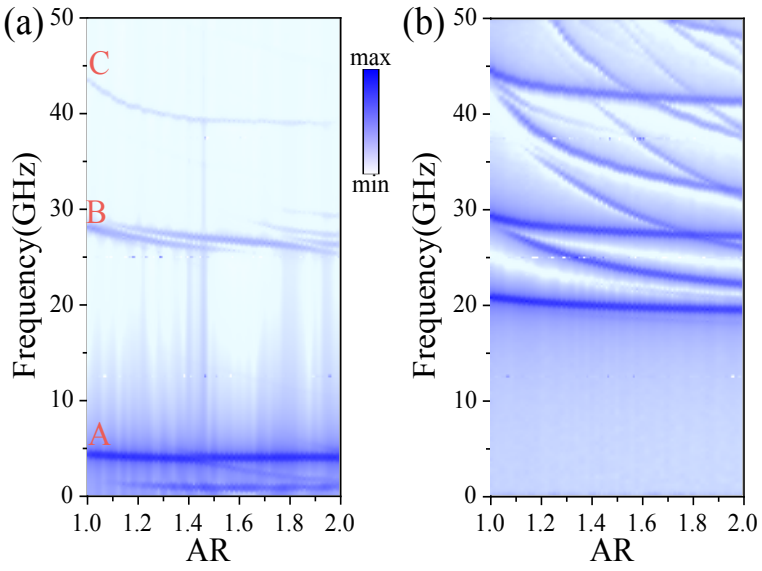

Figure 3.2: Power spectrum as a function of the disk AR for (a) single skyrmion and (b) ferromagnetic state.

other mode with higher frequency emerges from mode A at AR=1.4. On the other hand, mode B splits into two modes when the AR increases, and when the AR is around 1.7, three additional new modes closely related to mode B appear in the spectrum.

As a comparison, the power spectrum for a trivial FM state was calculated in the same geometry, as shown in Fig. 3.2(b). There are also three modes observed at AR=1, and they have similar trends that decrease nonlinearly with increasing AR. Similar to the skyrmion case, new modes are emergent at large AR, most of them are related to the collective modes at the edge with broken rotational symmetry. However, the lowest frequency mode of the FM state has a much higher frequency than that of the skyrmion, which is consistent with previous studies [44]. Also, there is no new mode splitting from the lowest mode of the FM, which is completely different from the skyrmion spectrum. This difference suggests that the lowest resonance mode could be used as a signature of the skyrmion state, and furthermore, could be used to check the AR of a given sample.

To resolve and understand different resonant modes, we plot the snapshots of real time magnetization fluctuations and the spatial FFT power of the nanodisk at AR=1.0 and AR=1.8 respectively, as shown in Fig. 3.3. When AR=1.0, there are three modes as mentioned above. Mode A is a breathing mode with the magnetization fluctuating locally around the core of the skyrmion. Mode B is a hybridized breathing mode with a strong magnetization fluctuation at the disk edge. Mode C is similar to mode B, but instead of the disk edge, the magnetization fluctuates mostly around the skyrmion core. These modes have been well studied before [44] and are employed here merely as a reference.

Once the AR is elevated to 1.8, there are 13 significant peaks in the power spectrum, which will be identified below. The lowest frequency mode is a new mode labeled D at 0.85 GHz instead of mode A. It is a rotation mode around the core in a clockwise (CW) direction with four nodes. The four nodes are all out-of-phase with their neighboring nodes. Mode A is split into two modes A1 and A2. Mode A1 at 2 GHz is also a CW rotation mode but with eight nodes, and the nodes are also out-of-phase with their neighbors. Mode A2 at 4.05 GHz is very similar to its parent breathing mode A at AR=1.0, but hybridized with a very small amplitude of oscillation. These low lying modes D, A1, and A2 are the dominant modes over the whole spectrum. Mode E at 6.05 GHz is a CW rotation mode with 12 nodes, which are again out-of-phase with their neighbors. Mode F is at 11.3 GHz with a counterclockwise (CCW) rotation of two connected large nodes, and the rotation is always in-phase around the skyrmion core. All of the five resonant modes at AR=1.8 discussed so far are lower than the lowest frequency mode in the FM case regardless of its AR.

Modes B1 to B4 have similar spatial map patterns, and they all involve a four-node oscillation hybridized with breathing, although the trajectory of nodes and the

magnetization fluctuations near the disk edge are different. For mode B1 at 25 GHz, the nodes located on the long axis have larger amplitudes than those on the short axis. They all oscillate around their own axis, and there is also a small fluctuation near the edge along the long axis. Mode B2 at 25.9 GHz has a similar oscillation as B1, but the amplitudes of the node along long axis and short axis are almost the same. It also involves a stronger breathing mode and a strong magnetization fluctuation near the edge along both axises. Mode B3 at 26.7 GHz has stronger nodes along the short axis. It consists of both a strong oscillation and a strong breathing mode, and the magnetization fluctuations near the edge along both axes have significant amplitudes. Similar to B3, B4 at 27.5 GHz has an oscillation trajectory, but the node with stronger amplitude is located on the long axis. The trajectory of the node on the short axis is slightly tilted, and the magnetization fluctuations near the edge are not strictly on the axis. Mode G at 29.7 GHz and mode H at 33 GHz have small oscillation amplitude, and their nodes on the long axis have larger amplitude. The trajectory of G is a little differerent from H, the edge mode of H is close to the short axis while the edge mode of G is close to the long axis. These 6 modes have similar patterns of hybridization between oscillation and breathing, and they could be distinguished from each other by the oscillation trajectory, node amplitude or fluctuations near the edge.

The last two modes are C1 at 39.1 GHz and I at 46.2 GHz. C1 is closely related to mode C at AR=1.0, but now it is mixed with an oscillation mode. There are two radial spin wave modes with strong amplitude along the short axis, but only one radial mode along the long axis. The magnetization fluctuation at the edge is along the short axis in C1. Mode I has two radial spin wave modes along both long and short axis, but the oscillation center of its four nodes is off-axis.

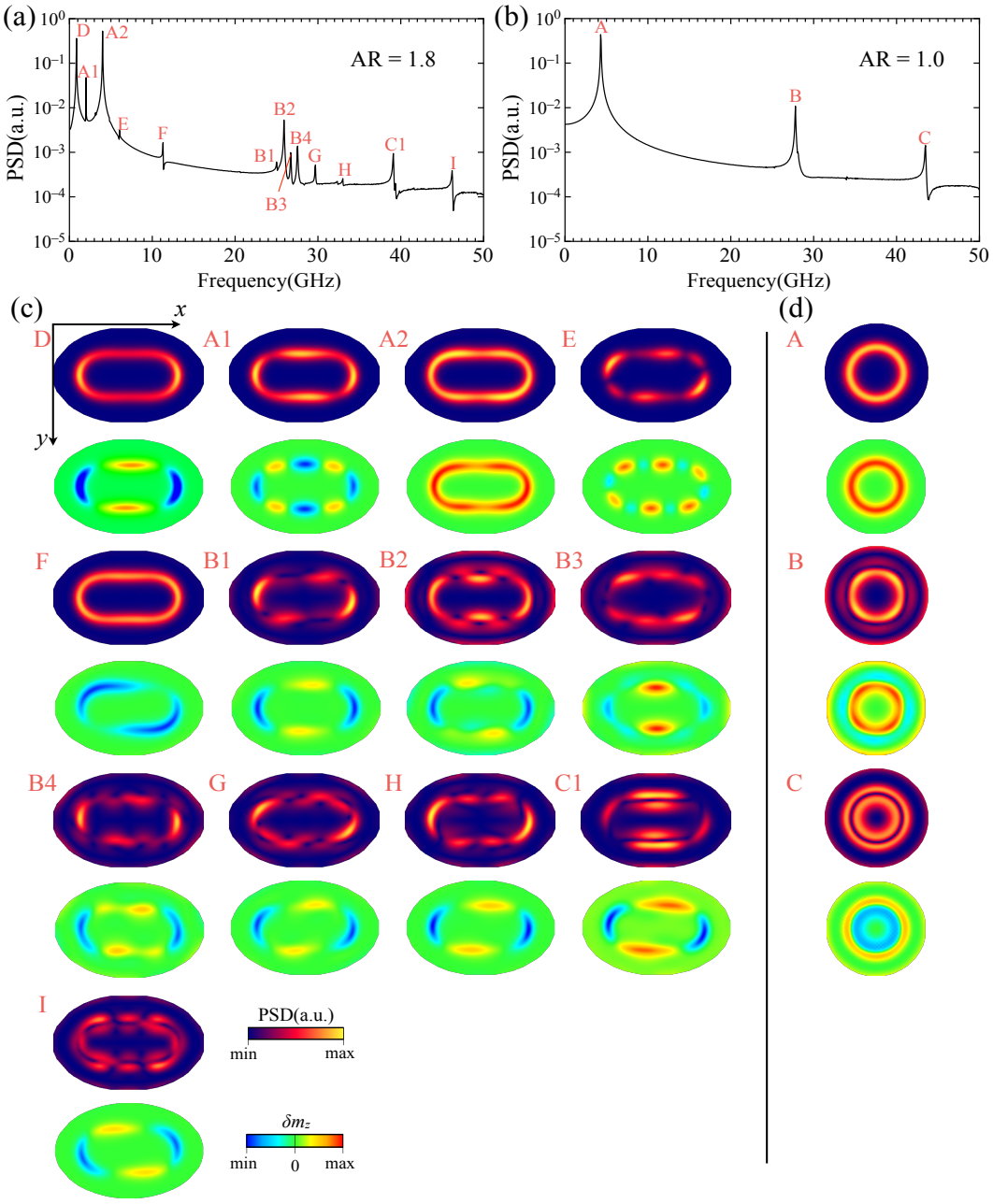

Figure 3.3: Power spectrum at (a) AR=1.8 and (b) AR =1.0. (c) and (d): Spatial map of the magnetization fluctuation snapshot(bottom) and the FFT amplitude(top) associated with different resonant modes in the power sepctrum. For each mode, one reprensentative magnetization fluctuation snapshot is slected from series of snapshots within one excitation period and the FFT data is collected from the magnetization dynamics over 30 excitaion periods.

Compared to the original three modes at AR=1, the modes at AR=1.8 are in general hybridized with a rotation or oscillation mode and all contain an azimuthal component which is introduced by the increasing AR. Obviously from the resolved modes, the rotational symmetry is broken in this system and thus many azimuthal components of the spin wave mode appears. Only mode A2 still shows an in-phase breathing mode around the skyrmion core. However, a very weak azimuthal component is observed along the short axis in A2, which is again a sign of the rotation symmetry breaking. Only the modes below 20 GHz are involved in a rotation motion except for mode A2, and only mode F has a CCW direction rotation. Mode B1 to H are all oscillation modes with a radial mode number equal to 1 while mode C1 and I have a radial mode number equal to 2. Although all the modes are hybridized with other motions, we can still observe the signature of their parent modes at AR=1.0. For example mode A2 is almost the same with mode A, both of which are a breathing mode. Mode B1 to B4 still show a signature of mode B, where the magnetization fluctuation near the edge has a significant amplitude. Mode C1 shows two strong radial modes, which are similar with mode C.

In general for a skyrmion in an infinite plane, the spin wave mode is governed by the short range interactions such as the Heisenberg exchange and DMI. However, in confined geometries with the sizes comparable to the skyrmion diameter, the long range dipolar interaction plays an important role, particularly in generating different resonant modes, while the short range interactions (exchange and DMI) determine basic properties of the modes such as the frequency and the spacing between different modes.

To conclude, the out-of-plane spin wave modes of a confined skyrmion in nanodisks with different ARs are studied using micromagntic simulations. The skyrmion AR increases nonlinearly with increasing disk AR. New mixed modes appear in the spectrum with increasing AR, which originate from geometrical confinement and bro-

ken rotational symmetry of both the nanodisk and the skyrmion. The lowest mode of the skyrmion is still well below the first eigenmode of the FM state in the same geometry. Furthermore, two new modes appear below the lowest mode of the skyrmion with increasing AR, whereas in the FM state, no additional mode appears below the lowest frequency mode. This property can be used for measuring the skyrmion and AR in non-axial symmetric systems. New rotation and oscillation modes with different azimuthal and radial components are identified at AR=1.8, which still have characteristics of their original modes at AR=1.0. This study provides insight into the effect of asymmetry on skyrmion dynamics in confined nanodisk geometries. Such understanding is a step towards skyrmion based spin torque oscillators and spin wave sources [49].

Chapter 4

Hopfion in Chiral Magnet Nanodisk

A topological soliton carries an integer topological index that cannot be changed by a continuous deformation [50]. A celebrated example is the skyrmion, a two-dimensional (2D) topological soliton originated from the Skyrme model [51], which can be characterized by the skyrmion number (or winding number) [52]. The addition of a third spatial dimension brings more diverse and complicated topological solitons, such as rings, links and knots [53–55]. Some of these three-dimensional (3D) topological solitons are "hopfions", since they can be classified by the Hopf invariant (Q_H) [56], a topological index of the homotopy group $\Pi_3(S^3)$ that can be interpreted as the linking number [57]. Due to their complex structures and models, the detailed study of the hopfion was properly established not long ago in terms of toroidal coordinates [58, 59]. Hopfions have been observed in a variety of physical systems including fluids, optics, liquid crystals, Bose-Einstein condensates, etc. [60–66] But its feasibility in magnetic materials remains elusive.

In magnetic systems, topological solitons in one dimension and two dimensions such as domain walls and vortices have been extensively studied over the past few decades. Much of the recent attention is attracted by the magnetic skyrmions residing in magnetic materials with the antisymmetric Dzyaloshinskii-Moriya interaction (DMI) [9, 10, 67]. The spins of a magnetic skyrmion wind around the unit sphere once, which results in the unit winding number of a skyrmion. Skyrmions are proposed to be promising candidate for spintronics applications due to their prominent features such as the nanoscale size and low driving current density [6, 21].

Although numerous studies have been made on the low-dimensional topological solitons, 3D topological solitons like hopfions have still not been well explored so far in nanomagnetism. Understanding the static and dynamical properties of these 3D topological solitons are not only of fundamental interest, but may also enable future applications. Only a few theoretical proposals predict the existence hopfions in ferromagnets, but only in the dynamical regime [68–70]. It has been recently proposed that a higher order exchange interaction and an external magnetic field will stabilize a hopfion in a frustrated magnet [71].

In this Chapter, we show that a $Q_H = 1$ hopfion can be simply enabled in a chiral magnet nanodisk in the absence of external magnetic fields. The nanodisk is sandwiched by two magnetic layers with perpendicular magnetic anisotropy (PMA) to nucleate the hopfion therein. The hopfion is identified by both the preimages and the numerical calculations of Q_H. Associated with the hopfion, another non-trivial state that includes a monopole-antimonopole pair (MAP) is also stabilized at zero fields in this structure. The topological transition between the hopfion state and the MAP state involves the creation (annihilation) of the monopole-antimonopole pair and a twist of the preimages.

4.1 Theoretical Model

We consider a chiral magnet nanodisk sandwiched by two magnetic thin layers with PMA, as shown in Fig. 4.1(a). A B20 compound such as the FeGe is employed to model the chiral magnet, such that the DMI is of the isotropic bulk type. The Hamiltonian of this system is given by

$$\mathcal{H} = \int dr^3[-A(\nabla \mathbf{s})^2 - (1-\mathrm{p})D\mathbf{s}\cdot(\nabla\times\mathbf{s}) - \mathrm{p}K_u(s_z)^2 + E_\mathrm{d}], \tag{4.1}$$

where A and D are the exchange and DMI constant, respectively, K_u is the PMA constant and p is 0 for the chiral magnet nanodisk and 1 for the magnetic thin nanodisks. E_d is the magnetic dipole-dipole interaction (DDI). E_d depends on the exact shape of the system. When the system size goes down to nanoscale, the DDI becomes important in determining the corresponding spin textures. For example, the DDI favors the stabilization of magnetic skyrmion at zero-field in confined geometries. It leads to the formation of the so-called target skyrmion, which has been theoretically proposed and recently experimentally observed in magnetic nanodisks without any external fields [72–75]. Thus, the effect of DDI is essential in confined systems and cannot be ignored.

We minimize the Hamiltonian (4.1) in the nanodisk structure with different initial states at various radii and thicknesses [1]. After minimizing the energy, we find two stable non-trivial states at zero-field, the hopfion state and the MAP state. The hopfion state includes a $Q_H = 1$ hopfion, and the MAP state includes a monopole-antimonopole pair.

[1] Micromagnetic simulations were performed using Mumax3 [76], Fidimag [77] and an in-house micromagnetic simulation package.

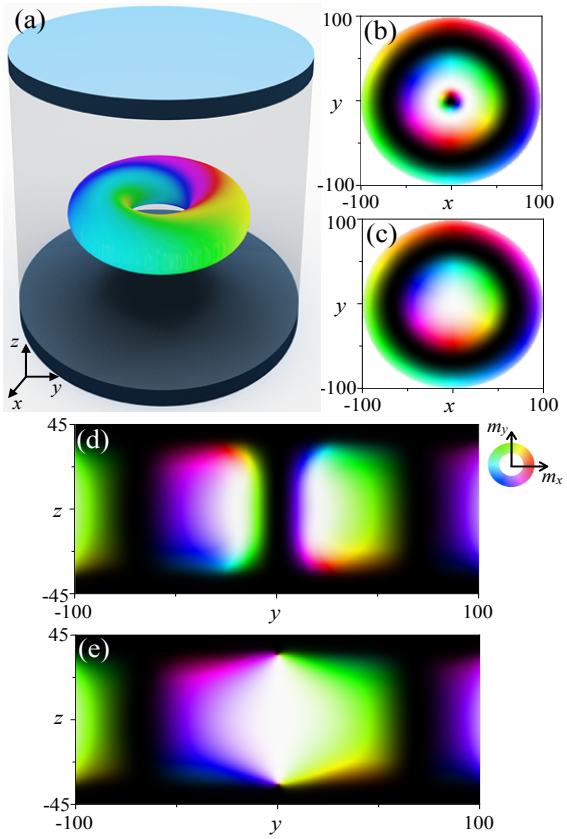

Figure 4.1: (a) Schematic of the proposed structure. The thin disks at the top and bottom represent the magnetic films with PMA. The transparent region in the middle is the chiral magnet nanodisk. The color ring at the center represents the set of preimages with $s_z = 0$ of a $Q_H = 1$ hopfion. (b), (c) The cross-sectional spin textures in the x-y plane (z=0) for the hopfion (b) and MAP (c). (d), (e) The cross-sectional spin textures in the y-z plane (x=0) for the hopfion (d) and MAP (e). In the color scheme, black indicates $s_z = -1$ and white indicates $s_z = 1$. The color wheel is for $s_z = 0$. The spin texture plot is for a chiral magnet nanodisk with radius 100 nm and thickness 70 nm.

4.2 Hopfion Spin Texture and Preimage

To present the detailed spin textures of the hopfion and MAP, cross-sections of both states are plotted in Fig. 4.1. For the hopfion, the cross-section in the x-y plane (z=0) shown in Fig. 4.1(b), has a skyrmion at the center surrounded by two concentric spin helical rings. This is typically a target skyrmion configuration recently observed in an FeGe nanodisk [75]. The hopfion consists of the central skyrmion and its nearest spin helical ring. The outer spin helical ring is not part of the hopfion but an edge state induced by the DDI from the circular shape and the DMI from the chiral magnet. The cross-section spin texture at the y-z plane (x=0) shown in Fig. 4.1(d) includes a skyrmion–antiskyrmion pair. The cross-section taken at any plane containing the z-axis always contains a skyrmion–antiskyrmion pair. This is a result of the hopfion spin texture that consists of a 2π twisted skyrmion tube with its two ends glued together as shown in Fig. 4.1(a). For the MAP state, the cross-section in the x-y plane (z=0) shown in Fig. 4.1(c) is a typical skyrmion, one helix ring less than the hopfion state. The cross-section in the y-z plane (x=0) shown in Fig. 4.1(e), has only one spin up region, in contrast to the skyrmion–antiskyrmion pair of the hopfion. Instead, a monopole (antimonopole) is formed near the top (bottom) surface. This originates from the restricted spin polarization of the PMA layers on the top and bottom.

To further visualize and understand the spin configurations of the hopfion and MAP in 3D, we plot their preimages using Spirit [78]. A preimage is the region in 3D real space that contains spins with the same orientations. It is a Hopf map of a point on the S^2 unit sphere to 3D space. We first plot the set of preimages of all spins with $s_z = 0$ for the hopfion (Fig 4.2(a)) and MAP (Fig. 4.2(c)), which corresponds to a Hopf map from the equator of the S^2 unit sphere to the 3D space. Two preimages are topologically

distinct as characterized by different genus g, i.e., the number of holes. The preimage of the hopfion forms a torus with $g = 1$, whereas the preimage of the MAP is a trivial surface with $g = 0$, which satisfies the Poincaré-Hopf theorem [79].

The Hopf invariant, also called the linking number, counts the number of links between two arbitrary closed-loop preimages. Therefore, preimages of two arbitrary spins must form closed loops that are linked with each other. These features can be identified in plots of the preimages of $\mathbf{s} = (1, 0, 0)$ and $\mathbf{s} = (-1, 0, 0)$ for the hopfion (Fig. 4.2(b)) and MAP (Fig. 4.2(d)). For the hopfion, two closed-loop preimages are formed and linked with each other once. $Q_H = 1$ in this case, and the topology of the hopfion state in this system is confirmed. In contrast, the MAP does not have closed-loop preimages and thus no links. The two MAP preimages of $\mathbf{s} = (1, 0, 0)$ and $\mathbf{s} = (-1, 0, 0)$ join at the monopole and antimonopole indicating their singular natures. The MAP is considered a defect state, while the hopfion is a smooth spin texture with no singularity. These preimages successfully reflect the topological natures of the hopfion and MAP.

4.3 Hopf Index

Other than the linking number of the preimages, the topology of the hopfion can also be confirmed by directly calculating the Hopf invariant. The integral form of the Hopf invariant in real space can be expressed as [80, 81]

$$Q_H = -\int \mathbf{B} \cdot \mathbf{A} d\mathbf{r}, \tag{4.2}$$

where $B_i = \frac{1}{8\pi}\epsilon_{ijk}\mathbf{n} \cdot (\nabla_j \mathbf{n} \times \nabla_k \mathbf{n})$ is the emergent magnetic field associated with the spin textures, and $\mathbf{A}$ is any vector potential that satisfies the magnetostatic equation

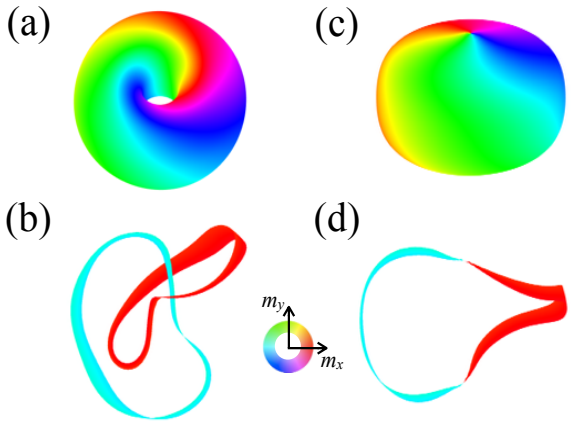

Figure 4.2: (a), (c) The set of preimages with $s_z = 0$ for the hopfion and MAP, respectively. (b), (d) The preimages of $\mathbf{s}$ =(-1,0,0) (cyan) and $\mathbf{s}$ =(1,0,0) (red) for the hopfion (b) and MAP (d).

$\nabla \times \mathbf{A} = \mathbf{B}$. The Hopf number is invariant under a gauge transformation $\mathbf{A} \rightarrow \mathbf{A} + \nabla\chi$ only when the emergent field $\mathbf{B}$ is free of singularities, *i.e.*, $\nabla \cdot \mathbf{B} = 0$. Cross-sections in the y-z plane of the emergent magnetic fields $\mathbf{B}$ of the hopfion and MAP states are shown in Fig. 4.3. The emergent $\mathbf{B}$ field of the hopfion shown in Fig. 4.3(a) flows smoothly and concentrates near the center of the nanodisk. In contrast, the emergent $\mathbf{B}$ field of the MAP shown in Fig. 4.3(b) has two magnetic monopoles with opposite charges near the top and bottom surface. The Hopf invariant is thus ill–defined for the MAP state, and it is well defined for the hopfion texture.

A gauge field solution $\mathbf{A}$ must also be solved in order to directly calculate Q_H in real space. To this end, we solve for the vector potential $\mathbf{A}$ in momentum space with the Coulomb gauge $\mathbf{k} \cdot \mathbf{A} = 0$, and then compute Q_H in momentum space [82]. Hopfion textures with different grid numbers (N_{tot}) are employed to validate this method. As shown in Fig. 4.3(c), as the grid number increases, Q_H rapidly converges to 1. We obtain a Hopf invariant of $Q_H = 0.96$ for the hopfion spin texture under investigation. Q_H is not an integer due to the finite size and open boundary condition. The manifold

is not compact, as indicated by the edge state around the disk boundary. Nevertheless, the Hopf invariant is close to 1, and the topological nature of the hopfion is further confirmed.

4.4 Topological trasition

Since the hopfion is topologically protected by the nonzero Hopf invariant, a topological transition must take place between the hopfion and MAP states. To investigate this topological transition, we performed a minimal energy path (MEP) calculation between these two states [83–85]. The MEP calculation is carried out using the geodesic nudged elastic band (GNEB) method associated with the Hamiltonian in Eq. (4.1). We consider a chiral magnet nanodisk with radius $r = 100$ nm and thickness $d = 70$ nm sandwiched by two magnetic thin nanodisks with thickness $d_{\mathrm{PMA}} = 10$ nm for the MEP calculation. For this size of system, the hopfion is a metastable state, and the MAP is the ground state. The stable spin textures from the energy minimizations are employed as the initial states in the MEP calculation.

Results from the MEP calculation are shown in Fig. 4.4(a). There exists an energy barrier between the hopfion and the MAP state. Thus, an activation energy is required to enable the transition from the hopfion (MAP) to MAP (hopfion) state. To capture details of the topological transition, we plot preimages of $\mathbf{s}$ =(1,0,0) and $\mathbf{s}$ =(-1,0,0) at the initial hopfion state, the barrier peak, the intermediate MEP state and the final MEP state (Fig. 4.4(b)-(e)). Transitioning from the hopfion state in (b) to the intermediate state (d), the two linked preimages break and reconnect generating the monopole–antimonopole pair with a 2π rotation. The two preimages are then topologically equivalent to those of the MAP state in Fig. 4.4(e), although they are twisted

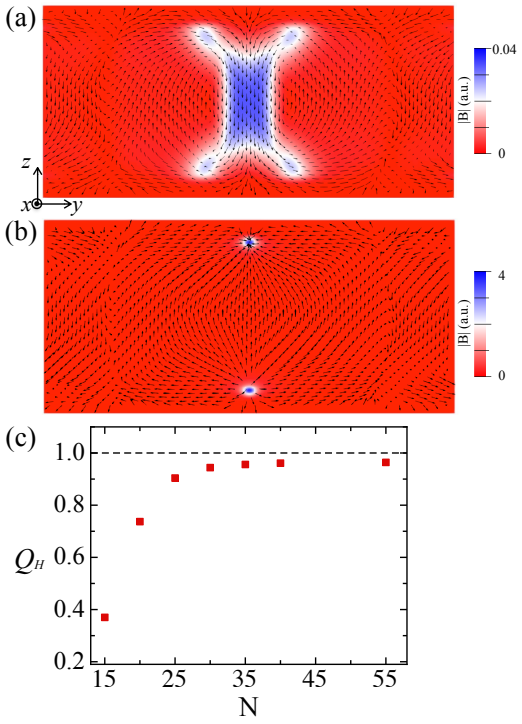

Figure 4.3: (a), (b) The emergent magnetic field **B** in the y-z plane (x=0) for hopfion (a) and MAP (b). (c) Numerical calculations of the Hopf invariant Q_H for different meshes. The total number of grid points $N_{tot} = N^3$.

by 2π. Relaxing from point (d) to to the MAP state of point (e), the preimages untwist to π, and the monopole and antimonopole move towards the top and bottom surface respectively. Videos of the transition also capture the transformation from a torus ($g = 1$) to a trivial surface ($g = 0$) for the preimages of $s_z = 0$ (see Movie1 and Movie2 in the Supplemental Materials). To create a hopfion from a MAP state, the reverse process is applied. The preimages first rotate from π to 2π. The monopole–antimonopole pair move towards each other until they eliminate each other. Then each preimage becomes close-looped and linked with the other preimage. In general, a hopfion can be created from a trivial state (e.g. ferromagnetic state) by creating a MAP, twisting the MAP by 2π and finally annihilating the MAP to form a smooth spin texture [86], as shown in Fig. 4.4(f).

4.5 Discussion

The hopfion is a 3D spin texture and a finite thickness of the sample is required to stabilize it. The length scale of the hopfion in the proposed structure is related to the ratio of the exchange interaction and DMI, which is the helical period L in chiral magnets. As shown in Fig. 4.1(d), the spin texture of the hopfion in the y-z plane includes a skyrmion–antiskyrmion pair. Thus, the radius and thickness of the chiral magnet nanodisk should be at least comparable to L.

This is confirmed by the calculated phase diagram of the magnetic ground state as a function of the nanodisk radius r and thickness d shown in the inset of Fig. 4.4(a). Here, L is 70 nm for our simulation parameters. For r and d small compared to L, the ground state is a ferromagnetic–like state in which the spins at the disk center have a ferromagnetic texture and the spins at the edges have in–plane components due to the

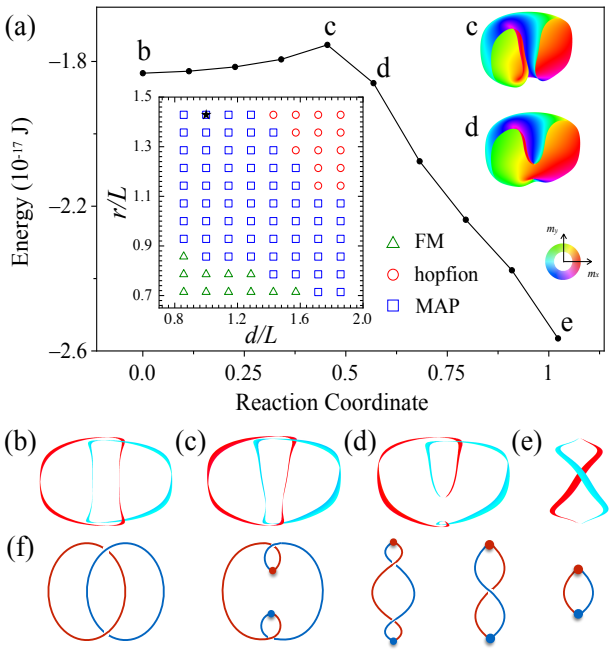

Figure 4.4: (a) Minimal energy path of the spin texture in the nanodisk of Fig. 4.1 with radius $r = 100$ nm and thickness $d = 70$ nm. Points b and e represent the hopfion and the MAP, respectively. The hopfion is nearly annhilated at saddle point c, and the MAP is created at d. Insets show the half-plane view preimages of $s_z = 0$ for spin textures at c and d and the phase diagram of the nanodisk. The phase diagram gives the ground state spin texture as a function of the nanodisk radius and thickness normalized to the helical period $L = 70$ nm. The black star indicates the parameters used for the MEP calculation. (b)-(e) The preimages of $\mathbf{s}$ =(-1,0,0) (cyan) and $\mathbf{s}$ =(1,0,0) (red) corresponding to points b–e in (a). (f) From right to left, the process of creating a hopfion out of a trivial state. The red and blue dot represents the monopole and antimonople, respectively.

DMI and magnetic dipole interaction. As r and d increase, the MAP state becomes the ground state. For even larger values of r and d such that $r > 1.1L$ and $d > 1.3L$, the hopfion becomes the ground state. As r and d continue to increase, multiple skyrmion states and more complicated spin textures appear. Also, as demonstrated by the MEP calculation, even in the regions where the MAP is the ground state, a hopfion can be created out of a MAP state by injecting sufficient activation energy, which could be experimentally achieved by a method such as a field quench.

Chapter 5

Spin Josephson effects in Exchange coupled Antiferromagnetic Insulators

5.1 Introduction

One main objective in the field of spintronics is the generation and manipulation of pure spin currents in magnetically ordered systems. Pure spin currents in magnetic insulators are carried by collective excitations. This can be achieved by combining elements of conventional spintronics with magnetic insulators [87], for example, magnon mediated spin currents can be generated in heterostructures composed of ferromagnetic(FM) insulators and metals [88, 89]. A more exotic method of transporting spin harnesses the ground states of both easy-plane FMs [90–92] and antiferromagnetic insulators (AFMIs) [93]. It has been long appreciated that magnetically ordered systems with spontaneously broken $U(1)$ symmetry [94, 95] support metastable spin spiral

states that can transfer spin angular momentum without dissipation [1]. In this regard, heterostructures composed of AFMIs are advantageous to those composed of easy-plane FMs, since they are less sensitive to stray fields or dipolar interactions, which can destroy dissipationless spin transport in easy-plane FMs [96].

It is difficult to experimentally distinguish between spin super-currents and magnon mediated spin currents in magnetic insulators, since the spin wave decay length is long due to the small Gilbert damping. Therefore, other signatures of spin superfluidity in magnetically ordered systems need to be explored. To this end, it is advantageous to investigate the connections between superconductivity and magnetism further. One remarkable phenomena is the Josephson effect [97], which occurs in coupled superfluids and superconductors because the coupling energy is a periodic function of the relative phase difference. A similar energy dependence can be anticipated for exchange coupled AFMIs and easy-plane FMs. This insight suggests that it is instructive to analyze the effect of exchange coupling on the spin currents in heterostructures composed of exchange coupled AFMIs and easy-plane FMs. Josephson dynamics were also predictied in dipole coupled nanomagnets [98].

In this chapter, we propose a lateral spin valve heterostructure, which consists of two AFMIs separated by a thin metallic spacer [2]. We show that the spin superfluid analogy can be further extended to realize Josephson-like oscillations of the spin currents flowing through exchange coupled antiferromagnetic insulators (AFMIs). This oscillatory spin current can be detected by injecting a pure spin current on the left side of the heterostructure illustrated in Fig. 6.1. A spin chemical potential established perpen-

[1] Spin supercurrents are analogues of charge or mass supercurrents in superconductors and superfluids. This analogy is useful even in the absence of strict conservation laws for spin, as long as the violation of the conservation laws is weak

[2] The same phenomena should be anticipated in similar heterostructures composed of easy-plane FMs

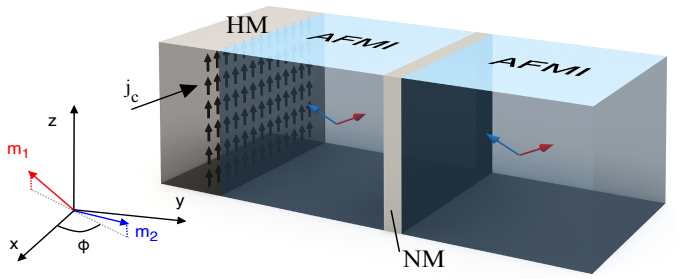

Figure 5.1: Schematic diagram of the proposed heterostructure to detect the Josephson effect in spin superfluids. The heterostructure consists of two antiferromagnetic insulators (AFMIs) separated by a thin non-magnetic metallic (NM) spacer. The magnetization of the AFMIs lies in the xy-plane as indicated in the inset showing the direction of the Néel vector and phase ϕ, with a spin canting in the $\hat{z}$-direction. A spin chemical potential of up spins on the left interface of the AFMI can drive an oscillating spin current through the metallic spacer via spin pumping. The spin Hall effect in a heavy metal (HM) can inject a spin current. The spin current flowing through a spin-orbit (SO) coupled metallic spacer can be detected via the inverse spin Hall effect.

dicular to the direction of the Néel vector field, drives an oscillatory spin supercurrent which can be converted to a charge current via the inverse spin Hall effect through a metallic spacer with large spin-orbit coupling. Furthermore, this oscillatory spin current induces a non-Ohmic I_S-V_S characteristics of AFMI exchange coupled heterostructures, which provides a "smoking gun" signature of the spin superfluidity.

5.2 Coupled magnetization dynamics

Consider the heterostructure in Fig. 6.1, consisting of two bipartite lattice AFMIs separated by a thin nonmagnetic metallic spacer that provides a local interlayer exchange coupling between the two AFMIs. Each AFMI has a staggered spin orientation $\mathbf{s}_i(\mathbf{r}) = S_i(\mathbf{r})/S$ where $i = \pm$ denotes the left (right) AFMI and S is the saturated spin density. The long-wavelength effective Hamiltonian describing the fluctuation of the AFMIs can be expressed in terms of two continuum fields $\mathbf{n}_i(\mathbf{r})$ (the Néel vector field) and $\mathbf{m}_i(\mathbf{r})$ (the canting field), with the local spin orientation $\mathbf{s}_i(\mathbf{r}) = \eta_{i,\mathbf{r}}\mathbf{n}_i(\mathbf{r})\sqrt{1-|\mathbf{m}_i(\mathbf{r})|^2}+$

$\mathbf{m}_i(\mathbf{r})$ with the constraints $|\mathbf{n}_i| = 1$ and $\mathbf{n}_i \cdot \mathbf{m}_i = 0$, where $\eta_{i,\mathbf{r}} = \pm 1$ for the $A(B)$ sublattices [99]. Assuming that the Néel vectors lie in the xy-plane with an interlayer exchange interaction $\sum_{\mathbf{r},\mathbf{r}'} J_{\mathbf{r},\mathbf{r}'} \mathbf{s}_{L,\mathbf{r}} \cdot \mathbf{s}_{R,\mathbf{r}'}$ [100], the effective Hamiltonian capturing the long-wavelength dynamics of this system is,

$$\begin{aligned} \mathcal{H} &= \frac{1}{\mathcal{V}} \int d\mathbf{r} \sum_{i=\pm 1} \left[\frac{\rho}{2} \big(\nabla \mathbf{n}_i(\mathbf{r})\big)^2 + \frac{\lambda}{2} \mathbf{m}_i^2(\mathbf{r}) \right. \\ &+ \left. \frac{J}{2} \mathbf{n}_i(\mathbf{r}) \cdot \mathbf{n}_{-i}(\mathbf{r}) + \frac{J}{2} \mathbf{m}_i(\mathbf{r}) \cdot \mathbf{m}_{-i}(\mathbf{r}) \right], \end{aligned} \tag{5.1}$$

where $\mathcal{V}$ is the volume, J is the inter-layer exchange coupling of the two AFMIs, $\lambda > 0$ is the homogenous AFMI exchange coupling, and ρ is the spin stiffness assumed equal for both AFMIs [101]. The energy of each AFMI is independent of the direction of the Néel vector $\mathbf{n}_i$ indicating $U(1)$ symmetry, and $\lambda > 0$ ensures that $\mathbf{m}_i = 0$ in equilibrium.

The long wavelength dynamics of the isolated system can be captured by the Landau-Lifshitz-Gilbert(LLG) equations, which subjected to the AFMI constraints, can be expressed as,

$$\hbar \dot{\mathbf{n}}_i = \lambda \mathbf{m}_i \times \mathbf{n}_i + J \mathbf{m}_{-i} \times \mathbf{n}_i - \hbar \alpha \mathbf{n}_i \times \dot{\mathbf{m}}_i, \tag{5.2}$$

$$\hbar \dot{\mathbf{m}}_i = \rho \mathbf{n}_i \times \nabla^2 \mathbf{n}_i + J \mathbf{n}_i \times \mathbf{n}_{-i} - \hbar \alpha \mathbf{n}_i \times \dot{\mathbf{n}}_i, \tag{5.3}$$

where $(\dot{\mathbf{m}}_i, \dot{\mathbf{n}}_i)$ denote the time derivatives of the fields $(\mathbf{m}_i, \mathbf{n}_i)$, α is the damping constant assumed the same for both AFMIs, and henceforth we neglect the spatial dependence of the fields ($\nabla^2 \mathbf{n}_i \sim 0$). To implement the AFM constraints in the above equation we define: $\mathbf{n}_i = (\cos\theta_i \cos\phi_i, \cos\theta_i \sin\phi_i, \sin\theta_i)$, where ϕ is the azimuthal angle, θ is the relative angle to the xy-plane and $\mathbf{m}_i = (-m_{\theta,i} \sin\theta_i \cos\phi_i - m_{\phi,i} \sin\phi_i, -m_{\theta,i} \sin\theta_i \sin\phi_i + m_{\phi,i} \cos\phi_i, m_{\theta,i} \cos\theta_i)$. With these substitutions the long-wavelength dynamics of the coupled AFMIs can be described in terms of a pair of canonically conjugate fields $(m_{\theta,i}, \phi_i)$ and $(m_{\phi,i}, \theta_i)$ for both AFMIs. For small varia-

tions about the Néel ordered state $\theta_i \approx 0$, the LLG equations for $(m_{\theta,i}, \phi_i)$ neglecting the quadratic terms, are decoupled from the $(m_{\phi,i}, \theta_i)$ fields, reducing to,

$$\hbar \dot{m}_{\theta,i} = J \sin(\phi_i - \phi_{-i}) - \hbar\alpha\dot{\phi}_i,$$
$$\hbar \dot{\phi}_i = \lambda m_{\theta,i} + J m_{\theta,-i} + \hbar\alpha \dot{m}_{\theta,i}. \tag{5.4}$$

For zero damping ($\alpha = 0$), the above equations describing the magnetization dynamics for exchange coupled systems of AFMIs are remarkably similar to the Josephson equations of coupled superconductors. This becomes evident after defining the relative magnetization $m_\theta = m_{\theta,L} - m_{\theta,R}$ and the relative phase $\phi = \phi_L - \phi_R$. Then, Eqs. (6.3) give

$$\hbar \dot{m}_\theta = 2J \sin(\phi); \quad \hbar\dot{\phi} = (\lambda - J) m_\theta. \tag{5.5}$$

The time dynamics of the relative phase is governed by $\ddot{\phi} = \omega_0^2 \sin(\phi)$, where the characteristic frequency $\omega_0 = \sqrt{2J(\lambda - J)}/\hbar$, depends on the nature of the inter-layer exchange of the coupled AFMIs. The equation describing the phase dynamics resembles the equation of a simple pendulum with tilt angle ϕ or equivalently the motion of a particle with unit mass moving in a potential $U(\phi) = \omega_0^2 \cos(\phi)$. This mechanical analogue provides an intuitive understanding of the rich magnetization dynamics of Eqs. (6.3).

Starting with initial conditions $\phi(t = 0) = 0$ and $m_{\theta,0} = 0.05 \propto \dot{\phi}(t = 0)$, we solve Eqs. (6.3) for both FM and AFM interlayer exchange coupling J. The magnetization exhibits periodic oscillations with frequencies $\omega \sim 1 - 10$ THz, as indicted in Fig. 5.2, with different dynamics for the FM and AFM inter-layer exchange. Fig. 5.2(a) shows the periodic variation of the phase dynamics for an FM exchange $|J|/\lambda = 1/300$ with $\lambda = 30meV$, which oscillates about the equilibrium point $\phi = 0$. The magnitude of the oscillations depends on the initial velocity $\dot{\phi}_0 \propto (\lambda - J) m_{\theta,0}/\hbar$. The individual

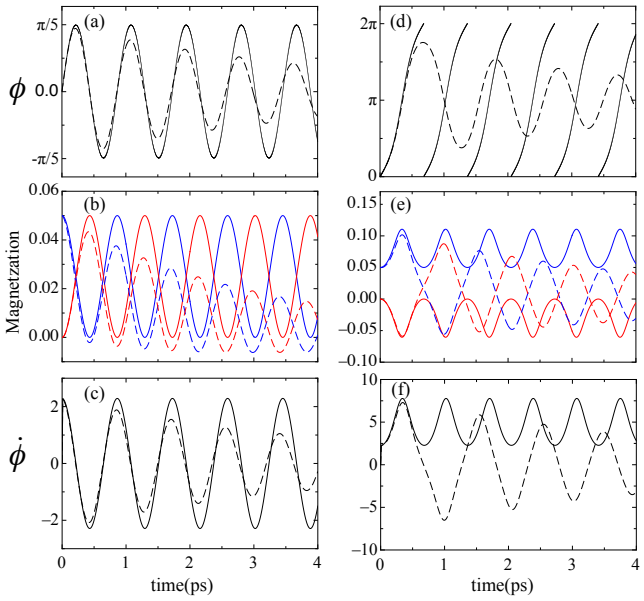

Figure 5.2: Dynamics of m_L (blue), m_R (red), ϕ, and the total spin current $I_S/I_{S,0} = \dot{\phi}$ with the initial conditions $m_0 = 0.05$ and $\phi = 0$. (a)-(c) are for the case of a FM inter-layer exchange $J < 0$, and (d)-(f) represent the case for an AFMI inter-layer exchange $J > 0$. All dashed lines represent the dynamics for non-zero damping with $\alpha = 0.05$. The equations are solved for $|J|/\lambda = 1/300$ and $\lambda = 30$ meV.

magnetizations ($m_{\theta,L}$ and $m_{\theta,R}$) also exhibits coupled periodic oscillations and as indicated in Fig 5.2 (b), and the total magnetization is conserved for the isolated system in the absence of any damping. When the initial magnetization is above a critical value $m > m_{0,c} = 2\sqrt{2|J|/(\lambda - J)}$, the Néel vector performs full rotations in the xy-plane, this critical value corresponds to an initial angular velocity of the pendulum $\dot{\phi}_c \geq 2|\omega_0|$. The effect of the Gilbert damping with $\alpha = 0.05$ denoted by the dotted lines in Fig. 5.2, results in an exponential damping of the phase in time, which in turn, leads to an exponential damping of the total magnetization.

The mechanical analogue for the antiferromagnetic interlayer exchange coupling $J > 0$ corresponds to a simple pendulum with the initial condition $\phi(t = 0) = \pi$, or the π-phase Josephson junction in superconductors. For this case, as shown in Fig. 5.2(d), irrespective of the initial conditions, the Néel vector performs complete

rotations in the xy-plane. $m_{\theta,L}$ and $m_{\theta,R}$ oscillate in-phase leading to an oscillation in m_θ which is conserved in the absence of damping. With damping, ($\alpha = 0.05$), the individual magnetizations decay exponentially as indicated by the dashed lines in Fig. 5.2, and as before the total magnetization decays exponentially.

5.3 Spin-current Dynamics

5.3.1 Oscillatory spin-current

The oscillations in the relative magnetization induced by the dynamics in the Néel vector fields of the AFMIs pump a spin current through the metal spacer. This spin current can be written as $I_S = I_{S,L} - I_{S,R}$, where

$$I_{S,i} = \hbar\frac{G_r}{4\pi}(\mathbf{n}_i \times \dot{\mathbf{n}}_i + \mathbf{m}_i \times \dot{\mathbf{m}}_i) - \hbar\frac{G_{im}}{4\pi}(\dot{\mathbf{m}}_i), \tag{5.6}$$

with $i = L(R)$ and $I_{S,L}(I_{S,R})$ is the spin current injected from the left (right) side of the metallic spacer, $G = \mathcal{A}g^{\uparrow\downarrow}/NS$ is the spin-mixing conductance at the AFMI/spacer interface, $\mathcal{A}$ is the interface area, $g^{\uparrow\downarrow} = g_r^{\uparrow\downarrow} + ig_{im}^{\uparrow\downarrow}$ is the spin-mixing conductance per unit area [102, 103], and $N = \mathcal{V}/a_0^3$ denotes the total number of spins. Restricting to the $\hat{z}$-component of the spin, the spin current pumped into the metallic spacer by the AFMIs can be expressed as,

$$I_S = \hbar\frac{G_r}{4\pi}\dot{\phi_L} - \hbar\frac{G_r}{4\pi}\dot{\phi_R} = \hbar\frac{G_r}{4\pi}\dot{\phi}, \tag{5.7}$$

valid for $|m_i| \ll |n_i|$. For simplicity, we assume the spin-mixing conductance is real and equal at both AFMI-spacer interfaces.

The normalized $I_S/I_{S,0}$ spin current flowing through metallic spacer, where $I_{S,0} = \hbar G\omega_0/(4\pi)$ is the characteristic spin current supported by the junction, is plotted in Figs. 5.2(c) and (f) for the FM and the AFM inter-layer exchange. Eq. 5.7 states

that the spin current is proportional to the rate of change of the relative phase, different from the Josephson voltage phase relation in a superconductor. Similarly, we anticipate that the spin chemical potential must act, via spin transfer torque, as a source term for the rate of change of the relative magnetization.

5.3.2 Steady state spin-current

Non-equilibrium spin accumulation at the left interface of the first AFMI, via the spin hall effect [104] or anomalous Hall effect, can transfer angular momentum by inducing a spin transfer torque on the coupled AFMI system. The spin-transfer torque can be expressed as

$$\tau_S = \frac{G_r}{4\pi}\mathbf{n} \times \boldsymbol{\mu_S} \times \mathbf{n} + \frac{G_{im}}{4\pi}\boldsymbol{\mu_S} \times \mathbf{n}, \tag{5.8}$$

where $\boldsymbol{\mu_S} = \boldsymbol{\mu_0} - \hbar\mathbf{n} \times \dot{\mathbf{n}}$ denotes the total non-equilibrium spin accumulation at the left interface, $\boldsymbol{\mu_0}$ is the spin accumulation, and $\hbar\mathbf{n} \times \dot{\mathbf{n}}$ denotes the spin pumping back-action due to the precession of the Néel vector, satisfying Onsager reciprocity [93]. This non-equilibrium spin accumulation leads to a non-zero relative magnetization via spin-transfer torque, resulting in the precession of the Néel vector field that drives an oscillatory spin current through the metallic spacer, which we analyze next.

Consider the spin transfer effect in the $\hat{z}$ spin direction at the left interface and drop G_i. In the presence of a spin accumulation at the left interface, Eq. (5.3) acquires a spin transfer torque τ_S resulting in modified equations for the canonically conjugate fields $(m_{\theta,i}, \phi_i)$. Eliminating m_θ from the modified equations, the time dynamics of the phase ϕ satisfy,

$$(1+\alpha^2)\ddot{\phi} + \frac{\hbar\tilde{\alpha}\omega^2}{2J}\dot{\phi} - \omega^2\sin(\phi) = \frac{\omega^2}{2J}V_S, \tag{5.9}$$

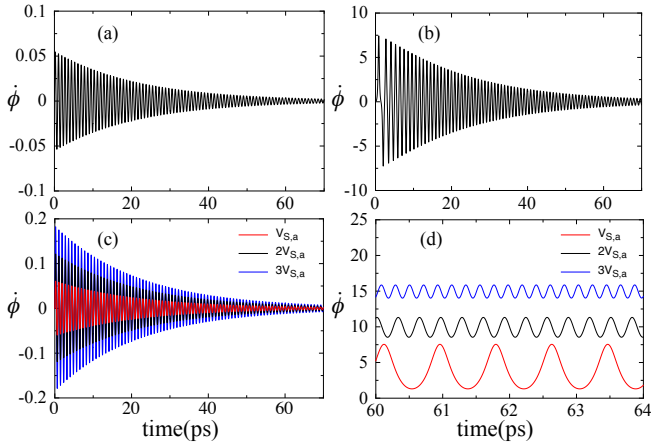

Figure 5.3: Steady state solution of $\dot{\phi}$ for the FM inter-layer exchange ($J < 0$) (a, c), and AFM interlayer exchange ($J > 0$) (b, d) as a function of the spin voltage V_S. We choose a spin injection value $V_{S,a} = 0.031J$ that is greater than the critical spin injection. $V_S < V_{S,0}$ for (a) and (b), and $V_{S,a} > V_{S,0}$ for (c) and (d). As before, we set $\lambda = 30meV$, $|J|/\lambda = 1/300$ and $\alpha = 0.001$.

Where $V_S = G_r^L \mu_0/(4\pi)$, $\tilde{\alpha} = \alpha + \alpha'$ with $\alpha' = G_r/(4\pi)$ is the enhanced damping due to the spin pumping at the spacer, and we define a critical spin voltage $V_{S,c} = 2J$. Here we assume α' is small compared to α and take $\alpha\tilde{\alpha} \sim \alpha^2$. This equation has been extensively studied in the context of superconductivity, and describes the RCSJ model for superconducting Josephson junctions [105]. Based on this similarity, it is prudent to define an effective Stewart-McCumber parameter $\beta = 2J(1+\alpha^2)/(\alpha^2(\lambda - J))$, which determines over-damped ($\beta \ll 1$) or under-damped ($\beta \gg 1$) junctions. For typical values of damping in AFMIs $\beta \sim 2J/(\lambda\alpha^2) \gg 1$, which corresponds to an under-damped junction where Eq. (5.9) must be solved numerically.

Eq. (5.9) resembles the equation of motion of a particle of mass $\hbar^2(1+\alpha^2)/(2(\lambda - J))$ moving along the ϕ axis in the presence of an effective tilted washboard potential $U(\phi) = 2J\cos(\phi) - V_S\phi$ with a viscous drag force $\hbar\tilde{\alpha}\dot{\phi}$. The phase dynamics $\dot{\phi}$ in the presence of damping $\alpha = 0.001$ are plotted in Fig. 5.3 for various values of a constant spin chemical potential V_S. The steady state solution of $\dot{\phi}$ for both the FM or

the AFM inter-layer exchange interaction shows the same behavior when $V_S < V_{S,0}$ (see Fig. 5.3(a) & (b)) and different dynamics when $V_S > V_{S,0}$ (see Fig. 5.3(c) & (d)), where $V_{S,0} = 0.031J \ll V_{S,c}$ depends on β. When the spin chemical potential is small $V_S < V_{S,0}$, viscous drag dominates the dynamics, and the oscillations in the phase decay as a result of the damping for both the FM and AFM inter-layer exchange interaction. However, if the spin transfer torque induced by V_S is sufficiently large, the energy gain due to the spin transfer torque can balance the energy loss due to the damping resulting in a continual rotation of the Néel vector. In the language of spintronics, this results from the anti-damping like torque due to V_S fully compensating the damping torque. For $J > 0$, which corresponds to the superconducting π-junction, the system is at an unstable equilibrium point, therefore, a small driving force ($V_S \ll 2J$) is enough to induce a full 2π-rotation of the phase. However, for $J < 0$, the system is at an energy minima, so a large driving force $V_S \sim 2J$ is required to overcome both the viscous damping force and the force required to push the particle over the hill.

In the over-damped case $\beta \ll 1$, when $V_S < V_{S,c}$ a static solution for the phase is allowed $\phi = \sin^{-1}(V/(2J))$ implying $I_S = 0$. However, when $V_S > V_{S,c}$ only time dependent solutions exist, for $\beta \ll 1$ we can assume $\langle\ddot{\phi}\rangle \sim 0$, solving Eq. 5.9 gives an oscillation frequency $\omega = 1/(h\tilde{\alpha})\sqrt{V^2 - 4J^2}$ for the phase ϕ, independent of the sign of the inter-layer exchange interaction. Similar characteristic behavior appears for the case of intermediate damping $\beta \sim 1$, however the critical value of $V_{S,0} = 2\alpha\sqrt{2|J|\lambda}$ to induce a non-zero steady state $\dot{\phi}$, depends on the damping.

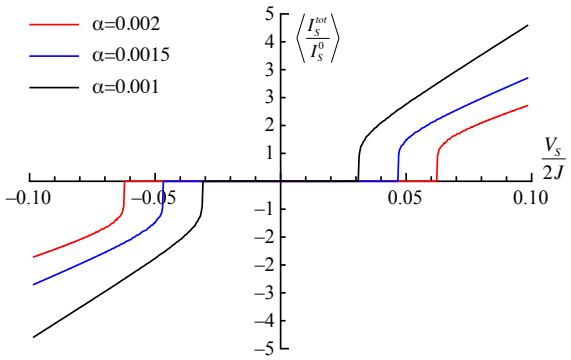

Figure 5.4: $I_S - V_S$ characteristics as a function of the applied spin voltage V_S for different values of the damping constant with $\lambda = 30$ meV and $|J|/\lambda = 1/300$.

5.4 I_S-V_S characteristics

The phase dynamics associated with both the FM and AFM inter-layer exchange interactions result in non-Ohmic I_S-V_S characteristics for the AFMI Josephson junctions. The time averaged value for the spin current $I_{S,av}$ can be determined from Eq. (5.7) for over-damped and under-damped junctions. For over-damped AFMI Josephson junctions $\beta \ll 1$, the $I_S - V_S$ characteristics can be inferred from $I_{S,av} = \hbar G\omega/(4\pi)$ giving the simple relation,

$$I_{S,av} = \frac{G}{4\pi\tilde{\alpha}}\sqrt{V_S^2 - 4J^2} \tag{5.10}$$

for $V_S > 2J$, which interpolates smoothly between $I_{S,av} = 0$ and Ohmic behavior with an effective spin resistance $R_S = 4\pi\tilde{\alpha}/G$. The $I_S - V_S$ characteristics for the under-damped junction $\beta \gg 1$ with an AFM inter-layer exchange ($J > 0$) are plotted as function of the spin chemical potential V_S for different values of the damping in Fig. 5.4. In the under-damped case, the spin current jumps discontinuously from $I_S = 0$ until the spin chemical potential reaches $V_{S,0}$, and $V_{S,0}$ is proportional to β. For under-damped junctions with a FM inter-layer exchange ($J < 0$) $I_{S,av} = 0$ for $V_{S,0} \sim 2J$ where the approximation $|\mathbf{m}| \ll |\mathbf{n}|$ breaks down and requires solutions of LLG equations without

any approximations. The $I_S - V_S$ characteristics of AFMI spin Josephson junctions are different from the $I - V$ characteristics of Josephson junctions in superconductors. These differences originate from the spin-current phase relation (see Eq. 5.7) and the role of the spin transfer torque in exchange coupled AFMIs.

5.5 Discussion and Summary

This average spin current flowing between the AFMIs can be detected via the inverse spin Hall effect if the metallic spacer has large spin-orbit coupling [88,104]. There are several ways to induce a spin chemical potential [92, 93, 96]. Here we consider spin injection by the spin Hall efect. To estimate current densities required to drive a spin current, consider two $0.1\mu\text{m} \times 0.1\mu\text{m} \times 0.01\mu\text{m}$ NiO thin films, with the exchange energy $\lambda = 19.01\text{meV}$ [106]. Taking $\alpha = 0.007$ and $J = 0.1$ meV we find that a spin chemical potential $V_{S,0} = 0.039$ meV is required for a spin current $I_S = 2.2 \times 10^{-2}$ meV. The critical current density can be estimated from the relation $V_S = \hbar G/(4\pi e)\theta_{SH} I_c$. Taking the spin mixing conductance g_r of NiO of $6.9 \times 10^{18}\text{m}^{-2}$ [102], and assuming a 10nm thick Pt spin current injector with $\theta_{SH} \sim 0.1$, we obtain an injection current density $I_c \sim 2.3 \times 10^7 \text{A/cm}^2$. The induced charge current, $I_c = 2e\theta_{SH} I_S/\hbar$ through a thin film Pt spacer with $t = 1$ nm and conductivity $\sim 0.095\ (\mu\Omega\text{cm})^{-1}$ gives an induced non-local voltage $V \sim 0.017\mu V$ across the Pt spacer.

The RKKY interaction is one mechanism that can generate the interlayer exchange coupling between the two AFMIs [107]. In this case, the interlayer exchange coupling will be an oscillatory function of $k_F d$ where k_F is the Fermi wavevector and d is the thickness of the non-magnetic metallic spacer. The detailed interlayer exchange coupling for AFMI multilayers will depend on the local spin orientation at the

AFMI/non-magnetic metal interface. Exchange coupling between AFMIs has not yet been studied, and it is an important research direction in the emerging field of AFM spintronics.

Similar oscillations in the spin current can occur across exchange coupled easy-plane FMs due to their broken U(1) symmetry. The out-of-plane anisotropy in FMs will play the role of λ in AFMIs and determine the property of the junction. Even in the presence of in-plane anisotropy, we expect these oscillations to persist as long as the spin chemical potential is above the anisotropy energy scale. The higher order LLG terms do not destroy the spin current oscillations, but they do affect their detailed dynamics. Lastly, the spatial variation in the order parameter, neglected here, can nucleate spin solitons or instantons within the junction, which can lead to a Fraunhofer-like interference patterns in the non-local voltage similar to the behavior of critical super-currents in superconducting Josephson junctions.

In summary, we propose a novel effect in exchange coupled AFMIs that is the analogue of the Josephson effect in superfluids. Due to periodic dependence of the exchange energy on the relative phase difference, an oscillatory spin current flows through the metallic spacer that is proportional to the rate of change of the relative in-plane orientation of the Néel vector fields. A spin transfer torque induced by a spin chemical potential at one of the interfaces results in non-linear I_S-V_S characteristics that distinguish the proposed lateral spin valve heterostructure composed of AFMIs and provide a signature of spin superfluidity. Furthermore, this heterostructure is an example of a pure spin AFMI terahertz oscillator [108].

Chapter 6

Spin superfluid Josephson oscillator

6.1 Introduction

When a spin polarized currents passes through a ferromagnetic conductor, it can exert torque on the magnetic moments [11, 12] by transferring spin angular momentum. This spin transfer torque (STT) can be used to electrically manipulate the magnetization. One of the major achievements of STT inspired technologies are spin torque oscillators. Spin oscillators utilize this effect to convert dc electric current into non-linear magnetization precession [109–114]. Persistent magnetization oscillations can also be induced in device heterostructures of magnetic insulators and metals with large spin-orbit coupling. In these systems a pure spin current, injected via the spin Hall effect [115, 116] by driving electrical currents in the heavy metal (HM), causes magnetization dynamics in the insulating ferromagnets.

One of the goals of spintronics is to transport spin with minimal losses. Spin superfluid (SSF) transport can be achieved in easy-plane FMs and antiferromagnets

(AFMs) [93, 117–120], by creating a non-equilibrium meta-stable state with static spin spiral textures. This state carries a spin current which decays algebraically over the propagation length has an advantage over magnon mediated spin currents [93, 117]. Recently some of us, proposed a spin Josephson-type oscillation associated with a 2π in-plane oscillation of the Néel vector in exchange coupled AFMs [2]. This is the magnetic analogue of the Josephson effect in superfluids. In this chapter, we demonstrate that an easy-plane FM spin superfluid Josephson (SSJ) junction sandwiched by two heavy metal (HM) contacts can serve as a spin oscillator.

The SSJ oscillator, illustrated in Fig. 6.1, consists of two easy-plane ferromagnets (FMs) with an anti-ferromagnetic inter-layer exchange coupling. This is the magnetic analogue of a π-phase Josephson junction. Electrical current along the x-direction in the HM can be used to generate a transverse spin current across the junction. Using both the Landau-Lifshitz-Gilbert (LLG) equations and micromagnetic simulations, we show that this current drives steady-state spin oscillations within the junction with a frequency determined by the applied current, damping and the parameters of the easy-plane FMs. These spin oscillations result from 2π rotation of the relative in-plane magnetization direction in the easy-axis FMs. The SSJ effect produces a novel magneto-resistance (MR) effect, here after called SSJ-MR, which is the only contribution in insulating devices. Whereas in metallic systems, the MR signal induced by the 2π phase rotation gets additional contributions from the giant magneto-resistance (GMR) and the anisotropic magneto-resistance (AMR).

When connected with an ac current, the time-averaged SSJ-MR exhibits Shapiro steps as a function of the applied current's dc component. SSJ-MR exhibits a step when the ac driving frequency matches the characteristic frequency of the SSJ oscillator. Fur-

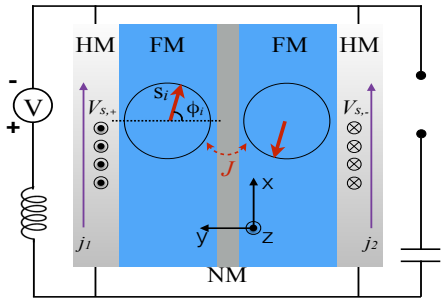

Figure 6.1: Schematic diagram of the proposed hetero-structure. Two easy-plane ferromagnets (FMs), with magnetization in the x-y plane) are separated by a thin non-magnetic metallic(NM) spacer. The ferromagnets are exchange coupled via an anti-ferromagnetic type inter-layer exchange coupling J. The ferromagnetic junction is sandwiched by two identical heavy metals.

thermore, the large precession angle of the in-plane magnetization results in large output power of SSJ oscillators.

6.2 Theoretical Model

The schematic diagram of the SSJ oscillator is shown in Fig. 6.1. The device heterostructure consists of two HM contacts and two easy-plane FMs separated by a thin non-magnetic spacer. The Hamiltonian for this system can be expressed as,

$$\begin{aligned} \mathcal{H} &= \frac{1}{\mathcal{V}} \int d\mathbf{r} \sum_{i=\pm} \frac{1}{2} [A\big(\nabla \mathbf{s}_i(\mathbf{r})\big)^2 + K s_i^z(\mathbf{r})^2 \\ &+ J\mathbf{s}_i(\mathbf{r}) \cdot \mathbf{s}_{-i}(\mathbf{r})], \end{aligned} \tag{6.1}$$

where $\mathcal{V}$ is the volume, J is the interlayer exchange coupling between the two easy-plane FMs, A and K represent the spin stiffness and easy-plane anisotropy of the FM, respectively. $\mathbf{s}_i(\mathbf{r}) = S_i(\mathbf{r})/S$ denotes the spin orientation of each easy-plane FM, $i = \pm$ denotes the top (bottom) FM and S is the saturated spin density. For simplicity, we assume all materials, the HMs, the easy-plane FMs and their interfaces are identical. In Eq. 6.1 the easy-plane anisotropy ($K > 0$) ensures the energy of each FM is independent

of the in-plane magnetization direction (indicating $U(1)$ symmetry). The energy is minimized by the in-plane spin configuration, $s_i^z = 0$ with a fixed in-plane magnetization.

For the in-plane spin configuration, the last term in Eq. 6.1 becomes an oscillatory function of the relative phase of the in-plane magnetization. The interlayer exchange coupling J can be AFM ($J > 0$) or FM ($J < 0$). This depends on the material and geometrical parameters [121]. Dipolar interactions in easy plane FMs can break the easy-plane U(1) symmetry which destroys spin superfluidity [122] and spin Josephson effect. In order to minimize the effects of dipolar interactions we work with an AFM type inter-layer exchange coupling and assume $J > 0$ hereafter. For $J > 0$ spins in the top and bottom easy-plane FMs point in the opposite directions which cancels the dipolar interactions.

The long wavelength magnetization dynamics of the device heterostructure can be captured by the Landau-Lifshitz-Gilbert (LLG) equation,

$$\begin{aligned} \hbar\dot{\mathbf{s}}_i = \quad & -\mathbf{s}_i \times (A\nabla^2\mathbf{s}_i + K(s_i^z\hat{\mathbf{z}}) + J\mathbf{s}_{-i}) \\ & +\alpha\mathbf{s}_i \times \dot{\mathbf{s}}_i + \boldsymbol{\tau}_{s,i}, \end{aligned} \tag{6.2}$$

where $\dot{\mathbf{s}}_i$ denotes the time derivative of $\mathbf{s}_i$, α is the damping constant and $\boldsymbol{\tau}_{s,i}$ describes the spin torque and spin pumping effect at the HM/FM interfaces. To induce the spin oscillations, a spin current with polarization perpendicular to the easy-plane, can be used to produce a spin transfer torque on the in-plane magnetization. This spin current is generated by driving an electrical current in x-direction in the HM contacts via the spin Hall effect. Decomposing, $\mathbf{s}_i = (\sqrt{1-(s_i^z)^2}\cos\phi_i, \sqrt{1-(s_i^z)^2}\sin\phi_i, s_i^z)$, the dynamics of both FMs can be expressed in terms of canonically conjugate amplitude and phase variables, s_i^z and ϕ_i. For small variation of the out-of-plane magnetization, $s_i^z \ll 1$, and $\tau_{s,i}$ is perpendicular to the easy plane, the LLG equation can be expanded to the lowest

order of s_i^z and ϕ_i. Since we are interested in the magnetization dynamics across the junction, hereafter we neglect the spatial dependence of the fields and set $\nabla^2 \mathbf{s}_i = 0$.

$$\begin{aligned} \hbar \dot{s}_i^z &= J \sin(\phi_i - \phi_{-i}) - \hbar\alpha\dot{\phi}_i + \tau_{i,s}^z, \\ \hbar \dot{\phi}_i &= K s_i^z + J s_{-i}^z + \hbar\alpha \dot{s}_i^z, \end{aligned} \tag{6.3}$$

Defining $\phi = \phi_i - \phi_{-i}$ as the relative phase, $\tau_s^z = \tau_{s,i}^z - \tau_{s,-i}^z$ as the total spin torque across the junction and $n = s_i^z - s_{-i}^z$ as the relative out-of-plane magnetization, the equation of motion can be reduced into two equations that describe the dynamics of the relative coupled variables,

$$\begin{aligned} \hbar \dot{n} &= 2J \sin(\phi) - \hbar\alpha\dot{\phi} + \tau_s^z, \\ \hbar \dot{\phi} &= (K - J)n + \hbar\alpha \dot{n}. \end{aligned} \tag{6.4}$$

For zero damping and zero spin torque ($\alpha = 0, \tau_s^z = 0$), the above equations resemble the π-phase Josephson junction of weak link superconductors with characteristic frequency $\omega_0 = \sqrt{2J(\lambda - J)}/\hbar$.

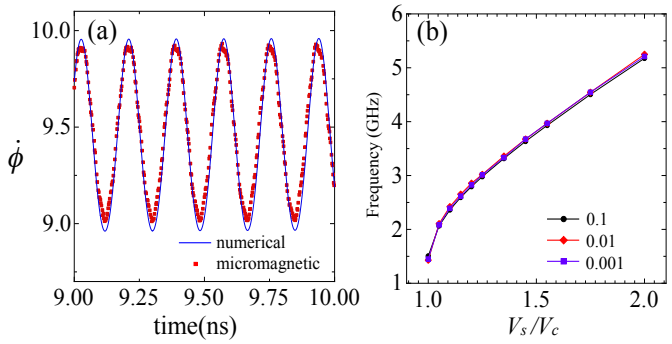

Figure 6.2: (a) The steady state time dynamics of $\dot{\phi}_n$ from both numerical and micromagnetic simulations. (b) Frequency as a function of the spin chemical potential for three different dampings in the underdamped regime.

6.3 Dynamics with dc input

When connected with an external electric field as shown in Fig. 6.1, the two HMs are connected in a parallel circuit configuration with currents flowing in the same direction (x-direction). The current flowing through the HM contacts generates a spin chemical potential, with spins perpendicular to the easy plane. To determine the electric and magnetic dynamics in the circuit, we solve for their dynamics self-consistently in the device heterostructure. The spin torque at the HM/FM interface can be expressed as,

$$\boldsymbol{\tau}_{s,i} = \frac{g_s}{4\pi}[\mathbf{s}_i \times (\boldsymbol{\mu}_{0,i} \times \mathbf{s}_i) - \hbar \mathbf{s}_i \times \dot{\mathbf{s}}_i]. \tag{6.5}$$

where $\boldsymbol{\mu_{0,i}} = \mu\hat{z}$, denotes the non-equilibrium spin accumulation at the top and bottom interface and g_s is effective spin mixing conductance, which we assume to be purely real through out this paper. The first term in Eq. 6.5 is the spin torque exerted due to the injected spin current. The second term is the reciprocal spin pumping effect [103] due to the precession of the magnetization in the FMs. This term must be included to satisfy Onsager's reciprocity relations.

With the circuit set up above, we have $V_{s,i} = -V_{s,-i} = |V_s|/2$, where the spin chemical potential $V_s = g_s\mu/(4\pi)$. Inserting this relationship into Eq. 6.3 and eliminating n we get the equation of motion for ϕ [2],

$$(1 + \tilde{\alpha}\alpha)\ddot{\phi} + \frac{\hbar\tilde{\alpha}{\omega_0}^2}{2J}\dot{\phi} - {\omega_0}^2 \sin(\phi) = \frac{{\omega_0}^2}{J}V_s, \tag{6.6}$$

where $\tilde{\alpha} = \alpha + g_s/(4\pi)$ is the enhanced damping. This equation represents an effective RCSJ model for the junction with an effective Stewart-McCumber parameter $\beta = 2J(1+\alpha\tilde{\alpha})/(\tilde{\alpha}^2(K-J))$ [123, 124]. Because of the Gilbert damping a critical spin chemical potential V_c, which is related to the current density in the HM contacts, is required to excite a magnetization oscillation. In the strong damping case ($\beta \ll 1$), the critical

spin chemical potential required to induce a persistent $\dot{\phi}$ oscillation is $V_c = 2J$. In the intermediate damping regime($\beta \sim 1$), the critical spin chemical potential can be estimated as $V_c = 2\tilde{\alpha}\sqrt{2JK}$, which depends on the damping, the interlayer exchange coupling and the FM easy-plane.

To determine the magnetization dynamics, we perform both micromagnetic simulations (blue dots in Fig 6.2 (b)) and numerical calculations of the RCSJ model (solid line in Fig 6.2 (b)) for the SSJ. For both calculations, in the steady-state dynamics, $\dot{\phi}$ oscillates around a finite time-averaged value, these oscillations correspond to 2π rotation of the relative in-plane magnetization. The micromagnetic simulations were performed on two easy-plane FM SSJ with dimensions 200 nm $\times$ 200 nm $\times$ 5 nm. The saturation magnetization in micromagnetic simulations is $M_s = 140$kA/m and the parameters for Eq. 6.1 are $K = 2.5$ meV, $J = 1$ μeV with a damping constant $\alpha = 0.01$. The Hamiltonian does not include magnetic dipolar interactions, which are irrelevant for an AFM-type inter-layer exchange coupling ($J > 0$) . Comparison of the micromagnetic simulations validates our Hamiltonian and the RCSJ model.

Above the critical voltage V_c the oscillation frequency depends on the applied voltage V_s. To investigate the relationship, we plot the oscillation frequency as a function of the normalized spin chemical potential $V = V_s/V_c$ for three different damping constants in Fig. 6.2. Within this damping regime, the frequency has a quasi linear relationship with V which is independent of damping. In the strong damping regime($\beta \ll 1$), one can analytically solve Eq. 6.6 and obtain a time-dependent solution for $\dot{\phi}$ with an oscillation frequency $\omega = \sqrt{{V_s}^2 - 4J^2}/(\hbar\tilde{\alpha})$. This is consistent with our numerical calculations of the RCSJ model.

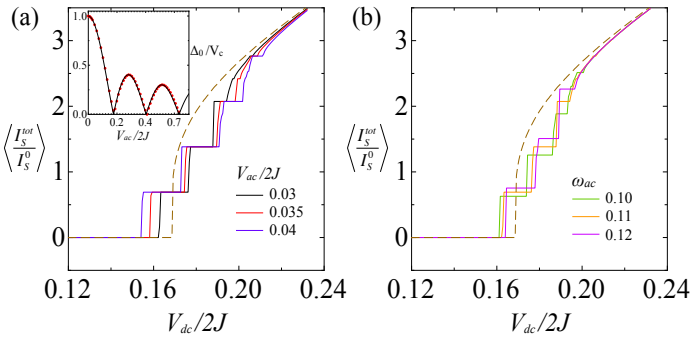

Figure 6.3: Numerical results of the mode locking for: (a) different rf power with fixed frequency $\omega_{ac} = 0.11$ and (b) different frequencies with fixed amplitude $V_{ac}/2J = 0.03$. The brown dashed line represents the case with d.c. input only. The damping constant is 0.1. Inset: The width of the 0 step Δ_0 as a function of the ac input V_{ac}. Red dots are the numerical results, the solid line is a fit to the $|J_0|$ Bessel function.

6.4 Spin Shapiro Steps

The spin oscillations also exhibit Shapiro step like dynamics in the presence of an ac input [125]. An ac spin chemical potential of the form of $V_{s,i}(t) = -V_{s,-i}(t) = V_{d.c.} + V_{ac}\sin(\omega_{ac}t)$ can be induced by applying an ac electric current in the HMs. In a simple model, when ω_{ac} is an integer multiple of ω_0, mode-locking of the input signal and the magnetization dynamics can occur. This results in a Shapiro step like behavior in the time averaged pumped spin current I_s within the HM. The dynamics of the system with ac input are determined by solving Eq. 6.6 with a time dependent source V_s.

In order to explore the role of ω_{ac} and V_{ac}, we calculate the time averaged I_s as a function of V_s. The results for different V_{ac} and ω_{ac} are shown in Fig. 6.3(a) and Fig. 6.3(b), respectively. The normalized spin current I_s^{tot}/I_s^0 is plotted where $I_s^0 = \hbar g_s \omega_0/4\pi$ is the characteristic spin current associated with the junction. When $V_{ac} = 0$, the time averaged I_s-V_s shows a non-linear relationship with $V_{d.c.}$ [2]. After increasing V_{ac} to a finite value, the I_s-V_s curve shows several steps, in the averaged spin current.

At each step, the oscillation frequency and maximum oscillation amplitude depends on V_{dc}. The step position in the time averaged I_s has complicated dependence on V_{dc}, ω_{ac} and V_{ac}. Both V_{ac} and ω_{ac} strongly influence the d.c. critical value and the step width, whereas the step height only depends on ω_{ac}. As shown in Fig. 6.3, finite V_{ac} can reduce the critical value required for a persistent oscillation. Furthermore, the width of the n^{th} step as a function of $V_{ac}/2J$ has a form of the first kind Bessel function $|J_n(V_{ac}/2J)|$, which is characteristic of the Shapiro steps [126] in superconducting Josephson junctions. The complicated magnetization dynamics of SSJ oscillators can be determined from the MR, we discuss this in the next section.

6.5 Magnetoresistance

The presence of spin pumping effect generates an additional electromotive force,

$$\boldsymbol{\Delta E}_i = i\frac{\hbar g_s \theta_{\rm SH}}{2ed_{\rm HM}}(\mathbf{s}_i \times \dot{\mathbf{s}}_i) \times \hat{\mathbf{y}} \tag{6.7}$$

where $i = \pm$ denotes the top and bottom HM contacts with thickness d_{HM}, and effective spin Hall angle θ_{SH}. The current in HM contacts is modified to $\mathbf{j} = (\mathbf{E} + \boldsymbol{\Delta}\mathbf{E})/\rho$, where the first term is the intrinsic circuit contribution, ρ is the resistivity and j is the electrical

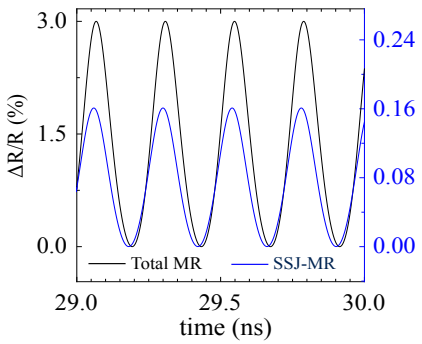

Figure 6.4: Steady-state oscillation of the magnetoresistance for SSJ-MR and total MR.

current density. Eq. 6.7 indicates that the magnetization dynamics generate a MR in the SSJ junction, Therefore, the SSJ oscillations can be detected by purely electrical means.

One can apply Eq. 6.7 to our geometry of Fig 6.1 to determine the MR response. We restrict our analysis to the x-component of $\boldsymbol{\Delta E}$, since the y-component of $\boldsymbol{\Delta E}$ is small, for $s_i^z \ll 1$ we find $(\mathbf{s}_i \times \dot{\mathbf{s}}_i) \times \hat{\mathbf{y}} = \dot{\phi}_i \hat{\mathbf{x}}$. According to Eq. 6.7, $\mathbf{\Delta E} = \mathbf{E_i} - \mathbf{E_{-i}}$ is directly proportional to $\dot{\phi}$. Thus, the dynamics of $\dot{\phi}$ gives $\mathbf{\Delta E}$ a time-dependent contribution which results in an effective MR of the circuit with an oscillation frequency ω. The SSJ-MR with a d.c. electric current source in the HM contacts is plotted in the Fig. 6.4. The magnitude of the SSJ-MR signal is primarily determined by the spin-Hall angle θ_{SH}. With an ac source in the HM contact, Shapiro like steps also emerge in the time averaged MR.

In metallic SSJ oscillators, which consist of two easy-plane FM metals, additional contributions due to the in-plane giant magnetoresistance (GMR) will dominate the MR [127–131]. The GMR can be determined by, $R_{GMR} = R_0 + \Delta R_{GMR}(1 - cos(\phi))/2$. The relative angle ϕ varies due to the precession of the in-plane magnetization, resulting a large GMR contributions. To estimate the MR, we consider a device with 100 nm by 100nm lateral (in x-z plane) size. The junction consists of two 3 nm thick metallic easy-plane FMs seperated by a 2 nm non-magnetic metal. Typical GMR ratio for this junction geometry ranges from 5% to 15%. The junction is sandwiched by two 5 nm Pt contacts. Using the following parameters: spin Hall angle of Pt $\theta_{\rm SH} = 0.1$, electrical resistivity of Pt $\rho_{\rm Pt} = 2.1 \times 10^{-7}\Omega \cdot$ m, interfacial spin mixing conductance $g_s = 5 \times 10^{18}\mathrm{m}^{-2}$, GMR ratio 10%, sheet resistance of junction $R = 40\Omega$, we get the resistance change for both the GMR and SSJ-MR. The total MR for metallic SSJ oscillators with a d.c. source, plotted in Fig 6.4, is one order of magnitude larger that the MR

in insulating SSJ oscillators since only SSJ-MR exists in insulating systems. Other than GMR, the anisotropic magnetoresistance (AMR) also shows up in our system. However, due to the very thin thickness and large resistance of FM layers, AMR can be ignored here.

It is worth to mentioning that even though the SSJ-MR is small, in the time averaged ΔR-V_s, the Shapiro steps are still persisted. This is because the GMR only depends on the relative phase of the in-plane magnetization, and the amplitude ranges from 0 to ΔR, however ΔR does not change with $\dot{\phi}$. Thus, even in a metallic system, the non-linear ΔR-V_s and the Shapiro steps behavior still persists and is not buried by the large GMR effect.

6.6 Discussion

MR signals are commonly employed to estimate the output power of a spin torque nano-oscillator. For the SSJ oscillators, the 2π magnetization dynamics within the easy-plane could potentially boost the output power of the proposed device. In metallic SSJ junctions the full 2π precession angle provide access to the maximum values of the GMR for given ΔR. The output power here can achieve 90 nW to 300 nW depending on the GMR ratio.

Chapter 7

Conclusion and Outlook

To conclude, we first demonstrate single skyrmion creation and annihilation by spin waves in a crossbar geometry. The skyrmion creation results from the geometry change in the crossbar combined with the effective gauge field provided by the DM interaction acting on the spin wave. Skyrmion annihilation results from the emergent magnetic field of the skyrmion acting on the spin wave and the conservation of momentum between the spin wave and the skyrmion. A critical frequency is required both for the creation and the annihilation of a skyrmion. The heat assisted method for skyrmion creation reduces the minimum frequency required for creation. The minimum frequencies for creation and annihilation are similar, but the optimum frequency for creation that requires minimum spin-wave amplitude is below the critical frequency for skyrmion annihilation. If a skyrmion already exists in the cross bar region, a spin wave below the critical frequency causes it to circulate within the central region at an angular frequency about 3 orders of magnitude below the spin wave frequency.

For the skyrmion resonance modes, the out-of-plane spin wave modes of a confined skyrmion in nanodisks with different ARs are studied using micromagntic sim-

ulations. The skyrmion AR increases nonlinearly with increasing disk AR. New mixed modes appear in the spectrum with increasing AR, which originate from geometrical confinement and broken rotational symmetry of both the nanodisk and the skyrmion. The lowest mode of the skyrmion is still well below the first eigenmode of the FM state in the same geometry. Furthermore, two new modes appear below the lowest mode of the skyrmion with increasing AR, whereas in the FM state, no additional mode appears below the lowest frequency mode. This property can be used for measuring the skyrmion and AR in non-axial symmetric systems. New rotation and oscillation modes with different azimuthal and radial components are identified at AR=1.8, which still have characteristics of their original modes at AR=1.0. This study provides insight into the effect of asymmetry on skyrmion dynamics in confined nanodisk geometries. Such understanding is a step towards skyrmion based spin torque oscillators and spin wave sources [49].

In chapter 4, we show that a $Q_H = 1$ hopfion can be stabilized in a chiral magnet nanodisk sandwiched by two magnetic layers with PMA at zero external magnetic fields. The hopfion is identified by its preimages and the Hopf invariant. A MAP state is also stabilized at zero fields in the proposed structure. The ratio of the helical period L of the chiral magnet to the radius and thickness of the nanodisk determines which state is the ground state and which state is the metastable state. The minimal energy path calculation reveals the topological transition between the hopfion and the MAP state. 3D magnetic imaging techniques such as the X-ray vector nanotomography could be a powerful tool for visualizing the spin texture of hopfion in real space [132]. The hopfion may exhibit fascinating electronic transport and dynamical properties due to its novel topology. This work paves a way in the development of 3D spintronics and high dimensional memory architectures

In the second part, we first propose a novel effect in exchange coupled AFMIs that is the analogue of the Josephson effect in superfluids. Due to periodic dependence of the exchange energy on the relative phase difference, an oscillatory spin current flows through the metallic spacer that is proportional to the rate of change of the relative in-plane orientation of the Néel vector fields. A spin transfer torque induced by a spin chemical potential at one of the interfaces results in non-linear I_S-V_S characteristics that distinguish the proposed lateral spin valve heterostructure composed of AFMIs and provide a signature of spin superfluidity. Furthermore, this heterostructure is an example of a pure spin AFMI terahertz oscillator [108].

Then, we proposed a new type of spin nano-oscillator based on the SSJ effect in FM. When exceeds critical value, a z-polarized spin chemical potential across the junction drives planar magnetization rotation. This spin oscillation is mediated by a spin superfluid mode and directly related to the phase difference between the two FMs. The oscillation frequency is highly tunable via the spin chemical potential. Furthermore, as a response of ac input, Shapiro steps appear in the I_s-V_s curve, which is a signature of mode-locking between the ac input and the magnetization oscillations. All the magnetization dynamics has been investigated within a magnetoresistance formalism, which can be directly measured experimentally. The time-averaged magnetization dynamics provides additional signatures for spin superfluidity. The 2π precession angle of the spin superfluid mode can maximize the GMR and AMR, thus opens an alternative routine towards building high power spin oscillators.

Appendix A

LLG Equations for AFM spin Josephson effect

For an antiferromagnet with two sublattices $\boldsymbol{m_1}$ and $\boldsymbol{m_2}$, we can write down the total magnetization $\boldsymbol{m} = \boldsymbol{m_1} + \boldsymbol{m_2}$ and the Néel order $\boldsymbol{n} = \boldsymbol{m_1} - \boldsymbol{m_2}$ with $|\boldsymbol{m}| << |\boldsymbol{n}| \approx 1$. Then the Hamiltonian for the two exchange coupled AFM layers shown in Fig. 6.1 is:

$$\mathcal{H} = \int [A(\nabla \mathbf{n}_L)^2 + \lambda \mathbf{m}_L \cdot \mathbf{m}_L + A(\nabla \mathbf{n}_R)^2 + \lambda \mathbf{m}_R \cdot \mathbf{m}_R + J\mathbf{m}_L \cdot \mathbf{m}_R + J\mathbf{n}_L \cdot \mathbf{n}_R] dr^3 \quad \text{(A.1)}$$

where A is the exchange constant, λ is the onsite exchange constant between two sublattices, and J is the interlayer exchange coupling between the left and right AFM. We assume the same A, J and λ for the two AFMs.

Now by the definition of effective field $H_{eff} = -\partial\mathcal{H}/\partial m$, we first derive the effective field for $\mathbf{m}_L$, $\mathbf{n}_L$, $\mathbf{m}_R$, $\mathbf{n}_R$ respectively.

$$\boldsymbol{H_{m_L}} = -\partial\mathcal{H}/\partial\mathbf{m}_L = -2\lambda\mathbf{m}_L - 2J\mathbf{m}_R \quad \text{(A.2)}$$

$$\boldsymbol{H_{n_L}} = -\partial\mathcal{H}/\partial\mathbf{n}_L = -A\nabla^2\mathbf{n}_L - 2J\mathbf{n}_R \tag{A.3}$$

$$\boldsymbol{H_{m_R}} = -\partial\mathcal{H}/\partial\mathbf{m}_R = -2\lambda\mathbf{m}_R - 2J\mathbf{m}_L \tag{A.4}$$

$$\boldsymbol{H_{n_R}} = -\partial\mathcal{H}/\partial\mathbf{n}_R = -A\nabla^2\mathbf{n}_R - 2J\mathbf{n}_L \tag{A.5}$$

Then the LLG equation of motion in $\boldsymbol{m}$ and $\boldsymbol{n}$ is:

$$\dot{\mathbf{n}}_L = \gamma\boldsymbol{H_{m_L}} \times \mathbf{n}_L - \alpha_1\dot{\mathbf{m}}_L \times \mathbf{n}_L \tag{A.6}$$

$$\dot{\mathbf{m}}_L = \gamma\boldsymbol{H_{n_L}} \times \mathbf{n}_L + \gamma\boldsymbol{H_{m_L}} \times \mathbf{m}_L - \alpha_1\dot{\mathbf{m}}_L \times \mathbf{m}_L - \alpha_2\dot{\mathbf{n}}_L \times \mathbf{n}_L \tag{A.7}$$

$$\dot{\mathbf{n}}_R = \gamma\boldsymbol{H_{m_R}} \times \mathbf{n}_R - \alpha_1\dot{\mathbf{m}}_R \times \mathbf{n}_R \tag{A.8}$$

$$\dot{\mathbf{m}}_R = \gamma\boldsymbol{H_{n_R}} \times \mathbf{n}_R + \gamma\boldsymbol{H_{m_R}} \times \mathbf{m}_R - \alpha_1\dot{\mathbf{m}}_R \times \mathbf{m}_R - \alpha_2\dot{\mathbf{n}}_R \times \mathbf{n}_R \tag{A.9}$$

The Néel order $\boldsymbol{n}$ and total magnetization $\boldsymbol{m}$ can be defined as

$$\mathbf{n}_L = (\cos\theta_L\cos\phi_L, \cos\theta_L\sin\phi_L, \sin\theta_L) \tag{A.10}$$

$$\mathbf{m}_L = (-m_{\theta_L}\sin\theta_L\cos\phi_L - m_{\phi_L}\sin\phi_L, -m_{\theta_L}\sin\theta_L\sin\phi_L + m_{\phi_L}\cos\phi L, m_{\theta_L}\cos\theta_L) \tag{A.11}$$

$$\mathbf{n}_R = (\cos\theta_R\cos\phi_R, \cos\theta_R\sin\phi_R, \sin\theta_R) \tag{A.12}$$

$$\mathbf{m}_R = (-m_{\theta_R}\sin\theta_R\cos\phi_R - m_{\phi_R}\sin\phi_R, -m_{\theta_R}\sin\theta_R\sin\phi_R + m_{\phi_R}\cos\phi R, m_{\theta_R}\cos\theta_R) \tag{A.13}$$

where θ is the angle relative to the $x-y$ plane and ϕ is the angle relative to the x axis. m_θ and m_ϕ are the two components transverse to the Néel order $\boldsymbol{n}$. In general, we assume the out-of-plane angle θ remains zero which gives an antiferromagnet order varying in the x-y plane only.

Then the Néel order and total magnetization become

$$\mathbf{n}_L = (\cos\phi_L, \sin\phi_L, 0) \tag{A.14}$$

$$\mathbf{m}_L = (-m_{\phi_L} \sin\phi_L, m_{\phi_L} \cos\phi L, m_{\theta_L}) \tag{A.15}$$

$$\mathbf{n}_R = (\cos\phi_R, \sin\phi_R, 0) \tag{A.16}$$

$$\mathbf{m}_R = (-m_{\phi_R} \sin\phi_R, m_{\phi_R} \cos\phi R, m_{\theta_R}) \tag{A.17}$$

and

$$\nabla^2 n_{L_x} = -\sin\phi_L \nabla^2\phi_L - \cos\phi_L (\nabla\phi_L)^2 \tag{A.18}$$

$$\nabla^2 n_{L_y} = -\sin\phi_L (\nabla\phi_L)^2 + \cos\phi_L \nabla^2\phi_L \tag{A.19}$$

$$\nabla^2 n_{L_z} = 0 \tag{A.20}$$

$$\dot{n}_{L_x} = -\sin\phi_L \dot{\phi}_L \tag{A.21}$$

$$\dot{n}_{L_y} = \cos\phi_L \dot{\phi}_L \tag{A.22}$$

$$\dot{n}_{L_z} = 0 \tag{A.23}$$

$$\dot{m}_{L_x} = -\dot{m}_{\phi_L} \sin\phi_L - m_{\phi_L} \cos\phi_L \dot{\phi}_L \tag{A.24}$$

$$\dot{m}_{L_y} = \dot{m}_{\phi_L} \cos\phi_L - m_{\phi_L} \sin\phi_L \dot{\phi}_L \tag{A.25}$$

$$\dot{m}_{L_z} = \dot{m}_{\theta_L} \tag{A.26}$$

$$\nabla^2 n_{R_x} = -\sin\phi_R \nabla^2\phi_R - \cos\phi_R (\nabla\phi_R)^2 \tag{A.27}$$

$$\nabla^2 n_{R_y} = -\sin\phi_R (\nabla\phi_R)^2 + \cos\phi_R \nabla^2\phi_R \tag{A.28}$$

$$\nabla^2 n_{R_z} = 0 \tag{A.29}$$

$$\dot{n}_{R_x} = -\sin\phi_R \dot{\phi}_R \tag{A.30}$$

$$\dot{n}_{R_y} = \cos\phi_R \dot{\phi}_R \tag{A.31}$$

$$\dot{n}_{R_z} = 0 \tag{A.32}$$

$$\dot{m}_{R_x} = -\dot{m}_{\phi_R} \sin\phi_R - m_{\phi_R} \cos\phi_R \dot{\phi}_R \tag{A.33}$$

$$\dot{m}_{R_y} = \dot{m}_{\phi_R} \cos\phi_R - m_{\phi_R} \sin\phi_R \dot{\phi}_R \tag{A.34}$$

$$\dot{m}_{R_z} = \dot{m}_{\theta_R} \tag{A.35}$$

Now that we have written down all of the equations and variables, we will begin to derive the equations of the spin Josephson effect.

First we expand the equation of motion for $\mathbf{m}$

$$\dot{\mathbf{m}}_L = -\gamma A \nabla^2 \mathbf{n}_L \times \mathbf{n}_L - 2\gamma J \mathbf{n}_R \times \mathbf{n}_L - 2\gamma J \mathbf{m}_R \times \mathbf{m}_L - \alpha_1 \dot{\mathbf{m}}_L \times \mathbf{m}_L - \alpha_2 \dot{\mathbf{n}}_L \times \mathbf{n}_L \tag{A.36}$$

$$\dot{\mathbf{m}}_R = -\gamma A \nabla^2 \mathbf{n}_R \times \mathbf{n}_R - 2\gamma J \mathbf{n}_L \times \mathbf{n}_R - 2\gamma J \mathbf{m}_L \times \mathbf{m}_R - \alpha_1 \dot{\mathbf{m}}_R \times \mathbf{m}_R - \alpha_2 \dot{\mathbf{n}}_R \times \mathbf{n}_R \tag{A.37}$$

and write down the explicit equation for z component $m_z(m_\theta)$

$$\begin{aligned} \dot{m}_{L_z} + \alpha_1(\dot{m}_{L_x} m_{L_y} - \dot{m}_{L_y} m_{L_x}) + \alpha_2(\dot{n}_{L_x} n_{L_y} - \dot{n}_{L_y} n_{L_x}) = -\gamma A(n_{L_y} \nabla^2 n_{L_x} - n_{L_x} \nabla^2 n_{L_y}) \\ - 2\gamma J(n_{R_x} n_{L_y} - n_{R_y} n_{L_x}) - 2\gamma J(m_{R_x} m_{L_y} - m_{R_y} m_{L_x}) \end{aligned} \tag{A.38}$$

$$\begin{aligned} \dot{m}_{R_z} + \alpha_1(\dot{m}_{R_x} m_{R_y} - \dot{m}_{R_y} m_{R_x}) + \alpha_2(\dot{n}_{R_x} n_{R_y} - \dot{n}_{R_y} n_{R_x}) = -\gamma A n_{R_y} \nabla^2 n_{R_x} - n_{R_x} \nabla^2 n_{R_y}) \\ - 2\gamma J(n_{L_x} n_{R_y} - n_{L_y} n_{R_x}) - 2\gamma J(m_{L_x} m_{R_y} - m_{L_y} m_{R_x}). \end{aligned} \tag{A.39}$$

After substituting all of the variables from section 1, we will have

$$\begin{aligned} \dot{m}_{\theta_L} + \alpha_1[-\dot{m}_{\phi_L} m_{\phi_L} \sin\phi_L \cos\phi_L - (m_{\phi_L})^2 \cos^2\phi_L \dot{\phi}_L + \dot{m}_{\phi_L} m_{\phi_L} \sin\phi_L \cos\phi_L \\ - (m_{\phi_L})^2 \sin^2\phi_L \dot{\phi}_L] + \alpha_2(-\sin^2\phi_L \dot{\phi}_L - \cos^2\phi_L \dot{\phi}_L) = -\gamma A[-\sin^2\phi_L \nabla^2 \phi_L \\ - \sin\phi_L \cos\phi_L (\nabla\phi_L)^2 - \cos^2\phi_L \nabla^2 \phi_L + \sin\phi_L \cos\phi_L (\nabla\phi_L)^2] \\ - 2\gamma J(\cos\phi_R \sin\phi_L - \sin\phi_R \cos\phi_L) \\ - 2\gamma J(-m_{\phi_L} m_{\phi_R} \sin\phi_R \cos\phi_L + m_{\phi_L} m_{\phi_R} \cos\phi_R \sin\phi_L) \end{aligned} \tag{A.40}$$

$$\dot{m}_{\theta_R} + \alpha_1[-\dot{m}_{\phi_R} m_{\phi_R} \sin\phi_R \cos\phi_R - (m_{\phi_R})^2 \cos^2\phi_R \dot{\phi}_R + \dot{m}_{\phi_R} m_{\phi_R} \sin\phi_R \cos\phi_R$$
$$- (m_{\phi_R})^2 \sin^2\phi_R \dot{\phi}_R] + \alpha_2(-\sin^2\phi_R \dot{\phi}_R - \cos^2\phi_R \dot{\phi}_R) = -\gamma A[-\sin^2\phi_R \nabla^2\phi_R$$
$$- \sin\phi_R \cos\phi_R (\nabla\phi_R)^2 - \cos^2\phi_R \nabla^2\phi_R + \sin\phi_R \cos\phi_R (\nabla\phi_R)^2]$$
$$+ 2\gamma J(\cos\phi_R \sin\phi_L - \sin\phi_R \cos\phi_L)$$
$$+ 2\gamma J(-m_{\phi_L} m_{\phi_R} \sin\phi_R \cos\phi_L + m_{\phi_L} m_{\phi_R} \cos\phi_R \sin\phi_L) \quad \text{(A.41)}$$

After cancellation, combination, and ignoring small second order terms like $(m_\phi)^2$, $(m_\theta)^2$, $m_\theta m_\phi$, we get

$$\dot{m}_{\theta_L} - \alpha_2 \dot{\phi}_L = -2\gamma \sin(\phi_L - \phi_R) \quad \text{(A.42)}$$

and

$$\dot{m}_{\theta_R} - \alpha_2 \dot{\phi}_R = 2\gamma \sin(\phi_L - \phi_R) \quad \text{(A.43)}$$

Equations (A.42) and (A.43) describe the spin Josephson effect. This relationship is analogous to the Josephson effect $I = I_c \sin(\Delta\phi)$ in a superconductor.

Next we will derive equations for the order parameter ϕ. Expand the equation of motion for $\mathbf{n}$

$$\dot{\mathbf{n}}_L + \alpha_1 \dot{\mathbf{m}}_L \times \mathbf{n}_L = -2\gamma\lambda \mathbf{m}_L \times \mathbf{n}_L - 2\gamma J \mathbf{m}_R \times \mathbf{n}_L \quad \text{(A.44)}$$

$$\dot{\mathbf{n}}_R + \alpha_1 \dot{\mathbf{m}}_R \times \mathbf{n}_R = -2\gamma\lambda \mathbf{m}_R \times \mathbf{n}_R - 2\gamma J \mathbf{m}_L \times \mathbf{n}_R \quad \text{(A.45)}$$

Then write down the explicit equation for n_{L_x} and n_{L_y}

$$\dot{n}_{L_x} - \alpha_1 \dot{m}_{L_z} n_{L_y} = 2\gamma\lambda m_{L_z} n_{L_y} + 2\gamma J m_{R_z} n_{L_y} \quad \text{(A.46)}$$

$$\dot{n}_{L_y} + \alpha_1 \dot{m}_{L_z} n_{L_x} = -2\gamma\lambda m_{L_z} n_{L_x} - 2\gamma J m_{R_z} n_{L_x} \quad \text{(A.47)}$$

$$\dot{n}_{R_x} - \alpha_1 \dot{m}_{R_z} n_{R_y} = 2\gamma\lambda m_{R_z} n_{R_y} + 2\gamma J m_{L_z} n_{R_y} \quad \text{(A.48)}$$

$$\dot{n}_{R_y} + \alpha_1 \dot{m}_{R_z} n_{R_x} = -2\gamma\lambda m_{R_z} n_{R_x} - 2\gamma J m_{L_z} n_{R_x} \tag{A.49}$$

After substituting all of the variables in equations (A.46)–(A.49), we get

$$-\sin\phi_L \dot{\phi}_L - \alpha_1 \dot{m}_{\theta_L} \sin\phi_L = 2\gamma\lambda m_{\theta_L} \sin\phi_L + 2\gamma J m_{\theta_R} \sin\phi_L \tag{A.50}$$

$$\cos\phi_L \dot{\phi}_L + \alpha_1 \dot{m}_{\theta_L} \cos\phi_L = -2\gamma\lambda m_{\theta_L} \cos\phi_L - 2\gamma J m_{\theta_R} \cos\phi_L \tag{A.51}$$

$$-\sin\phi_R \dot{\phi}_R - \alpha_1 \dot{m}_{\theta_R} \sin\phi_R = 2\gamma\lambda m_{\theta_R} \sin\phi_R + 2\gamma J m_{\theta_L} \sin\phi_R \tag{A.52}$$

$$\cos\phi_R \dot{\phi}_R + \alpha_1 \dot{m}_{\theta_R} \cos\phi_R = -2\gamma\lambda m_{\theta_R} \cos\phi_R - 2\gamma J m_{\theta_L} \cos\phi_R \tag{A.53}$$

Taking (A.50) $\times \sin\phi_L -$ (A.51) $\times \cos\phi_L$ and (A.52) $\times \sin\phi_R -$ (A.53) $\times \cos\phi_R$ gives

$$\dot{\phi}_L = -2\gamma\lambda m_{\theta_L} - 2\gamma J m_{\theta_R} - \alpha_1 \dot{m_{\theta_L}} \tag{A.54}$$

and

$$-\dot{\phi}_R = 2\gamma\lambda m_{\theta_R} + 2\gamma J m_{\theta_L} + \alpha_1 \dot{m_{\theta_R}} \tag{A.55}$$

Eqs. (A.54) and (A.55) are the equations for the order parameter ϕ. Now let $m_{\theta_L} - m_{\theta_R} = m_z$, $\phi_L - \phi_R = \phi$, take (A.42)-(A.43), and (A.54) + (A.55) to obtain

$$\dot{m}_z = -4\gamma J \sin(\phi) + \alpha_2 \dot{\phi} \tag{A.56}$$

and

$$\dot{\phi} = (2\gamma J - 2\gamma\lambda) m_z - \alpha_1 \dot{m}_z. \tag{A.57}$$

Eqs. (A.56) and (A.57) are the final equations for the spin Josephson effect in the two exchange–coupled AFM layers.

Appendix B

Hopf invariant in k-space

In real space, the integral form of the Hopf invariant is defined as [81]

$$H = -\int \mathbf{B}(\mathbf{r}) \cdot \mathbf{A}(\mathbf{r}) d\mathbf{r}, \tag{B.1}$$

where

$$B_i = \frac{1}{8\pi} \epsilon_{ijk}\, \mathbf{m} \cdot (\nabla_j \mathbf{m} \times \nabla_k \mathbf{m}), \tag{B.2}$$

$$\nabla \times \mathbf{A} = \mathbf{B}, \tag{B.3}$$

$\mathbf{m}$ is the local magnetic vector, $\mathbf{B}$ is the emergent magnetic field, $\mathbf{A}$ is the corresponding gauge potential, and ϵ is the Levi-Civita symbol.

To avoid solving for the explicit form of $\mathbf{A}$, we represent $\mathbf{A}$ in form of $\mathbf{B}$ in momentum space. To do this, we first perform a Fourier transformation on both $\mathbf{A}$ and $\mathbf{B}$ and get

$$\begin{aligned} \mathbf{A}(\mathbf{r}) &= \frac{1}{N} \sum \mathbf{A}(\mathbf{k}) e^{i2\pi \mathbf{k}\cdot\mathbf{r}}, \\ \mathbf{B}(\mathbf{r}) &= \frac{1}{N} \sum \mathbf{B}(\mathbf{k}) e^{i2\pi \mathbf{k}\cdot\mathbf{r}}, \end{aligned} \tag{B.4}$$

where N is the grid size of the system. In momentum space, Eq. (B.3) becomes

$$i2\pi \mathbf{k} \times \mathbf{A}(\mathbf{k}) = \mathbf{B}(\mathbf{k}). \tag{B.5}$$

Then, by using the Lagrange formula and the gauge relation $\mathbf{k} \cdot \mathbf{A} = 0$, we solve Eq. (B.5) to obtain the expression

$$\mathbf{A}(\mathbf{k}) = -i\frac{\mathbf{k} \times \mathbf{B}(\mathbf{k})}{2\pi\mathbf{k^2}}. \tag{B.6}$$

Substituting Eq. (B.6) into Eq. (B.1), the Hopf invariant in momentum space becomes

$$H = i\frac{1}{N}\sum_{\mathbf{k}} \frac{\mathbf{B}(-\mathbf{k}) \cdot (\mathbf{k} \times \mathbf{B}(\mathbf{k}))}{2\pi\mathbf{k^2}}. \tag{B.7}$$

All the Hopf invariant calculations in the main text were obtained using Eq. (B.7).

Appendix C

Simple Magnon Band

Let us consider a system with the following Hamiltonian

$$\mathcal{H} = -A(\nabla \mathbf{m})^2 + D\mathbf{m} \cdot (\nabla \times \mathbf{m}) - \frac{K_u}{2}(\mathbf{m} \cdot \mathbf{z})^2 - \mathbf{H}_{ext} \cdot \mathbf{m} \tag{C.1}$$

where A is the exchange constant, D is the bulk type DMI constant, K_u is the anisotropy constant with an easy-axis along the z-direction and $\mathbf{H}_{ext}$ is the external magnetic field. From Eq. C.1, we can get the effective field $\mathbf{h}_{eff} = -\frac{1}{\mu_0 M_s}\frac{\mathrm{d}\mathcal{H}}{\mathrm{d}\mathbf{m}}$ of the system

$$\mathbf{h}_{eff} = \frac{A}{\mu_0 M_s}\nabla^2 \mathbf{m} - \frac{2D}{\mu_0 M_S}(\nabla \times \mathbf{m}) + \frac{K_u}{\mu_0 Ms}(\mathbf{m} \cdot \mathbf{z})\mathbf{z} + \mathbf{h}_{ext} \cdot \mathbf{m} \tag{C.2}$$

Hereafter, we will use A_0, D_0 and K_0 instead of the full expressions of every term for simplicity. The LLG equation without damping can be written as

$$\dot{\mathbf{m}} = -\gamma \mathbf{m} \times \mathbf{h}_{eff} \tag{C.3}$$

Plugging in Eq. C.2 in the LLG equation, we will have

$$\dot{\mathbf{m}} = -\gamma \mathbf{m} \times [A_0 \nabla^2 \mathbf{m} - D_0(\nabla \times \mathbf{m}) + K_0(\mathbf{m} \cdot \mathbf{z})\mathbf{z} + \mathbf{h}_{ext} \cdot \mathbf{m}] \tag{C.4}$$

Assume the magnetic field is in z-direction and the anisotropy and external magnetic field is strong so that all the magnetizations point to z-direction. In the presence of small

perturbation, we can define $\mathbf{m} = m_0\mathbf{z} + \mathbf{m}_\perp$, where $\mathbf{m}_\perp$ is the lowest order perturbation term and $\mathbf{m}_\perp \cdot \mathbf{z} = 0$. Using this definition, the LLG equation becomes

$$\dot{\mathbf{m}}_\perp = -\gamma(m_0\mathbf{z} + \mathbf{m}_\perp) \times [A_0\nabla^2\mathbf{m}_\perp - D_0(\nabla \times \mathbf{m}_\perp) + K_0 m_0\mathbf{z} + h_{ext} \cdot m_0\mathbf{z}], \tag{C.5}$$

$$\dot{\mathbf{m}}_\perp = \gamma m_0\mathbf{z} \times [-A_0\nabla^2\mathbf{m}_\perp + D_0(\nabla \times \mathbf{m}_\perp) + K_0\mathbf{m}_\perp + h_{ext} \cdot \mathbf{m}_\perp] \tag{C.6}$$

Rewrite $\mathbf{m}_\perp$ in components $\mathbf{m}_\perp = m_x\mathbf{x} + m_y\mathbf{y}$, and also rewrite Eq. C.6 in components,

$$\frac{1}{\gamma}\dot{m}_x = A_0\nabla^2 m_y + D_0 m_0 \nabla m_x - K_0 m_y - h_{ext} m_y \tag{C.7}$$

$$\frac{1}{\gamma}\dot{m}_y = -A_0\nabla^2 m_x + D_0 m_0 \nabla m_y + K_0 m_x + h_{ext} m_x \tag{C.8}$$

Define $\psi = m_x - im_y$ and assume $m_0 \approx 1$. Then take Eq. (C.7) $- i$ Eq. (C.8) to obtain

$$\frac{1}{\gamma}\dot{\psi} = iA_0\nabla^2\psi + D_0\nabla\psi - iK_0\psi - ih_{ext}\psi. \tag{C.9}$$

Using a plan-wave solution $\psi = \psi_0 e^{i(\mathbf{k}\cdot\mathbf{r} - \omega t)}$ in Eq. (C.9) gives the magnon dispersion

$$\frac{1}{\gamma}\omega = A_0 k^2 \pm D_0 k + (K_0 + h_{ext}). \tag{C.10}$$

The dispersion is a parabolic band with horizontal shift in k due to the DMI and a vertical shift in frequency due to the anisotropy and the external magnetic field.

Bibliography

[1] Yizhou Liu, Gen Yin, Jiadong Zang, Jing Shi, and Roger K. Lake. Skyrmion creation and annihilation by spin waves. *Appl. Phys. Lett.*, 107(15):152411, October 2015.

[2] Yizhou Liu, Gen Yin, Jiadong Zang, Roger K. Lake, and Yafis Barlas. Spin-Josephson effects in exchange coupled antiferromagnetic insulators. *Phys. Rev. B*, 94(9):094434, September 2016.

[3] Yizhou Liu, Roger K. Lake, and Jiadong Zang. Shape dependent resonant modes of skyrmions in magnetic nanodisks. *Journal of Magnetism and Magnetic Materials*, July 2017.

[4] Yizhou Liu, Roger K. Lake, and Jiadong Zang. Binding a Hopfion in chiral magnet nanodisk. (preprint, 2017).

[5] Yizhou Liu, Igor Barsukov, Ilya Krivorotov, Yafis Barlas, and Roger K. Lake. Spin superfluid Josephson oscillator. (preprint, 2017).

[6] Albert Fert, Vincent Cros, and João Sampaio. Skyrmions on the track. *Nat. Nanotech.*, 8(3):152, March 2013.

[7] A. Loidl, C. D. Dewhurst, D. Ehlers, E. Neuber, H. Nakamura, H. M. Rnnow, I. Kzsmrki, J. S. White, K. Yanai, L. M. Eng, M. Mochizuki, P. Milde, S. Bordcs, and V. Tsurkan. Nel-type skyrmion lattice with confined orientation in the polar magnetic semiconductor GaV_4S_8. *Nature Materials*, 14(11):1116, November 2015.

[8] G. E. Moore. Cramming more components onto integrated circuits, Reprinted from Electronics, volume 38, number 8, April 19, 1965, pp.114 ff. *IEEE Solid-State Circuits Society Newsletter*, 11(3):33–35, September 2006.

[9] Tôru Moriya. Anisotropic Superexchange Interaction and Weak Ferromagnetism. *Physical Review*, 120(1):91–98, October 1960.

[10] I. Dzyaloshinsky. A thermodynamic theory of "weak" ferromagnetism of antiferromagnetics. *Journal of Physics and Chemistry of Solids*, 4(4):241–255, 1958.

[11] J. C. Slonczewski. Current-driven excitation of magnetic multilayers. *Journal of Magnetism and Magnetic Materials*, 159(1):L1–L7, June 1996.

[12] L. Berger. Emission of spin waves by a magnetic multilayer traversed by a current. *Phys. Rev. B*, 54(13):9353–9358, October 1996.

[13] Naoto Nagaosa and Yoshinori Tokura. Topological properties and dynamics of magnetic skyrmions. *Nature Nanotechnology*, 8(12):899–911, December 2013.

[14] S. Mühlbauer, B. Binz, F. Jonietz, C. Pfleiderer, A. Rosch, A. Neubauer, R. Georgii, and P. Böni. Skyrmion Lattice in a Chiral Magnet. *Science*, 323(5916):915–919, February 2009.

[15] X. Z. Yu, Y. Onose, N. Kanazawa, J. H. Park, J. H. Han, Y. Matsui, N. Nagaosa, and Y. Tokura. Real-space observation of a two-dimensional skyrmion crystal. *Nature*, 465(7300):901–904, June 2010.

[16] Stefan Heinze, Kirsten von Bergmann, Matthias Menzel, Jens Brede, André Kubetzka, Roland Wiesendanger, Gustav Bihlmayer, and Stefan Blügel. Spontaneous atomic-scale magnetic skyrmion lattice in two dimensions. *Nature Physics*, 7(9):713–718, September 2011.

[17] X. Z. Yu, N. Kanazawa, W. Z. Zhang, T. Nagai, T. Hara, K. Kimoto, Y. Matsui, Y. Onose, and Y. Tokura. Skyrmion flow near room temperature in an ultralow current density. *Nature Communications*, 3:988, August 2012.

[18] J.S. White, K. Prša, P. Huang, A.A. Omrani, I. Živković, M. Bartkowiak, H. Berger, A. Magrez, J.L. Gavilano, G. Nagy, J. Zang, and H.M. Rønnow. Electric-Field-Induced Skyrmion Distortion and Giant Lattice Rotation in the Magnetoelectric Insulator ${\mathrm{Cu}}_{2}{\mathrm{OSeO}}_{3}$. *Physical Review Letters*, 113(10):107203, September 2014.

[19] Lingyao Kong and Jiadong Zang. Dynamics of an Insulating Skyrmion under a Temperature Gradient. *Physical Review Letters*, 111(6):067203, August 2013.

[20] Shi-Zeng Lin, Cristian D. Batista, Charles Reichhardt, and Avadh Saxena. ac Current Generation in Chiral Magnetic Insulators and Skyrmion Motion induced by the Spin Seebeck Effect. *Physical Review Letters*, 112(18):187203, May 2014.

[21] F. Jonietz, S. Mühlbauer, C. Pfleiderer, A. Neubauer, W. Münzer, A. Bauer, T. Adams, R. Georgii, P. Böni, R. A. Duine, K. Everschor, M. Garst, and A. Rosch. Spin Transfer Torques in MnSi at Ultralow Current Densities. *Science*, 330(6011):1648–1651, December 2010.

[22] T. Schulz, R. Ritz, A. Bauer, M. Halder, M. Wagner, C. Franz, C. Pfleiderer, K. Everschor, M. Garst, and A. Rosch. Emergent electrodynamics of skyrmions in a chiral magnet. *Nature Physics*, 8(4):301–304, April 2012.

[23] Junichi Iwasaki, Aron J. Beekman, and Naoto Nagaosa. Theory of magnon-skyrmion scattering in chiral magnets. *Physical Review B*, 89(6):064412, February 2014.

[24] M. Mochizuki, X. Z. Yu, S. Seki, N. Kanazawa, W. Koshibae, J. Zang, M. Mostovoy, Y. Tokura, and N. Nagaosa. Thermally driven ratchet motion of a skyrmion microcrystal and topological magnon Hall effect. *Nature Materials*, 13(3):241–246, March 2014.

[25] Niklas Romming, Christian Hanneken, Matthias Menzel, Jessica E. Bickel, Boris Wolter, Kirsten von Bergmann, André Kubetzka, and Roland Wiesendanger. Writing and Deleting Single Magnetic Skyrmions. *Science*, 341(6146):636–639, August 2013.

[26] J. Sampaio, V. Cros, S. Rohart, A. Thiaville, and A. Fert. Nucleation, stability and current-induced motion of isolated magnetic skyrmions in nanostructures. *Nature Nanotechnology*, 8(11):839–844, November 2013.

[27] Shi-Zeng Lin, Charles Reichhardt, and Avadh Saxena. Manipulation of skyrmions in nanodisks with a current pulse and skyrmion rectifier. *Applied Physics Letters*, 102(22):222405, June 2013.

[28] Gen Yin, Yufan Li, Lingyao Kong, Roger K. Lake, C. L. Chien, and Jiadong Zang. Topological Charge Analysis of Single Skyrmion Creation with a Nanosecond Current Pulse. *arXiv:1411.7762 [cond-mat]*, November 2014.

[29] Youngbin Tchoe and Jung Hoon Han. Skyrmion generation by current. *Physical Review B*, 85(17):174416, May 2012.

[30] Wataru Koshibae and Naoto Nagaosa. Creation of skyrmions and antiskyrmions by local heating. *Nature Communications*, 5:5148, October 2014.

[31] Junichi Iwasaki, Masahito Mochizuki, and Naoto Nagaosa. Current-induced skyrmion dynamics in constricted geometries. *Nature Nanotechnology*, 8(10):742–747, October 2013.

[32] Wanjun Jiang, Pramey Upadhyaya, Wei Zhang, Guoqiang Yu, M. Benjamin Jungfleisch, Frank Y. Fradin, John E. Pearson, Yaroslav Tserkovnyak, Kang L. Wang, Olle Heinonen, Suzanne G. E. te Velthuis, and Axel Hoffmann. Blowing Magnetic Skyrmion Bubbles. *arXiv:1502.08028 [cond-mat]*, February 2015.

[33] Yan Zhou and Motohiko Ezawa. A reversible conversion between a skyrmion and a domain-wall pair in a junction geometry. *Nature Communications*, 5, August 2014.

[34] Gen Yin, Yizhou Liu, Yafis Barlas, Jiadong Zang, and Roger K. Lake. Topological Spin Hall Effect. *arXiv:1503.00242 [cond-mat]*, March 2015.

[35] Alexander Khitun. Magnonic holographic devices for special type data processing. *Journal of Applied Physics*, 113(16):164503, 2013.

[36] Su Do Yi, Shigeki Onoda, Naoto Nagaosa, and Jung Hoon Han. Skyrmions and anomalous Hall effect in a Dzyaloshinskii-Moriya spiral magnet. *Physical Review B*, 80(5):054416, August 2009.

[37] José Luis García-Palacios and Francisco J. Lázaro. Langevin-dynamics study of the dynamical properties of small magnetic particles. *Physical Review B*, 58(22):14937–14958, December 1998.

[38] Y. Onose, T. Ideue, H. Katsura, Y. Shiomi, N. Nagaosa, and Y. Tokura. Observation of the Magnon Hall Effect. *Science*, 329(5989):297–299, July 2010.

[39] M.H. Kryder, E.C. Gage, T.W. McDaniel, W.A. Challener, R.E. Rottmayer, Ganping Ju, Yiao-Tee Hsia, and M.F. Erden. Heat Assisted Magnetic Recording. *Proceedings of the IEEE*, 96(11):1810–1835, November 2008.

[40] A. A. Thiele. Steady-State Motion of Magnetic Domains. *Phys. Rev. Lett.*, 30(6):230–233, February 1973.

[41] S. Rohart and A. Thiaville. Skyrmion confinement in ultrathin film nanostructures in the presence of Dzyaloshinskii-Moriya interaction. *Phys. Rev. B*, 88(18):184422, November 2013.

[42] Olivier Boulle, Jan Vogel, Hongxin Yang, Stefania Pizzini, Dayane de Souza Chaves, Andrea Locatelli, Tevfik Onur Menteş, Alessandro Sala, Liliana D. Buda-Prejbeanu, Olivier Klein, Mohamed Belmeguenai, Yves Roussigné, Andrey Stashkevich, Salim Mourad Chérif, Lucia Aballe, Michael Foerster, Mairbek Chshiev, Stéphane Auffret, Ioan Mihai Miron, and Gilles Gaudin. Room-temperature chiral magnetic skyrmions in ultrathin magnetic nanostructures. *Nat Nano*, 11(5):449–454, May 2016.

[43] Aakash Pushp, Timothy Phung, Charles Rettner, Brian P. Hughes, See-Hun Yang, Luc Thomas, and Stuart S. P. Parkin. Domain wall trajectory determined by its fractional topological edge defects. *Nat Phys*, 9(8):505–511, August 2013.

[44] Joo-Von Kim, Felipe Garcia-Sanchez, João Sampaio, Constance Moreau-Luchaire, Vincent Cros, and Albert Fert. Breathing modes of confined skyrmions in ultrathin magnetic dots. *Phys. Rev. B*, 90(6):064410, August 2014.

[45] Marijan Beg, Maximilian Albert, Marc-Antonio Bisotti, David Cortés-Ortuño, Weiwei Wang, Rebecca Carey, Mark Vousden, Ondrej Hovorka, Chiara Ciccarelli, Charles S. Spencer, Christopher H. Marrows, and Hans Fangohr. Dynamics of skyrmionic states in confined helimagnetic nanostructures. *Phys. Rev. B*, 95(1):014433, January 2017.

[46] A. R. Fert. Magnetic and Transport Properties of Metallic Multilayers. *Materials Science Forum*, 59-60:439–480, 1990.

[47] Arne Vansteenkiste, Jonathan Leliaert, Mykola Dvornik, Mathias Helsen, Felipe Garcia-Sanchez, and Bartel Van Waeyenberge. The design and verification of MuMax3. *AIP Advances*, 4(10):107133, October 2014.

[48] O. Gérardin, H. Le Gall, M. J. Donahue, and N. Vukadinovic. Micromagnetic calculation of the high frequency dynamics of nano-size rectangular ferromagnetic stripes. *Journal of Applied Physics*, 89(11):7012–7014, June 2001.

[49] Sebastian Wintz, Vasil Tiberkevich, Markus Weigand, Jörg Raabe, Jürgen Lindner, Artur Erbe, Andrei Slavin, and Jürgen Fassbender. Magnetic vortex cores as tunable spin-wave emitters. *Nat Nano*, 11(11):948–953, November 2016.

[50] Nicholas Manton and Paul Sutcliffe. *Topological Solitons*. Cambridge University Press, Cambridge, England, June 2004.

[51] T. H. R. Skyrme. A unified field theory of mesons and baryons. *Nucl. Phys.*, 31(Supplement C):556–569, March 1962.

[52] R. Rajaraman. *Solitons and Instantons*. North-holland, Amsterdam, Netherlands, 1987.

[53] G.E. Volovik and V.P. Mineev. Particle-like solitons in superfluid 3he phases. *Sov. Phys. JETP*, 46:401, 1977.

[54] Richard A. Battye and P. M. Sutcliffe. Knots as Stable Soliton Solutions in a Three-Dimensional Classical Field Theory. *Phys. Rev. Lett.*, 81(22):4798–4801, November 1998.

[55] Richard A. Battye and Paul M. Sutcliffe. Solitons, Links and Knots. *Proc. R. Soc. A*, 455(1992):4305–4331, 1999.

[56] Heinz Hopf. Über die Abbildungen der dreidimensionalen Sphäre auf die Kugelfläche. *Math. Ann.*, 104(1):637–665, December 1931.

[57] P.J. Hilton. *An Introduction to Homotopy Theory*. Cambridge University Press, Cambridge, England, 1953.

[58] L. Faddeev and Antti J. Niemi. Stable knot-like structures in classical field theory. *Nature*, 387(6628):58–61, May 1997.

[59] L. Faddeev and A. J. Niemi. Toroidal Confugurations As Stable Solitons. *arXiv:hep-th/9705176*, May 1997. arXiv: hep-th/9705176.

[60] Dustin Kleckner and William T. M. Irvine. Creation and dynamics of knotted vortices. *Nat. Phys.*, 9(4):253–258, April 2013.

[61] Dustin Kleckner, Louis H. Kauffman, and William T. M. Irvine. How superfluid vortex knots untie. *Nat. Phys.*, 12(7):650–655, July 2016.

[62] Mark R. Dennis, Robert P. King, Barry Jack, Kevin O'Holleran, and Miles J. Padgett. Isolated optical vortex knots. *Nat. Phys.*, 6(2):118–121, February 2010.

[63] Yuki Kawaguchi, Muneto Nitta, and Masahito Ueda. Knots in a Spinor Bose-Einstein Condensate. *Phys. Rev. Lett.*, 100(18):180403, May 2008.

[64] Paul J. Ackerman, Jao van de Lagemaat, and Ivan I. Smalyukh. Self-assembly and electrostriction of arrays and chains of hopfion particles in chiral liquid crystals. *Nat. Commun.*, 6:6012, January 2015.

[65] Paul J. Ackerman and Ivan I. Smalyukh. Static three-dimensional topological solitons in fluid chiral ferromagnets and colloids. *Nat. Mater.*, 16(4):426–432, April 2017.

[66] D. S. Hall, M. W. Ray, K. Tiurev, E. Ruokokoski, A. H. Gheorghe, and M. Möttönen. Tying quantum knots. *Nat. Phys.*, 12(5):478–483, May 2016.

[67] U. K. Rößler, A. N. Bogdanov, and C. Pfleiderer. Spontaneous skyrmion ground states in magnetic metals. *Nature*, 442(7104):797–801, August 2006.

[68] N. R. Cooper. Propagating Magnetic Vortex Rings in Ferromagnets. *Phys. Rev. Lett.*, 82(7):1554–1557, February 1999.

[69] Paul Sutcliffe. Vortex rings in ferromagnets: Numerical simulations of the time-dependent three-dimensional Landau-Lifshitz equation. *Phys. Rev. B*, 76(18):184439, November 2007.

[70] A. B. Borisov and F. N. Rybakov. Stationary precession topological solitons with nonzero Hopf invariant in a uniaxial ferromagnet. *JETP Lett.*, 88(4):264–267, October 2008.

[71] Paul Sutcliffe. Skyrmion Knots in Frustrated Magnets. *Phys. Rev. Lett.*, 118(24):247203, June 2017.

[72] Haifeng Du, Wie Ning, Mingliang Tian, and Yuheng Zhang. Magnetic vortex with skyrmionic core in a thin nanodisk of chiral magnets. *Europhys. Lett.*, 101(3):37001, 2013.

[73] A. O. Leonov, U. K. Rößler, and M. Mostovoy. Target-skyrmions and skyrmion clusters in nanowires of chiral magnets. *EPJ Web Conf.*, 75:05002, 2014.

[74] Marijan Beg, Rebecca Carey, Weiwei Wang, David Corts-Ortuo, Mark Vousden, Marc-Antonio Bisotti, Maximilian Albert, Dmitri Chernyshenko, Ondrej Hovorka, Robert L. Stamps, and Hans Fangohr. Ground state search, hysteretic behaviour, and reversal mechanism of skyrmionic textures in confined helimagnetic nanostructures. *Sci. Rep.*, 5:17137, November 2015.

[75] Fengshan Zheng, Hang Li, Shasha Wang, Dongsheng Song, Chiming Jin, Wenshen Wei, Andrs Kovcs, Jiadong Zang, Mingliang Tian, Yuheng Zhang, Haifeng Du, and Rafal E. Dunin-Borkowski. Direct Imaging of a Zero-Field Target Skyrmion and Its Polarity Switch in a Chiral Magnetic Nanodisk. *Phys. Rev. Lett.*, 119(19):197205, November 2017.

[76] Arne Vansteenkiste, Jonathan Leliaert, Mykola Dvornik, Mathias Helsen, Felipe Garcia-Sanchez, and Bartel Van Waeyenberge. The design and verification of MuMax3. *AIP Advances*, 4(10):107133, October 2014.

[77] David Cortés-Ortuño, Weiwei Wang, Ryan Pepper, Marc-Antonio Bisotti, Thomas Kluyver, Mark Vousden, and Hans Fangohr. Fidimag v2.0. Technical report, Zenodo, November 2016. DOI: 10.5281/zenodo.167858.

[78] *Spirit spin simulation framework, (see https://spirit-code.github.io).*

[79] J. W. Milnor. *Topology from the Differentiable Viewpoint.* Princeton University Press, Princeton, 1997.

[80] J. H. C. Whitehead. An Expression of Hopf's Invariant as an Integral. *Proc. Natl. Acad. Sci. U.S.A.*, 33(5):117–123, May 1947.

[81] Frank Wilczek and A. Zee. Linking Numbers, Spin, and Statistics of Solitons. *Phys. Rev. Lett.*, 51(25):2250–2252, December 1983.

[82] Joel E. Moore, Ying Ran, and Xiao-Gang Wen. Topological Surface States in Three-Dimensional Magnetic Insulators. *Phys. Rev. Lett.*, 101(18):186805, October 2008.

[83] Pavel F. Bessarab, Valery M. Uzdin, and Hannes Jónsson. Method for finding mechanism and activation energy of magnetic transitions, applied to skyrmion and antivortex annihilation. *Comput. Phys. Commun.*, 196(Supplement C):335–347, November 2015.

[84] David Cortés-Ortuño, Weiwei Wang, Marijan Beg, Ryan A. Pepper, Marc-Antonio Bisotti, Rebecca Carey, Mark Vousden, Thomas Kluyver, Ondrej Hovorka, and Hans Fangohr. Thermal stability and topological protection of skyrmions in nanotracks. *Sci. Rep.*, 7(1):4060, June 2017.

[85] P. F. Bessarab, G. P. Müller, I. S. Lobanov, F. N. Rybakov, N. S. Kiselev, H. Jónsson, V. M. Uzdin, S. Blügel, L. Bergqvist, and A. Delin. Annihilation mechanisms and lifetime of racetrack skyrmions. *arXiv:1706.07173 [cond-mat]*, June 2017. arXiv: 1706.07173.

[86] Ying Ran, Pavan Hosur, and Ashvin Vishwanath. Fermionic Hopf solitons and Berry phase in topological surface superconductors. *Phys. Rev. B*, 84(18):184501, November 2011.

[87] Steven S.-L. Zhang and Shufeng Zhang. Magnon mediated electric current drag across a ferromagnetic insulator layer. *Phys. Rev. Lett.*, 109:096603, Aug 2012.

[88] Y. Kajiwara, K. Harii, S. Takahashi, J. Ohe, K. Uchida, M. Mizuguchi, H. Umezawa, H. Kawai, K. Ando, K. Takanashi, S. Maekawa, and E. Saitoh. Transmission of electrical signals by spin-wave interconversion in a magnetic insulator. *Nature*, 464(7286):262–266, March 2010.

[89] J. Li, Y. Xu, M. Aldosary, C. Tang, Z. Lin, S. Zhang, R. Lake, and J. Shi. Observation of magnon-mediated current drag in pt/yttrium iron garnet/pt(ta) trilayers. *Nat. Comm.*, 7:10858, Jan. 2016.

[90] Jürgen König, Martin Chr. Bønsager, and A. H. MacDonald. Dissipationless spin transport in thin film ferromagnets. *Phys. Rev. Lett.*, 87:187202, Oct 2001.

[91] So Takei and Yaroslav Tserkovnyak. Superfluid spin transport through easy-plane ferromagnetic insulators. *Phys. Rev. Lett.*, 112:227201, Jun 2014.

[92] Hua Chen, Andrew D. Kent, Allan H. MacDonald, and Inti Sodemann. Nonlocal transport mediated by spin supercurrents. *Phys. Rev. B*, 90:220401, Dec 2014.

[93] So Takei and Yaroslav Tserkovnyak. Superfluid Spin Transport Through Easy-Plane Ferromagnetic Insulators. *Phys. Rev. Lett.*, 112(22):227201, June 2014.

[94] B. I. Halperin and P. C. Hohenberg. Hydrodynamic theory of spin waves. *Phys. Rev.*, 188:898–918, Dec 1969.

[95] E. B. Sonin. Magnon mediated electric current drag across a ferromagnetic insulator layer. *Adv. in Phys.*, 59:181, 2010.

[96] Hans Skarsvåg, Cecilia Holmqvist, and Arne Brataas. Spin superfluidity and long-range transport in thin-film ferromagnets. *Phys. Rev. Lett.*, 115:237201, Dec 2015.

[97] B. D. Josephson. Possible new effects in superconductive tunnelling. *Physics Letters*, 1(7):251–253, July 1962.

[98] Simone Borlenghi, Stefano Iubini, Stefano Lepri, Lars Bergqvist, Anna Delin, and Jonas Fransson. Coherent energy transport in classical nonlinear oscillators: An analogy with the Josephson effect. *Phys. Rev. E*, 91(4):040102, April 2015.

[99] F. D. M. Haldane. Nonlinear Field Theory of Large-Spin Heisenberg Antiferromagnets: Semiclassically Quantized Solitons of the One-Dimensional Easy-Axis N\'eel State. *Phys. Rev. Lett.*, 50(15):1153–1156, April 1983.

[100] P. Bruno. Theory of interlayer magnetic coupling. *Phys. Rev. B*, 52(1):411–439, July 1995.

[101] Assa Auerbach. *Interacting Electrons and Quantum Magnetism*. Graduate Texts in Contemporary Physics. Springer New York, New York, NY, 1994.

[102] Ran Cheng, Jiang Xiao, Qian Niu, and Arne Brataas. Spin Pumping and Spin-Transfer Torques in Antiferromagnets. *Phys. Rev. Lett.*, 113(5):057601, July 2014.

[103] Yaroslav Tserkovnyak, Arne Brataas, and Gerrit E. W. Bauer. Enhanced Gilbert Damping in Thin Ferromagnetic Films. *Phys. Rev. Lett.*, 88(11):117601, February 2002.

[104] Jairo Sinova, Sergio O. Valenzuela, J. Wunderlich, C.H. Back, and T. Jungwirth. Spin Hall effects. *Rev. Mod. Phys.*, 87(4):1213–1260, October 2015.

[105] Theodore Van Duzer and Charles William Turner. *Principles of Superconductive Devices and Circuits*. Prentice Hall, 1999.

[106] M. T. Hutchings and E. J. Samuelsen. Measurement of Spin-Wave Dispersion in NiO by Inelastic Neutron Scattering and Its Relation to Magnetic Properties. *Phys. Rev. B*, 6(9):3447–3461, November 1972.

[107] Y. Yafet. Ruderman-Kittel-Kasuya-Yosida range function of a one-dimensional free-electron gas. *Phys. Rev. B*, 36(7):3948–3949, September 1987.

[108] Ran Cheng, Di Xiao, and Arne Brataas. Terahertz Antiferromagnetic Spin Hall Nano-Oscillator. *Phys. Rev. Lett.*, 116(20):207603, May 2016.

[109] J. A. Katine, F. J. Albert, R. A. Buhrman, E. B. Myers, and D. C. Ralph. Current-Driven Magnetization Reversal and Spin-Wave Excitations in Co $/$Cu $/$Co Pillars. *Phys. Rev. Lett.*, 84(14):3149–3152, April 2000.

[110] J. Z Sun. Current-driven magnetic switching in manganite trilayer junctions. *Journal of Magnetism and Magnetic Materials*, 202(1):157–162, June 1999.

[111] M. Tsoi, A. G. M. Jansen, J. Bass, W.-C. Chiang, M. Seck, V. Tsoi, and P. Wyder. Excitation of a Magnetic Multilayer by an Electric Current. *Phys. Rev. Lett.*, 80(19):4281–4284, May 1998.

[112] S. I. Kiselev, J. C. Sankey, I. N. Krivorotov, N. C. Emley, R. J. Schoelkopf, R. A. Buhrman, and D. C. Ralph. Microwave oscillations of a nanomagnet driven by a spin-polarized current. *Nature*, 425(6956):380–383, September 2003.

[113] W. H. Rippard, M. R. Pufall, S. Kaka, S. E. Russek, and T. J. Silva. Direct-Current Induced Dynamics in Co90Fe10/Ni80Fe20 Point Contacts. *Phys. Rev. Lett.*, 92(2):027201, January 2004.

[114] I. N. Krivorotov, N. C. Emley, J. C. Sankey, S. I. Kiselev, D. C. Ralph, and R. A. Buhrman. Time-Domain Measurements of Nanomagnet Dynamics Driven by Spin-Transfer Torques. *Science*, 307(5707):228–231, January 2005.

[115] M. Collet, X. de Milly, O. d'Allivy Kelly, V. V. Naletov, R. Bernard, P. Bortolotti, J. Ben Youssef, V. E. Demidov, S. O. Demokritov, J. L. Prieto, M. Muñoz, V. Cros, A. Anane, G. de Loubens, and O. Klein. Generation of coherent spin-wave modes in yttrium iron garnet microdiscs by spin–orbit torque. *Nature Communications*, 7:10377, January 2016.

[116] A. Hamadeh, O. d'Allivy Kelly, C. Hahn, H. Meley, R. Bernard, A.H. Molpeceres, V.V. Naletov, M. Viret, A. Anane, V. Cros, S.O. Demokritov, J.L. Prieto, M. Muñoz, G. de Loubens, and O. Klein. Full Control of the Spin-Wave Damping in a Magnetic Insulator Using Spin-Orbit Torque. *Phys. Rev. Lett.*, 113(19):197203, November 2014.

[117] E.B. Sonin. Spin currents and spin superfluidity. *Advances in Physics*, 59(3):181–255, 2010.

[118] Jürgen König, Martin Chr. Bønsager, and A. H. MacDonald. Dissipationless spin transport in thin film ferromagnets. *Phys. Rev. Lett.*, 87:187202, Oct 2001.

[119] Hua Chen, Andrew D. Kent, Allan H. MacDonald, and Inti Sodemann. Nonlocal transport mediated by spin supercurrents. *Phys. Rev. B*, 90:220401, Dec 2014.

[120] So Takei, Bertrand I. Halperin, Amir Yacoby, and Yaroslav Tserkovnyak. Superfluid spin transport through antiferromagnetic insulators. *Phys. Rev. B*, 90(9):094408, September 2014.

[121] S. S. P. Parkin, N. More, and K. P. Roche. Oscillations in exchange coupling and magnetoresistance in metallic superlattice structures: Co/Ru, Co/Cr, and Fe/Cr. *Phys. Rev. Lett.*, 64(19):2304–2307, May 1990.

[122] Hans Skarsvåg, Cecilia Holmqvist, and Arne Brataas. Spin Superfluidity and Long-Range Transport in Thin-Film Ferromagnets. *Phys. Rev. Lett.*, 115(23):237201, December 2015.

[123] D. E. McCumber. Effect of ac Impedance on dc VoltageCurrent Characteristics of Superconductor WeakLink Junctions. *Journal of Applied Physics*, 39(7):3113–3118, June 1968.

[124] W. C. Stewart. Currentvoltage characteristics of josephson junctions. *Appl. Phys. Lett.*, 12(8):277–280, April 1968.

[125] Sidney Shapiro. Josephson Currents in Superconducting Tunneling: The Effect of Microwaves and Other Observations. *Phys. Rev. Lett.*, 11(2):80–82, July 1963.

[126] Sidney Shapiro, Andre R. Janus, and Sandor Holly. Effect of Microwaves on Josephson Currents in Superconducting Tunneling. *Rev. Mod. Phys.*, 36(1):223–225, January 1964.

[127] T. McGuire and R. Potter. Anisotropic magnetoresistance in ferromagnetic 3d alloys. *IEEE Transactions on Magnetics*, 11(4):1018–1038, July 1975.

[128] I. A. Campbell. Hall Effect and Resistivity Anisotropy in Ni Alloys. *Phys. Rev. Lett.*, 24(6):269–271, February 1970.

[129] G. Binasch, P. Grünberg, F. Saurenbach, and W. Zinn. Enhanced magnetoresistance in layered magnetic structures with antiferromagnetic interlayer exchange. *Phys. Rev. B*, 39(7):4828–4830, March 1989.

[130] M. N. Baibich, J. M. Broto, A. Fert, F. Nguyen Van Dau, F. Petroff, P. Etienne, G. Creuzet, A. Friederich, and J. Chazelas. Giant Magnetoresistance of (001)Fe/(001)Cr Magnetic Superlattices. *Phys. Rev. Lett.*, 61(21):2472–2475, November 1988.

[131] A. Hütten, S. Mrozek, S. Heitmann, T. Hempel, H. Brückl, and G. Reiss. Evolution of the GMR-effect amplitude in copper/permalloy-multilayered thin films. *Acta Materialia*, 47(15):4245–4252, November 1999.

[132] Claire Donnelly, Manuel Guizar-Sicairos, Valerio Scagnoli, Sebastian Gliga, Mirko Holler, Jörg Raabe, and Laura J. Heyderman. Three-dimensional magnetization structures revealed with X-ray vector nanotomography. *Nature*, 547(7663):328–331, July 2017.

[133] A. Kozhevnikov, F. Gertz, G. Dudko, Y. Filimonov, and A. Khitun. Pattern recognition with magnonic holographic memory device. *Applied Physics Letters*, 106(14):142409, April 2015.

[134] F. Gertz, A. Kozhevnikov, Y. Filimonov, and A. Khitun. Magnonic Holographic Memory. *IEEE Transactions on Magnetics*, 51(4):1–5, April 2015.

[135] Youngbin Tchoe and Jung Hoon Han. Skyrmion generation by current. *Physical Review B*, 85(17):174416, May 2012.

[136] Y. Onose, T. Ideue, H. Katsura, Y. Shiomi, N. Nagaosa, and Y. Tokura. Observation of the Magnon Hall Effect. *Science*, 329(5989):297–299, July 2010.

[137] Yan Zhou and Motohiko Ezawa. A reversible conversion between a skyrmion and a domain-wall pair in a junction geometry. *Nature Communications*, 5, August 2014.

[138] Jung-Hwan Moon, Soo-Man Seo, Kyung-Jin Lee, Kyoung-Whan Kim, Jisu Ryu, Hyun-Woo Lee, R. D. McMichael, and M. D. Stiles. Spin-wave propagation in the presence of interfacial Dzyaloshinskii-Moriya interaction. *Physical Review B*, 88(18):184404, November 2013.

[139] D. Cortés-Ortuño and P. Landeros. Influence of the Dzyaloshinskii–Moriya interaction on the spin-wave spectra of thin films. *Journal of Physics: Condensed Matter*, 25(15):156001, April 2013.

[140] Masahito Mochizuki. Spin-Wave Modes and Their Intense Excitation Effects in Skyrmion Crystals. *Physical Review Letters*, 108(1):017601, January 2012.

[141] Youngbin Tchoe and Jung Hoon Han. Skyrmion generation by current. *Physical Review B*, 85(17):174416, May 2012.

[142] Youngbin Tchoe and Jung Hoon Han. Skyrmion generation by current. *Physical Review B*, 85(17):174416, May 2012.

[143] Jacob Torrejon, Mathieu Riou, Flavio Abreu Araujo, Sumito Tsunegi, Guru Khalsa, Damien Querlioz, Paolo Bortolotti, Vincent Cros, Akio Fukushima, Hitoshi Kubota, Shinji Yuasa, M. D. Stiles, and Julie Grollier. Neuromorphic computing with nanoscale spintronic oscillators. *arXiv:1701.07715 [cs]*, January 2017. arXiv: 1701.07715.

[144] J. Grollier, D. Querlioz, and M. D. Stiles. Spintronic Nanodevices for Bioinspired Computing. *Proceedings of the IEEE*, 104(10):2024–2039, October 2016.

[145] Alireza Qaiumzadeh, Hans Skarsvåg, Cecilia Holmqvist, and Arne Brataas. Spin Superfluidity in Biaxial Antiferromagnetic Insulators. *Phys. Rev. Lett.*, 118(13):137201, March 2017.

[146] So Takei and Yaroslav Tserkovnyak. Nonlocal Magnetoresistance Mediated by Spin Superfluidity. *Phys. Rev. Lett.*, 115(15):156604, October 2015.

[147] Yan-Ting Chen, Saburo Takahashi, Hiroyasu Nakayama, Matthias Althammer, Sebastian T. B. Goennenwein, Eiji Saitoh, and Gerrit E. W. Bauer. Theory of spin Hall magnetoresistance. *Phys. Rev. B*, 87(14):144411, April 2013.

[148] H. Nakayama, M. Althammer, Y.-T. Chen, K. Uchida, Y. Kajiwara, D. Kikuchi, T. Ohtani, S. Geprägs, M. Opel, S. Takahashi, R. Gross, G. E. W. Bauer, S. T. B. Goennenwein, and E. Saitoh. Spin Hall Magnetoresistance Induced by a Nonequilibrium Proximity Effect. *Phys. Rev. Lett.*, 110(20):206601, May 2013.

[149] B. D. Josephson. Possible new effects in superconductive tunnelling. *Physics Letters*, 1(7):251–253, July 1962.

[150] Yaroslav Tserkovnyak and Scott A. Bender. Spin Hall phenomenology of magnetic dynamics. *Phys. Rev. B*, 90(1):014428, July 2014.

[151] T. Jungwirth, X. Marti, P. Wadley, and J. Wunderlich. Antiferromagnetic spintronics. *Nat Nano*, 11(3):231–241, March 2016.

[152] J. C. Slonczewski. Current-driven excitation of magnetic multilayers. *Journal of Magnetism and Magnetic Materials*, 159(12):L1–L7, June 1996.

[153] L. Berger. Emission of spin waves by a magnetic multilayer traversed by a current. *Phys. Rev. B*, 54(13):9353–9358, October 1996.

[154] Yizhou Liu, Roger K. Lake, and Yafis Barlas. *(in preparation)*.

[155] G. Binasch, P. Grünberg, F. Saurenbach, and W. Zinn. Enhanced magnetoresistance in layered magnetic structures with antiferromagnetic interlayer exchange. *Phys. Rev. B*, 39:4828–4830, Mar 1989.

[156] B. I. HALPERIN and P. C. HOHENBERG. Hydrodynamic Theory of Spin Waves. *Phys. Rev.*, 188(2):898–918, December 1969.

[157] Igor Žutić, Jaroslav Fabian, and S. Das Sarma. Spintronics: Fundamentals and applications. *Rev. Mod. Phys.*, 76:323–410, Apr 2004.

[158] M. N. Baibich, J. M. Broto, A. Fert, F. Nguyen Van Dau, F. Petroff, P. Etienne, G. Creuzet, A. Friederich, and J. Chazelas. Giant magnetoresistance of (001)fe/(001)cr magnetic superlattices. *Phys. Rev. Lett.*, 61:2472–2475, Nov 1988.

[159] Erlend G. Tveten, Alireza Qaiumzadeh, and Arne Brataas. Antiferromagnetic Domain Wall Motion Induced by Spin Waves. *Phys. Rev. Lett.*, 112(14):147204, April 2014.

[160] V G Bar'yakhtar, B A Ivanov, and Mikhail V Chetkin. Dynamics of domain walls in weak ferromagnets. *Soviet Physics Uspekhi*, 28(7):563–588, July 1985.

[161] Yaroslav Tserkovnyak, Arne Brataas, Gerrit E. W. Bauer, and Bertrand I. Halperin. Nonlocal magnetization dynamics in ferromagnetic heterostructures. *Rev. Mod. Phys.*, 77(4):1375–1421, December 2005.

[162] E. M. Lifshitz and L. P. Pitaevskii. *Statistical Physics: Theory of the Condensed State*. Butterworth-Heinemann, Oxford, January 1980.

[163] Kjetil M. D. Hals, Yaroslav Tserkovnyak, and Arne Brataas. Phenomenology of Current-Induced Dynamics in Antiferromagnets. *Phys. Rev. Lett.*, 106(10):107206, March 2011.

[164] So Takei, Bertrand I. Halperin, Amir Yacoby, and Yaroslav Tserkovnyak. Superfluid spin transport through antiferromagnetic insulators. *Phys. Rev. B*, 90(9):094408, September 2014.

[165] Ran Cheng, Matthew W. Daniels, Jian-Gang Zhu, and Di Xiao. Ultrafast switching of antiferromagnets via spin-transfer torque. *Phys. Rev. B*, 91(6):064423, February 2015.

[166] Hua Chen, Andrew D. Kent, Allan H. MacDonald, and Inti Sodemann. Nonlocal transport mediated by spin supercurrents. *Phys. Rev. B*, 90(22):220401, December 2014.

[167] Erlend G. Tveten, Alireza Qaiumzadeh, O. A. Tretiakov, and Arne Brataas. Staggered Dynamics in Antiferromagnets by Collective Coordinates. *Phys. Rev. Lett.*, 110(12):127208, March 2013.

[168] P. Wadley, B. Howells, J. Železný, C. Andrews, V. Hills, R. P. Campion, V. Novák, K. Olejník, F. Maccherozzi, S. S. Dhesi, S. Y. Martin, T. Wagner, J. Wunderlich, F. Freimuth, Y. Mokrousov, J. Kuneš, J. S. Chauhan, M. J. Grzybowski, A. W. Rushforth, K. W. Edmonds, B. L. Gallagher, and T. Jungwirth. Electrical switching of an antiferromagnet. *Science*, page aab1031, January 2016.

[169] Michikazu Kobayashi and Muneto Nitta. Torus knots as Hopfions. *Physics Letters B*, 728:314–318, January 2014.

[170] Amalio Fernández-Pacheco, Robert Streubel, Olivier Fruchart, Riccardo Hertel, Peter Fischer, and Russell P. Cowburn. Three-dimensional nanomagnetism. *Nat. Commun.*, 8:15756, June 2017.

[171] Filipp N. Rybakov, Aleksandr B. Borisov, Stefan Blügel, and Nikolai S. Kiselev. New Type of Stable Particlelike States in Chiral Magnets. *Phys. Rev. Lett.*, 115(11):117201, September 2015.

[172] Zhongbo Yan, Ren Bi, and Zhong Wang. Majorana Zero Modes Protected by a Hopf Invariant in Topologically Trivial Superconductors. *Phys. Rev. Lett.*, 118(14):147003, April 2017.

[173] T. H. R. Skyrme. A non-linear field theory. *Proc. R. Soc. Lond. A*, 260(1300):127–138, February 1961.

[174] S. L. Sondhi, A. Karlhede, S. A. Kivelson, and E. H. Rezayi. Skyrmions and the crossover from the integer to fractional quantum Hall effect at small Zeeman energies. *Phys. Rev. B*, 47(24):16419–16426, June 1993.

[175] L. A. Takhtadzhyan and L. D. Faddeev. Essentially nonlinear one-dimensional model of classical field theory. *Theor Math Phys*, 21(2):1046–1057, November 1974.

[176] V. E. Korepin and L. D. Faddeev. Quantization of solitons. *Theor Math Phys*, 25(2):1039–1049, November 1975.

[177] Stuart S. P. Parkin, Masamitsu Hayashi, and Luc Thomas. Magnetic Domain-Wall Racetrack Memory. *Science*, 320(5873):190–194, April 2008.

[178] V. S. Pribiag, I. N. Krivorotov, G. D. Fuchs, P. M. Braganca, O. Ozatay, J. C. Sankey, D. C. Ralph, and R. A. Buhrman. Magnetic vortex oscillator driven by d.c. spin-polarized current. *Nat Phys*, 3(7):498–503, July 2007.

[179] X. Z. Yu, N. Kanazawa, Y. Onose, K. Kimoto, W. Z. Zhang, S. Ishiwata, Y. Matsui, and Y. Tokura. Near room-temperature formation of a skyrmion crystal in thin-films of the helimagnet FeGe. *Nat Mater*, 10(2):106–109, February 2011.

[180] C. Moreau-Luchaire, C. Moutafis, N. Reyren, J. Sampaio, C. a. F. Vaz, N. Van Horne, K. Bouzehouane, K. Garcia, C. Deranlot, P. Warnicke, P. Wohlhüter, J.-M. George, M. Weigand, J. Raabe, V. Cros, and A. Fert. Additive interfacial chiral interaction in multilayers for stabilization of small individual skyrmions at room temperature. *Nat Nano*, 11(5):444–448, May 2016.

[181] Gen Yin, Yizhou Liu, Yafis Barlas, Jiadong Zang, and Roger K. Lake. Topological spin Hall effect resulting from magnetic skyrmions. *Phys. Rev. B*, 92(2):024411, July 2015.

[182] M. Mochizuki, X. Z. Yu, S. Seki, N. Kanazawa, W. Koshibae, J. Zang, M. Mostovoy, Y. Tokura, and N. Nagaosa. Thermally driven ratchet motion of a skyrmion microcrystal and topological magnon Hall effect. *Nat Mater*, 13(3):241–246, March 2014.

[183] A. Neubauer, C. Pfleiderer, B. Binz, A. Rosch, R. Ritz, P. G. Niklowitz, and P. Böni. Topological Hall Effect in the A Phase of MnSi. *Phys. Rev. Lett.*, 102(18):186602, May 2009.

[184] Y. Nii, A. Kikkawa, Y. Taguchi, Y. Tokura, and Y. Iwasa. Elastic Stiffness of a Skyrmion Crystal. *Phys. Rev. Lett.*, 113(26):267203, December 2014.

[185] S. Seki, X. Z. Yu, S. Ishiwata, and Y. Tokura. Observation of Skyrmions in a Multiferroic Material. *Science*, 336(6078):198–201, April 2012.

[186] Karin Everschor, Markus Garst, R. A. Duine, and Achim Rosch. Current-induced rotational torques in the skyrmion lattice phase of chiral magnets. *Phys. Rev. B*, 84(6):064401, August 2011.

[187] Masahito Mochizuki. Spin-wave modes and their intense excitation effects in skyrmion crystals. *Phys. Rev. Lett.*, 108(1):017601, January 2012.